Astérosismologie des étoiles de type solaire, avec ou sans planètes, abondance des éléments et phénomènes de transport

María Eliana Escobar

▶ **To cite this version:**

María Eliana Escobar. Astérosismologie des étoiles de type solaire, avec ou sans planètes, abondance des éléments et phénomènes de transport. Astrophysique stellaire et solaire [astro-ph.SR]. Université Paul Sabatier - Toulouse III, 2013. Français. NNT : . tel-00909055

HAL Id: tel-00909055

https://theses.hal.science/tel-00909055v1

Submitted on 25 Nov 2013

HAL is a multi-disciplinary open access archive for the deposit and dissemination of scientific research documents, whether they are published or not. The documents may come from teaching and research institutions in France or abroad, or from public or private research centers.

L'archive ouverte pluridisciplinaire **HAL**, est destinée au dépôt et à la diffusion de documents scientifiques de niveau recherche, publiés ou non, émanant des établissements d'enseignement et de recherche français ou étrangers, des laboratoires publics ou privés.

Université de Toulouse

THÈSE

En vue de l'obtention du

DOCTORAT DE L'UNIVERSITÉ DE TOULOUSE

Délivré par :
Université Toulouse III Paul Sabatier (UT3 Paul Sabatier)

Discipline ou spécialité :

Astrophysique

Présentée et soutenue par :
María Eliana Escobar Muñoz
le : jeudi 26 septembre 2013

Titre :

Astérosismologie des étoiles de type solaire avec ou sans planètes, abondance des éléments et phénomènes de transport

---

Ecole doctorale :
Sciences de l'Univers, de l'Environnement et de l'Espace (SDU2E)

Unité de recherche :
Institut de Recherche en Astrophysique et Planétologie (IRAP)

Directeur(s) de Thèse :

Sylvie Vauclair

Rapporteurs :

Pr. Magali Deleuil (LAM, Université de Marseille)
Pr. Jianning Fu (Beijing Normal University)

Membre(s) du jury :

Dr. Georges Alecian (LUTH, Observatoire de Paris)
Pr. Magali Deleuil (LAM, Université de Marseille)
Pr. Jianning Fu (Beijing Normal Univerity)
Dr. Andrés Moya (Centro de Astrobiología, Madrid)
Pr. Sylvie Vauclair (IRAP, Université de Toulouse)

A mi abuelito, que siempre quiso tener un@ niet@ doctor@ ...

Contents

Introduction

Depuis plusieurs décennies, les observations des oscillations stellaires et la recherche d'exoplanètes se sont développées en parallèle, en utilisant les mêmes méthodes et les mêmes instruments : la méthode de la vitesse radiale, à partir essentiellement d'instruments au sol, et la méthode photométrique (courbes de lumière), à partir d'instruments spatiaux. De plus, les mêmes données observationnelles obtenues pour une même étoile ont pu conduire à la découverte d'exoplanètes, à une grande échelle temporelle (de quelques jours à quelques années), aussi bien que à la détection d'oscillations de type solaire à petite échelle temporelle (quelques minutes). Ce fut le cas, par exemple, pour l'étoile μ Arae (Pepe et al. (2007), Santos et al. (2004a), Bouchy et al. (2005),Bazot et al. (2005), Soriano & Vauclair (2010)).

Dans ce double but, des instruments puissants et précis ont été construits depuis quelques années. Des spectrographes au sol comme HARPS et SOPHIE ont donné d'excellents résultats à la fois pour la recherche d'exoplanètes et pour l'astérosismologie. HARPS (High Accuracy Radial velocity Planet Searcher) est un spectrographe échelle de haute précision installé sur le télescope de 3.6m à l'observatoire de La Silla, Chili. Comme son nom l'indique, il a été construit initialement pour chercher des exoplanètes depuis l'hémisphère sud, et a déjà permis la découverte de 130 nouvelles planètes jusqu'à présent. De plus, ses performances permettent aussi l'identification d'oscillations de type solaire. Nous pouvons mentionner plusieurs exemples, comme les étoiles μ Arae (Bouchy et al., 2005), ι Horologii (Vauclair et al., 2008), parmi d'autres. Dans l'hémisphère nord il y a SOPHIE, un spectrographe à haute résolution monté sur le télescope de 1.96m à l'observatoire de Haute Provence. Comme HARPS, SOPHIE a été prévu pour la recherche d'exoplanètes, mais permet aussi des études d'astérosismologie.

Cependant, l'astérosismologie au sol présente quelques problèmes. Même si d'importantes informations peuvent être obtenues, la coupure journalière dans les observations représente un problème majeur pour les identifications précises de modes d'oscillation. Cette coupure induit des alias dans les données, et rend la tâche très difficile. Les observations multisites peuvent aider à limiter ces alias, mais les observations spatiales sont encore bien meilleures sur ce plan. Nous avons ainsi deux exemples de la synergie entre les recherches d'exoplanètes et l'astérosismologie avec

les satellites CoRoT et *Kepler*. Lancé en décembre 1996, CoRoT (Convection, Rotation and lanetary Transit, Baglin et al. (2006)) comprend un télescope de 27cm avec 4 caméras CCD qui observèrent de manière interrompue des milliers d'étoiles pendant 6 ans. La photométrie de haute précision obtenues avec CoRoT a conduit à d'importantes découvertes en ce qui concerne les exoplanètes, comme la première super-Terre en transit, COROT 7-b (Leger et al. (2009), Queloz et al. (2009)), et les premières naines brunes en transit (Deleuil et al. (2008), Bouchy et al. (2011)). Elle a conduit aussi à l'identification de modes d'oscillation pour de nombreuses étoiles, comme HD 52265 (Ballot et al. (2011)), HD 49933 (Samadi et al. (2010)) et HD 46375(Gaulme et al. (2010)) parmi d'autres.

La mission *Kepler* (Koch et al. (2010)) commence en Mars 2009. Construit au départ dans le but de découvrir des planètes de taille terrestre, dans la zone habitable, il comprend un télescope de 0.95 m et un ensemble de caméras CCD qui permettent une grande précision dans la détection des variations de luminosité stellaire, et donc la détection d'exoplanètes et d'oscillations stellaires. Des oscillations ont été détectées dans plus de 500 étoiles (Chaplin et al. (2011)). L'intérêt d'étudier les oscillations des étoiles centrales de systèmes planétaires est apparu dès le début de ces observations. La caractérisation des planètes nécessite une très bonne connaissance de l'étoile centrale et particulièrement de ses paramètres globaux comme la masse, le rayon, la température. Il est important aussi d'essayer de contraindre au maximum l'intérieur de ces étoiles (profondeur de zone convective extérieure, cour convectif, composition chimique, etc.). L'étude de la différence entre les étoiles possédant des planètes et celles qui n'en ont pas, peut apporter des informations précieuses pour mieux comprendre la formation des systèmes planétaires. Il est bien connu, par exemple, que les étoiles possédant des planètes ont en moyenne des métallicités supérieures à celles qui n'en ont pas. L'étude de leurs oscillations peut permettre de mieux comprendre l'origine et les conséquences de ces différences.

Le très grand nombre d'exoplanètes ou de candidats exoplanètes détectés par les expériences spatiales, en particulier *Kepler*, nécessite à présent des procédures automatiques pour extraire les paramètres principaux des étoiles centrales à partir de l'étude de leurs oscillations. Cependant, des études astérosismiques précises de quelques étoiles bien choisies sont encore importantes pour une plus grande précision des résultats, et pour tester les autres procédures.

Dans cette thèse, nous avons choisi d'étudier précisément trois étoiles centrales de systèmes planétaires de type solaire :

- HD52265, une étoile G0V, la seule étoile cible principale de COROT, observée pendant plusieurs mois consécutifs avec une précision photométrique inégalée.

- 94 Ceti, une étoile F8V, une étoile centrale de système planétaire dont les paramètres spectroscopiques ressemblent à ceux de β virginis, étoile sans planète,

elle-même bien étudié par ailleurs ; cette étoile 94 Ceti a été observée avec le spectromètre HARPS à La Silla, Chili.

- 51 Pegasi, une étoile G2IV, étoile " mythique" hôte de la première exoplanète observée en 1995 par Michel Mayor et Didier Queloz; cette étoile a été observée avec le spectromètre SOPHIE à l'OHP.

Dans tous les cas, nous avons comparé les fréquences observées et leurs combinaisons, avec celles calculées pour des modèles obtenus avec le Toulouse-Geneva Evolution Code (TGEC). Les fréquences ont été calculées avec le code PULSE, de Montreal. Divers aspects physiques ont été testés, en particulier la diffusion atomique incluant les forces radiatives sur les éléments lourds.

Nous avons obtenu des résultats intéressants pour ces trois étoiles, pour lesquelles les approches sont différentes. Dans les trois cas nous déduisons les paramètres extérieurs et des informations sur la structure. Ce travail comprend à la fois un aspect observationnel et de modélisation. C'est donc une approche assez complète de l'astérosismologie et de ses techniques.

La présentation comprend 5 chapitres. Dans le chapitre 2 nous introduisons des concepts de base d'astérosismologie, dans le chapitre 3 nous présentons la modélisation de l'étoile HD52265, le chapitre 4 est consacré à l'étoile 94 Ceti, dont nous présentons les identifications de modes et la modélisation, et enfin dans le Chapitre 5 nous donnons des résultats préliminaires sur 51 Peg, en expliquant les difficultés particulières présentées pour cette étoile. Le manuscrit se termine par une conclusion et discussion du travail effectué.

Introduction

Stars are the main components of the visible Universe. When looking at the sky it is difficult to imagine that a simple light spot could harbor so many interesting physical phenomenas. At the first stages of observational studies on stellar interiors, the available techniques and instrumentation only allowed us to access to the surface layers of the stars. By the inference of different properties as metallicity, log g and temperature, combined with the theory of stellar interior and evolution, it was possible to infer some other important properties of the stars as their masses, radius and ages, although not with a high precision. This situation has changed with asteroseismology, giving us the unique opportunity to study stellar interiors with an accuracy never reached before.

During the past decades, stellar oscillations and exoplanet searches have been developed in parallel. Consequently, observations have been done with the same instruments, and thus similar techniques are used for the detection of exoplanets as well as for solar-like oscillations: radial velocity method, essentially with ground-based instruments, and photometric methods (light curves) from space. Moreover, the same observational data taken for a star could lead to planet discoveries at large time scales (days to years) as well as to the detection of stellar oscillations at small time scales (minutes). This has been the case of the star μ Arae (Pepe et al. (2007), Santos et al. (2004a), Bouchy et al. (2005), Bazot et al. (2005), Soriano & Vauclair (2010)).

For this purpose powerful and precise instruments have been built. Ground-based spectrographs like HARPS and SOPHIE have give very valuable results in exoplanet searches as well as asteroseismic observations. HARPS (High Accuracy Radial velocity Planet Searcher) is a high precision échelle spectrograph installed in the 3.6 m telescope at La Silla Observatory, Chile. As it appears from its name, it was initially designed for planet hunting in the south hemisphere, giving more than 130 new discoveries to date. Nevertheless, its high performance also allows the identification of solar-like oscillations. As an example we can mention the stars μ Arae (Bouchy et al. (2005)), ι Horologii (Vauclair et al. (2008)), among others. In the north hemisphere there is SOPHIE, a high resolution spectrograph mounted in the 1.96 m telescope at the Haute Provence Observatory, France. Both HARPS

and SOPHIE were built by the same team (M. Mayor and his collaborators, from Geneva Observatory). SOPHIE was also primary designed for exoplanet searches. But also asteroseismic observations have been done with this instrument and with its previous versions as CORALIE and ELODIE (Bouchy & Carrier (2001), Carrier et al. (2005))).

However ground-based observations present some problems. Even if important information can be obtained, the day-gap between observations is a major problem in the attempt of good and precise mode identification. This day-gap induces strong aliases in the data, making frequency identification a very difficult task. Multisite observations may help avoiding these aliases, but the results are better from space. Two good examples of the synergy between exoplanet searches and asteroseismology are the CoRoT and *Kepler* satellites. Launched in December 1996, CoRoT (Convection. Rotation and planetary Transits, Baglin et al. (2006)) contains a 27 cm telescope with 4 CCD-cameras that observed uninterruptedly thousands of stars for about 6 years. High-precision photometry obtained from CoRoT gave important results in exoplanet discoveries, like the first transiting super-earth, CoRoT-7b (Leger et al. (2009), Queloz et al. (2009)), and first transiting brown dwarfs CoRoT-3b (Deleuil et al. (2008)) and CoRoT-15b (Bouchy et al. (2011)), and also in mode identification for several stars as HD 52265 (Ballot et al. (2011)), HD 49933 (Samadi et al. (2010))and HD 46375 (Gaulme et al. (2010)) among others.

The NASA *Kepler* mission (Koch et al. (2010)) started in March 2009. Designed for the discovery of habitable-zone earth-sized planets, the spacecraft is equipped with a 0.95 m telescope and an array of CCDs that provides high-precision photometry allowing the detection of the variations in stellar brightness due to solar-like oscillations and to planetary transits. Its 105 square degrees field of view allows the uninterrupted monitoring of thousands stars of different types. *Kepler* results for asteroseismology have been huge, detecting solar-like oscillations in more than 500 stars (Chaplin et al. (2011)). In the exoplanet context, *Kepler* announced in 2012 the discovery of the first two earth-size planet around the star Kepler-20 (Fressin et al. (2012)).

But synergy between exoplanets and asteroseismology does not restrict only to instrumentation. Stellar astrophysics has a lot to say when regarding exoplanets studies. First, for a good and precise determination of planet properties a good characterization of the parent star is strongly needed. Stellar properties as mass and radius are used to obtain planet essential parameters. This becomes more important concerning earth-sized planet studies. Additionally, precise determination of stellar ages and internal structure as chemical composition gives new insight on the characteristics of the planet formation scenario. Thus, asteroseismology has become an important tool in our understanding of planetary systems formation and evolution.

Since the discovery of the first planet orbiting another star than our Sun (Mayor & Queloz (1995)), several observational ground-based programs were dedicated not only to the search of more extra-solar planets, but also to the characterization of the exoplanet parent stars. As it was already mentioned, a correct characterization of the parent star is very important to deduce the parameters of the whole planetary system. For this reason, several spectroscopic campaigns were carried to infer basic properties of these stars, as effective temperature, metallicity and log g. From these studies, remarkable was the fact that in most cases exoplanet host stars showed a higher metal content when comparing to the Sun (Santos et al. (2003), Santos et al. (2005), Fischer & Valenti (2005)). This lead to several theories of the origin of this overmetallicity, with two possible scenarios: (i) this higher metal content has a primordial origin, meaning that the molecular cloud were the star was form was already rich in metal content, and (ii) the overmetallicity was produced due to other phenomena after star formation. This was call the accretion scenario, where planetesimal already created during cloud collapse had been falling into the star during early stages of stellar evolution, thus increasing the metal content of the outer layers of the star. Many theoretical and observational studies were performed in order to find the answer to this issue. Now it is known that this overmetallicity has a primordial origin. One of the first results pointing to this result was the asteroseismic modeling of the exoplanet-host star ι Hor, where it was found that this star was an evaporated member of the Hyades cluster, confirming the primordal origin of its higher metal content (Vauclair et al. (2008)). Also, theoretical studies have shown that the amount of planetesimals needed to be accreated to reach the overmetallic content that is seen in exoplanet host star is too large to be realistic. Finally, Vauclair (2004), Garaud (2011), Traxler et al. (2011) and Vauclair & Théado (2012) showed that heavy element accretion onto a star leads to a double-diffusive instability (thermohaline convection) so that the accreted matter sinks inside the star.

With thousands of exoplanet candidates discovered by *Kepler*, automatic procedures and pipelines are needed for large databases to obtain the characteristics of the central stars. However, precise asteroseismic studies of well-chosen stars are still important for a deeper insight on stellar characteristics and phenomena, and also to obtain the most precise results as possible. Also, performing this individual studies will help to compare the results with the automatic procedure, and then infer whether they are trustful in that specific case. In this work we present individual asteroseismic studies of three solar-like exoplanet-host stars:

- HD 52265, a G0V star, the only exoplanet-host star observed as a main target by CoRoT.

- 94 Ceti, a F8V star, an exoplanet-host star whose spectroscopic parameters

are close to the well known star β Virginis, a star that has no detected planet. Both stars belong to a binary system. Observations for 94 Cet were obtained using the HARPS spectrograph installed in La Silla Observatory, Chile.

- 51 Pegasi, a G2IV star, the host of the first exoplanet ever discovered, in 1995. Asteroseismic data for this star was taken with the spectrograph SOPHIE (Haute Provence Observatory, France), installed at the same telescope where the observation for the planet discovery were done.

We obtained interesting results for these three stars, which will be presented and discussed in the following chapters, and in the conclusion. In particular we were able to derive their stellar parameters, to do comparisons with automatic procedures, to check the importance of the internal chemical composition, and to test the importance of radiative accelerations on individual elements for asteroseismic purposes.

The presentation of my 4 years thesis work will be as follows: in chapter 2 we introduce some basic concepts on the theory of stellar oscillations; in chapter 3 we present the modeling of HD 52265; in chapter 4 we present mode identification and modeling of the star 94 Cet, and in chapter 5 we give the results of a preliminary modeling of 51 Peg, together with the observational results. Conclusions are presented at the end of this manuscript.

Chapter 1

Theory of Stellar Oscillations

1.1 Equations for stellar oscillations

The theory of stellar oscillations is developed in several textbooks, like Unno et al. (1979) (Non Radial Oscillations of Stars), or Aerts & Christensen-Dalsgaard, J. and Kurtz, D. W. (2010) (Asteroseismology). A very good course is found in the "Lecture Notes on Stellar Oscillations" by Christensen-Dalsgaard (2003). In this chapter, we present general formalisms which are important for our work. At the end of this chapter we also present some of our own results, concerning the effect of the stellar chemical composition on the induced seismic parameters.

1.1.1 Hydrodynamical equations

A gas can be treated as a continuum, so its properties will be characterized as functions of position $\mathbf{r}$ and time t. This gas will follow the hydrodynamic equations:

- Equation of Continuity

  The fact that the mass is conserved can be expressed as:

  $$\frac{\partial \rho}{\partial t} + \nabla(\rho \mathbf{v}) = 0, \tag{1.1}$$

  where ρ is the density, and $\mathbf{v}$ is the instant velocity. This equation gives the rate of change of density following the motion.

- Equation of Motion

  $$\rho \frac{\partial \mathbf{v}}{\partial t} + \rho \mathbf{v} \cdot \nabla \mathbf{v} = -\nabla p + \rho \mathbf{g}, \tag{1.2}$$

where p is the pressure, and $\mathbf{g}$ is the gravitational acceleration which can be written as the gradient of the gravitational potential:

$$\mathbf{g} = -\nabla\Phi, \tag{1.3}$$

where Φ satisfies the Poisson equation:

$$\nabla^2\Phi = 4\pi G\rho, \tag{1.4}$$

whose integral solution is:

$$\Phi(\mathbf{r}, t) = -G\int_V \frac{\rho(\mathbf{r}', t)dV'}{\mid \mathbf{r} - \mathbf{r}' \mid}, \tag{1.5}$$

where the integral is taken over the volume V of the star.

- Equation of Energy

  This equation will give us a relation between p and ρ. If the system satisfies the first law of thermodynamics, we have:

$$\frac{dq}{dt} = \frac{dE}{dt} + p\frac{dV}{dt}, \tag{1.6}$$

where $\frac{dq}{dt}$ is the rate of heat loss or gain and E is the internal energy per unit mass. Using thermodynamical identities, equation 1.6 can be written as:

$$\begin{aligned} \tfrac{dq}{dt} &= \tfrac{1}{\rho(\Gamma_3-1)}(\tfrac{dp}{dt} - \tfrac{\Gamma_1 p}{\rho}\tfrac{d\rho}{dt}) \\ &= c_p(\tfrac{dT}{dt} - \tfrac{\Gamma_2-1}{\Gamma_2}\tfrac{T}{p}\tfrac{dp}{dt}) \\ &= c_V[\tfrac{dT}{dt} - (\Gamma_3 - 1)\tfrac{T}{\rho}\tfrac{d\rho}{dt}], \end{aligned} \tag{1.7}$$

where c_p and c_V are the specific heat per unit mass at constant pressure and volume, respectively, and the adiabatic exponents are defined by:

$$\Gamma_1 = (\frac{\partial \ln p}{\partial \ln \rho})_{ad}, \quad \frac{\Gamma_2 - 1}{\Gamma_2} = (\frac{\partial \ln T}{\partial \ln p})_{ad}, \quad \Gamma_3 - 1 = (\frac{\partial \ln T}{\partial \ln \rho})_{ad}. \tag{1.8}$$

The relation between p, ρ, T and Γ_i $(i = 1, 2, 3)$, will depend on the thermodynamical state and composition of the gas. Where the heating can be

neglected (i.e, $\frac{dq}{dt} = 0$), the motion occurs adiabatically. Then equation 1.7 can be expressed as:

$$\frac{dp}{dt} = \frac{\Gamma_1 p}{\rho}\frac{d\rho}{dt}. \tag{1.9}$$

For stars, the heat gain has to be considered in more detail. Specifically, it can be written as:

$$\rho\frac{dq}{dt} = \rho\epsilon - div\mathbf{F}, \tag{1.10}$$

where ϵ is the rate of energy generation per unit mass and $\mathbf{F}$ is the flux of energy.

Equations 1.9, 1.1, 1.2, and 1.4 are the equations that describe adiabatic motion.

1.1.2 Perturbation Analysis

Performing a direct analysis of stellar pulsation using the equations described in the previous section is of great complexity. But simplifications are possible. Observed solar and solar-like oscillations have small amplitudes compared with the characteristic scales of a star. This allows to treat them as small perturbations around a static equilibrium state. By being static means that all time derivatives can be neglected. Let us assume that there are no velocities, so equation 1.1 is satisfied. Then, the equations of motion 1.2 can be simplified to the equation of hydrostatic equilibrium:

$$\nabla p_0 = \rho_0 \mathbf{g_0} = -\rho_0 \nabla \Phi_0, \tag{1.11}$$

where the subscript "0" indicates the equilibrium quantities. The Poisson equation 1.4 is unchanged:

$$\nabla^2 \Phi_0 = 4\pi G \rho_o. \tag{1.12}$$

And the equation of energy 1.10 becomes:

$$\frac{dq}{dt} = 0 = \epsilon_0 - \frac{1}{\rho_0} div\mathbf{F_0}. \tag{1.13}$$

Now let's consider small perturbations around the equilibrium state. Then the pressure can be written as:

$$p(\mathbf{r},t) = p_o(\mathbf{r}) + p'(\mathbf{r},t), \tag{1.14}$$

where p' is a small perturbation. This is the perturbation in *Eulerian* description, *i.e*, the perturbation at a given point. For our purposes it is convenient to use the *Lagrangian* description, where the reference frame follows the motion. If an element of gas is moved from $\mathbf{r_0}$ to $\mathbf{r_0} + \delta\mathbf{r_0}$, then the pressure can be written as:

$$\delta p(\mathbf{r}) = p'(\mathbf{r_0}) + \delta\mathbf{r} \cdot \nabla p_0. \tag{1.15}$$

The perturbations equations are obtained by introducing these perturbations into the full equations and linearizing them. Then, the continuity equation 1.1 becomes:

$$\delta p + \rho_0 div(\delta\mathbf{r}) = 0. \tag{1.16}$$

The equation of motion results in:

$$\rho_0 \frac{\partial \delta\mathbf{r}}{\partial t^2} = -\nabla p' + \rho_0 \mathbf{g}' + \rho' \mathbf{g_0}, \tag{1.17}$$

where $\mathbf{g}' = -\nabla\Phi'$, and the perturbation Φ' to the gravitational potential satisfies the perturbed Poisson equation:

$$\nabla^2\Phi' = 4\pi G\rho', \tag{1.18}$$

whose integral solution is:

$$\Phi' = -G\int_V \frac{\rho'(\mathbf{r}',t)}{\mid \mathbf{r} - \mathbf{r}' \mid} dV'. \tag{1.19}$$

And the energy equation become:

$$\frac{\partial \delta q}{\partial t} = \frac{1}{\rho_0(\Gamma_{3,0} - 1)}\left(\frac{\partial \delta p}{\partial t} - \frac{\Gamma_{1,0} p_0}{\rho_0}\frac{\partial \delta\rho}{\partial t}\right), \tag{1.20}$$

which in terms of equation 1.10 is:

$$\rho_0 \frac{\partial \delta q}{\partial t} = (\rho\epsilon - div\mathbf{F})'. \tag{1.21}$$

In case of adiabatic motion, we can neglect the heating term. Thus we obtain:

$$\frac{\partial \delta p}{\partial t} = \frac{\Gamma_{1,0} p_0}{\rho_0}\frac{\partial \delta\rho}{\partial t}. \tag{1.22}$$

1.1.3 Oscillation Equations: Separation of Variables

The displacement δr can be separated into radial and horizontal coordinates:

$$\delta r = \xi_r \mathbf{a}_r + \xi_\mathbf{h}, \tag{1.23}$$

with

$$\xi_\mathbf{h} = \xi_\theta \mathbf{a}_\theta + \xi_\phi \mathbf{a}_\phi. \tag{1.24}$$

From equation 1.17, and taking its horizontal divergence, it gives:

$$\rho_0 \frac{\partial^2}{\partial t^2} \nabla_h \cdot \xi_\mathbf{h} = -\nabla_h^2 p' - \rho \nabla_h^2 \Phi'. \tag{1.25}$$

The equation of continuity 1.16 can be written as:

$$\rho' = -div(\rho \delta \mathbf{r}) = -\frac{1}{r^2}\frac{\partial}{\partial r}(\rho r^2 \xi_r) - \rho \nabla_h \cdot \xi_\mathbf{h}. \tag{1.26}$$

Using this expression to eliminate $\nabla_h \cdot \xi_\mathbf{h}$, equation 1.25 becomes:

$$-\frac{\partial^2}{\partial t^2}[\rho' + \frac{1}{r^2}\frac{\partial}{\partial r}(r^2 \rho \xi_r)] = -\nabla_h^2 p' - \rho_0 \nabla_h^2 \Phi'. \tag{1.27}$$

The radial component of the motion equation 1.17 is:

$$\rho_0 \frac{\partial^2 \xi_r}{\partial t^2} = -\frac{\partial p'}{\partial r} - \rho' g_0 - \rho_0 \frac{\partial \Phi'}{\partial r}. \tag{1.28}$$

Finally, the Poisson equation 1.18 may be written as:

$$\frac{1}{r^2}\frac{\partial}{\partial r}(r^2 \frac{\partial \Phi'}{\partial r}) + \nabla_h^2 \Phi' = 4\pi G \rho'. \tag{1.29}$$

Taking account of the spherical symmetry allows to separate the radial component of the motion from the non-radial component which can be developed in spherical harmonics.

Then, the dependent variable present in equation 1.27, 1.28 and 1.29 can be written in the following way:

$$\begin{aligned}\xi_r(r,\theta,\phi,t) &= \sqrt{4\pi}\tilde{\xi}_r(r)Y_\ell^m(\theta,\phi)\exp -i\omega t p'(r,\theta,\phi,t) \\ &= \sqrt{4\pi}\tilde{p'}(r)Y_\ell^m(\theta,\phi)\exp -i\omega t ...etc. \qquad (1.30)\end{aligned}$$

$(\rho' \; and \; \Phi')$

where $\tilde{\xi}_r$, $\tilde{p'}(r)$, ...etc. are the amplitude functions, and $Y_\ell^m(\theta,\phi)$ are the spherical harmonics, characterized by their degree ℓ and azimuthal order m, defined by:

$$Y_l^m(\theta,\phi) = (-1)^m \frac{(2\ell+1)(\ell-m)!}{4\pi(\ell+m)} P_\ell^m(\cos\theta), \qquad (1.31)$$

where P_ℓ^m is the Legendre function. We see that equations 1.30 have $Y_\ell^m(\theta,\phi)$ $\exp -i\omega t$ as a common factor. Then if we divide these equations by it, we can obtain the following differential equations for the amplitude functions:

$$\begin{aligned}\omega^2\left[\tilde{\rho'} + \tfrac{1}{r^2}\tfrac{d}{dr}(r^2\rho_0\tilde{\xi_r})\right] &= \tfrac{\ell(\ell+1)}{r^2}(\tilde{p'} + \rho_0\tilde{\Phi'}) - \omega^2\rho\tilde{\xi_r} \\ &= -\tfrac{d\tilde{p'}}{dr} - \tilde{\rho'}g_0 - \rho_0\tfrac{d\tilde{\Phi'}}{dr}\tfrac{1}{r^2}\tfrac{d}{dr}\left(r^2\tfrac{d\tilde{\Phi'}}{dr}\right) - \tfrac{\ell(\ell-1)}{r^2}\tilde{\Phi'} \qquad (1.32) \\ &= 4\pi G\tilde{\rho'}\end{aligned}$$

And the energy equation is:

$$\rho_0(\Gamma_{3,0}-1)\delta\tilde{q} = \delta\tilde{p'} - \frac{\Gamma_{1,0}p_0}{\rho_0}\delta\tilde{\rho'}. \qquad (1.33)$$

We notice that equations 1.32 and 1.33 do not depend on the azimuthal order m, in agreement with the assumption of spherical symmetry of the equilibrium state.

1.2 Adiabatic Nonradial Oscillations

If we consider adiabatic oscillations, the heat term can be neglected. Then, with $\delta q = 0$, the energy equation 1.33 simplifies and can be written as:

$$\delta p = \frac{\Gamma_1 p}{\rho}\delta\rho, \qquad (1.34)$$

and then:

$$\rho' = \frac{\rho}{\Gamma_1 p} p' + \rho \xi_r \left(\frac{1}{\Gamma_1 p} \frac{dp}{dr} - \frac{1}{\rho} \frac{d\rho}{dr} \right). \tag{1.35}$$

Using this expression it is possible to eliminate ρ' in equations 1.32. For the first equation we obtain:

$$\frac{d\xi_r}{dr} = -\left(\frac{2}{r} + \frac{1}{\Gamma_1 p} \frac{dp}{dr} \right) \xi_r + \frac{1}{\rho c^2} \left(\frac{S_\ell^2}{\omega^2} - 1 \right) p' + \frac{\ell(\ell+1)}{\omega^2 r^2} \Phi', \tag{1.36}$$

where $c^2 = \Gamma_1 p / \rho$ is the square of the adiabatic sound speed, and we have introduced the characteristic acoustic frequency S_ℓ, or Lamb frequency, defined as:

$$S_\ell^2 = \frac{\ell(\ell+1) c^2}{r^2}. \tag{1.37}$$

The second equation gives:

$$\frac{dp'}{dr} = \rho(\omega^2 - N^2)\xi_r + \frac{1}{\Gamma_1 p} \frac{dp}{dr} p' - \rho \frac{d\Phi'}{dr}, \tag{1.38}$$

where we have introduced the bouyancy frequency, or Brunt-Väisälä frequency, defined by:

$$N^2 = g \left(\frac{1}{\Gamma_1 p} \frac{dp}{dr} - \frac{1}{\rho} \frac{d\rho}{dr} \right). \tag{1.39}$$

And finally, the third equation becomes:

$$\frac{1}{r^2} \frac{d}{dr} \left(r^2 \frac{d\Phi'}{dr} \right) = 4\pi G \left(\frac{p'}{c^2} + \frac{\rho \xi_r}{g} N^2 \right) + \frac{\ell(\ell+1)}{r^2} \Phi' \tag{1.40}$$

Equations 1.36, 1.38 and 1.40 form a complete set of fourth-order ordinary differential equations for the four dependent variables ξ_r, p', Φ' and $\frac{d\Phi'}{dr}$. All coefficients in these equations are real. We expect that the solution is such that ω^2 is real, thus the eigenfunction may be chosen to be real as well. Two cases can be possible: (i) the frequency is purely real, in which case the motion is undamped oscillatory, or (ii) the frequency is purely imaginary, in which case the motion will grow or decay exponentially.

1.2.1 The Cowling Approximation

The general equations that rule the stellar oscillations are fourth-order differential equation system not trivial to be solved. A first step in order to simplify these equations is to neglect the perturbation to the gravitational potential Φ'. This is the Cowling approximation. By applying it the system is reduced to a second-order equations system, so the equations can be written as:

$$\begin{aligned} \frac{d\xi_r}{dr} &= -\left(\frac{2}{r} - \frac{1}{\Gamma_1}H_p^{-1}\right)\xi_r + \frac{1}{\rho c^2}\left(\frac{S_\ell^2}{\omega^2} - 1\right)p' \\ \frac{dp'}{dr} &= \rho(\omega^2 - N^2)\xi_r - \frac{1}{\Gamma_1}H_p^{-1}p', \end{aligned} \tag{1.41}$$

where

$$H_p^{-1} = -\frac{d\ln p}{dr} \tag{1.42}$$

is the pressure scale height.

If we consider oscillations with high radial orders, the eigenfunctions vary much more rapidly than the equilibrium quantities. Considering this, we can, as a first rough approximation, neglect the derivatives of the equilibrium quantities. Then the system can be written as:

$$\begin{aligned} \frac{d\xi_r}{dr} &= \frac{1}{\rho c^2}\left(\frac{S_\ell^2}{\omega^2} - 1\right)p' \\ \frac{dp'}{dr} &= \rho(\omega^2 - N^2)\xi_r. \end{aligned} \tag{1.43}$$

These two equations can be combined into a single second-order differential equation for ξ_r, resulting:

$$\frac{d^2\xi_r}{dr^2} = \frac{\omega^2}{c^2}\left(1 - \frac{N^2}{\omega^2}\right)\left(\frac{S_\ell^2}{\omega^2} - 1\right)\xi_r. \tag{1.44}$$

This equation can describe adequately the overall properties of the modes and will give good determination of their frequencies. From this equation we can also notice that the Brunt-Väisälä (N) and Lamb (S_ℓ) frequencies play an important role on the behavior of the oscillations. Their evolution with the star radius is shown in figure 1.1, for a solar standard model, which is representative of lower-main sequence stars. We see that S_ℓ tends to infinity as r tends to zero, and decreases monotonically towards the surface. The Brunt-Väisälä frequency (N) is negative in

convective zones, and positive within radiative zones. The maximum in N seen very near the center is associated to the increase of the helium abundance, where the nuclear burning occurs.

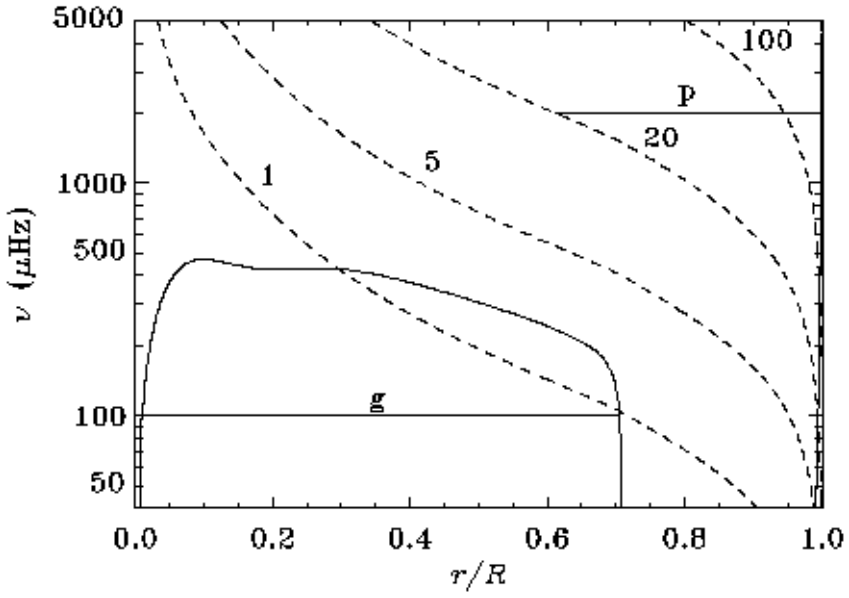

Figure 1.1: Brunt-Väisälä frequency N (continuous line) and characteristic Lamb frequency S_ℓ (dashed line, labeled by the values of ℓ) vs r/R for a standard solar model. The heavy horizontal lines indicate the trapping regions for a g mode with frequency ν=100 μHz, and for a p mode with degree 20 and ν=2000 μHz.

To analyze the behavior of the oscillations, equation 1.44 can be written as:

$$\frac{d^2\xi_r}{dr^2} = -K_s(r)\xi_r, \tag{1.45}$$

where

$$K_s(r) = \frac{\omega^2}{c^2}\left(\frac{N^2}{\omega^2} - 1\right)\left(\frac{S_\ell^2}{\omega^2} - 1\right). \tag{1.46}$$

The behavior of ξ_r will depend on the sign of $K_s(r)$. If $K_s(r)$ is positive, ξ_r is a oscillating function of r, and the solution can be written approximately as:

$$\xi_r \sim \cos\left(\int K_s^{1/2} dr + \phi\right), \tag{1.47}$$

where ϕ is a phase determined by the boundary conditions. If $K_s(r)$ is negative then ξ_r will be an exponentially increasing or decreasing function of r. In this case the solution can be written approximately as:

$$\xi_r \sim \exp\left(\pm \int \mid K_s \mid^{1/2} dr\right). \tag{1.48}$$

Thus, the solution is oscillatory as a function of r when:

$\mid \omega \mid > \mid N \mid$ and $\mid \omega \mid > S_\ell$,

or,

$\mid \omega \mid < \mid N \mid$ and $\mid \omega \mid < S_\ell$.

And the solutions will be exponential when:

$\mid N \mid < \mid \omega \mid < S_\ell$,

or,
$S_\ell < \mid \omega \mid < \mid N \mid$.

Regarding these solution, it is possible for a given mode of oscillation to have some regions where the solutions oscillates, with some intervening regions where the solution is exponential. However, in general one of the oscillating regions is dominant. It is said that the mode is *trapped* in this region and its frequency is determined by the structure of the model in this region of trapping. The boundaries of this region are known as *turning points* and are determined where $K_s(r) = 0$.

From the behavior of S_ℓ and N as shown in figure 1.1, and the conditions for an oscillatory solution, we can have two classes of modes:

- Modes with high frequencies that satisfy $\mid \omega \mid > \mid N \mid$ and $\mid \omega \mid > S_\ell$ - they are p modes.

- Modes with low frequencies that satisfy $\mid \omega \mid < \mid N \mid$ and $\mid \omega \mid < S_\ell$ - they are g modes.

We will discuss them in more detail in the next two subsections.

1.2.2 p Modes

These modes are trapped between a turning point $r = r_t$ and the surface of the star. The location of the inner turning point is determined where $S_\ell = \omega$, *i.e.*:

$$\frac{c^2(r_t)}{r_t^2} = \frac{\omega^2}{\ell(\ell+1)}. \tag{1.49}$$

For p modes, we typically have $\omega \gg N$, where N is the Brunt-Väisälä frequency. Then, K_s can be approximated by:

$$K_s(r) \simeq \frac{1}{c^2}(\omega^2 - S_\ell^2).. \tag{1.50}$$

Here the dynamics of the p modes are only determined by the variation of the sound speed with the radius r. These modes are acoustic standing waves, where the restoring force is dominated by pressure. In figure 1.1 the region where the p modes propagates is clearly shown.

The radial wave number k_r is given by:

$$k_r^2 = \frac{\omega^2 - S_\ell^2}{c^2}. \tag{1.51}$$

Sound speed increases towards the stellar interior, and the modes propagate faster. From equation 1.51 it follows that when c increases, then k decreases until it becomes zero (turning point). When this happens the wave travels only horizontally (no radial displacement). This can be seen in figure 1.1. Also, the angular degree ℓ and the location of the turning point r_t are related in such a way that r_t is smaller for smaller values of ℓ. Consequently, modes with a low angular degree ℓ will propagate deeper in the star. This is of extreme importance in the asteroseismic study of solar-like pulsators, where only modes with low angular degree ℓ can be observed. These modes carry precious informations about the deeper regions of the star.

1.2.3 g Modes

These modes propagate between two turning points whose locations are determined by the condition $N = \omega$. One turning point is located very near the center, whereas the second one is just below the base of the convective zone. The location of these turning points is independent of the angular degree ℓ.

For higher-order g modes, the frequencies are very low compared with the Lamb frequency: $\omega^2 \ll S_\ell^2$. Then, $K_s(r)$ can be written as:

$$K_s(r) \simeq \frac{1}{\omega^2}(N^2 - \omega^2)\frac{\ell(\ell+1)}{r^2}. \tag{1.52}$$

In this case the dynamics is dominated by the variation of N with r. Here gravity, acting on the density perturbation, is the dominating restoring force.

The radial wave number k_r for g modes is given by:

$$k_r^2 = \frac{\ell(\ell+1)}{r^2}\left(\frac{N^2}{\omega^2} - 1\right). \tag{1.53}$$

The order of the mode increases with decreasing frequency.

1.3 Asymptotic Theory of Stellar Pulsations

We restart from equations 1.41, which are second-order differential equations obtained through the Cowling approximation, but now we do not neglect the terms involving H_p^{-1}. Differentiating the first equation and replacing the term $\frac{dP'}{dr}$ we obtain:

$$\begin{aligned}\frac{d^2\xi_r}{dr^2} &= -\left(\frac{2}{r} - \frac{1}{\Gamma_1}H_p^{-1}\right)\frac{d\xi_r}{dr} - \left[-\frac{2}{r^2} - \frac{d}{dr}\left(\frac{1}{\Gamma_1}H_p^{-1}\right)\right]\xi_r \\ &\quad + \frac{1}{\rho c^2}\left(\frac{S_\ell^2}{\omega^2} - 1\right)\left\{\rho(\omega^2 - N^2)\xi_r + \frac{1}{\Gamma_1}H_p^{-1}P' + \left[\frac{d}{dr}\ln\left|\frac{1}{\rho c^2}\left(\frac{S_\ell^2}{\omega^2} - 1\right)\right|\right]P'\right\}.\end{aligned} \tag{1.54}$$

We can express P' as a function of ξ_r and $\frac{d\xi_r}{dr}$ by using equation 1.41. Replacing P' in equation 1.54 we obtain:

$$\frac{d^2\xi_r}{dr^2} = -\left[\frac{2}{r} + \frac{d}{dr}\ln\left|\frac{1}{\rho c^2}\left(\frac{S_\ell^2}{\omega^2} - 1\right)\right|\right]\frac{d\xi_r}{dr} + \left[K_s(r) - \tilde{h}(r)\right]\xi_r, \tag{1.55}$$

where $K_s(r)$ is given by equation 1.46, and $\tilde{h}(r)$ is defined as:

$$\begin{aligned}\tilde{h}(r) &= \left[-\frac{1}{\Gamma_1}H_p^{-1} + \frac{d}{dr}\ln\left|\frac{1}{\rho c^2}\left(\frac{S_\ell^2}{\omega^2} - 1\right)\right|\right]\left(\frac{2}{r} - \frac{1}{\Gamma_1}H_p^{-1}\right) \\ &\quad + \left[\frac{2}{r^2} + \frac{d}{dr}\left(\frac{1}{\Gamma_1}H_p^{-1}\right)\right].\end{aligned} \tag{1.56}$$

Notice that this term contains derivatives of the equilibrium quantities, thus it can be neglected in comparison with $K_s(r)$, except near the stellar surface. Equation 1.55 may also be written as:

$$\frac{d^2\xi_r}{dr^2} - \frac{d}{dr}\ln f\frac{d\xi_r}{dr} + [K_s(r) - \tilde{h}(r)]\xi_r = 0, \tag{1.57}$$

where

$$f(r) = \frac{1}{\rho r^2 c^2}\left|\frac{S_\ell^2}{\omega^2} - 1\right|. \tag{1.58}$$

To have an equation on the form of equation 1.45, without first derivatives, we introduced the new variable $\hat{\xi}_r$:

$$\xi_r(r) = f(r)^{1/2}\hat{\xi}_r(r). \tag{1.59}$$

$\hat{\xi}_r$ satisfies:

$$\frac{d^2\hat{\xi}_r}{dr^2} + [K_s(r) - h(r)]\hat{\xi}_r = 0, \tag{1.60}$$

where

$$h(r) = \tilde{h}(r) - \frac{1}{2}\frac{d^2 \ln f}{dr^2} + \frac{1}{4}\left(\frac{d\ln f}{dr}\right)^2. \tag{1.61}$$

Like $\tilde{h}(r)$, $h(r)$ is small compared with $K_s(r)$. Thus, it can be neglected and in that case equation 1.60 is similar to equation 1.45. The trapping properties of the modes are the same as those obtained previously with equation 1.45.

1.3.1 The JWKB Method

To find the solution to equation 1.60 the method JWKB (Jeffers, Wentzel, Kramers and Brillouin) is used. It assumes that the solution varies rapidly compared with equilibrium quantities, *i.e* with $K_s(r)$. Thus, the solution can be expressed as:

$$\hat{\xi}_r = a(r)\exp[i\Psi(r)], \tag{1.62}$$

where $a(r)$ is a slowly varying amplitude function, and $\Psi(r)$ is rapidly varying so that the radial wave number $k_r = \frac{d\Psi}{dr}$ is large. Replacing equation 1.62 into equation 1.60 and neglecting h we obtain:

$$\frac{d^2a(r)}{dr^2} + i\left(2k_r\frac{da(r)}{dr} + a(r)\frac{dk_r}{dr}\right) - a(r)k_r^2 = -K_s(r)a(r). \tag{1.63}$$

The imaginary part must cancel, thus we have:

$$\frac{1}{a}\frac{da(r)}{dr} = -\frac{1}{2}\frac{1}{k_r}\frac{dk_r}{dr}. \tag{1.64}$$

Then, apart from a constant factor, we obtain:

$$a(r) = |k_r|^{1/2}. \tag{1.65}$$

The asymptotic approximation consist in neglecting second derivatives. Thus, from equation 1.63 we necessary need that k_r must be chosen as:

$$k_r(r) = K(r)^{1/2}. \tag{1.66}$$

Then, with relation 1.65 finally we have:

$$a(r) = |K_s(r)|^{-1/4}. \tag{1.67}$$

The solution of equation 1.60 has to be real, and can be written as:

- If $K_s(r) > 0$

$$\hat{\xi}_r = A|K_s(r)|^{-1/4} \cos\left(\int_{r_0}^{r} K_s(r')^{1/2} dr' + \phi\right). \tag{1.68}$$

- If $K_s(r) < 0$

$$\hat{\xi}_r = |K_s(r)|^{-1/4} \left[A_+ \exp\left(\int_{r_0}^{r} K_s(r')^{1/2} dr'\right) + A_- \exp\left(-\int_{r_0}^{r} K_s(r')^{1/2} dr'\right)\right]. \tag{1.69}$$

Here A, ϕ, A_+, and A_- are real constants that will be determined by boundary conditions. As already seen before, we found the oscillatory ($K_s(r) > 0$) and exponential solutions ($K_s(r) < 0$).

To analyse the solution near the turning points, we have to connect the solution in the exponential and oscillatory regions, and apply the boundary conditions. We have a wave trapped within a region with boundaries r_1 and r_2.

Let consider a turning point r_1 such that $K_s(r) < 0$ for $r < r_1$ and $K_s(r) > 0$ for $r > r_1$. If r_1 is a zero for $K_s(r)$, then close to r_1 we approximately have:

$$K_s(r) \simeq K_1(r - r_1), \tag{1.70}$$

where K_1 is a positive constant. We introduce a new dependent variable, x, defined by:

$$x = K_1^{1/3}(r - r_1). \tag{1.71}$$

Then equation 1.60 for $\hat{\xi}_r$ can be written as:

$$\frac{d^2\hat{\xi}_r}{dx^2} = -x\hat{\xi}_r, \tag{1.72}$$

with the solution:

$$\hat{\xi}_r = C_1 A_{\rm i}(-x) + C_2 B_{\rm i}(-x), \tag{1.73}$$

where C_1 and C_2 are constants, and $A_{\rm i}$ and $B_{\rm i}$ are the Airy functions. We consider a solution that is trapped in the oscillatory region outside r_1. Thus, we need to choose C_1 and C_2 such as the solution will decrease exponentially as r decreases beneath r_1. When x is large and negative, $A_{\rm i}(-x)$ and $B_{\rm i}(-x)$ have the following asymptotic behavior:

$$A_{\rm i}(-x) \simeq \frac{1}{2\sqrt{\pi}}|x|^{-1/4}\exp\left(-\frac{2}{3}|x|^{3/2}\right) \tag{1.74}$$

$$B_{\rm i}(-x) \simeq \frac{1}{\sqrt{\pi}}|x|^{-1/4}\exp\left(\frac{2}{3}|x|^{3/2}\right). \tag{1.75}$$

Thus the requirement is $C_2 = 0$, and the solution $\hat{\xi}_r$ that satisfies the boundary condition for $r < r_1$ is:

$$\hat{\xi}_r = C_1 A_{\rm i}(-x). \tag{1.76}$$

For a large positive x, the asymptotic expression for $A_{\rm i}(-x)$ is given by:

$$A_{\rm i}(-x) \simeq \frac{1}{\sqrt{\pi}}|x|^{-1/4}\cos\left(\frac{2}{3}x^{2/3} - \frac{\pi}{4}\right). \tag{1.77}$$

This expression has to be in agreement with equation 1.68, assuming that we are in a region where both expressions are valid. Then we have:

$$\int_{r_1}^{r} K_s(r')^{1/2}dr' + \phi = \frac{2}{3}x^{3/2} - \frac{\pi}{4}, \tag{1.78}$$

and we obtain:

$$\phi = -\frac{\pi}{4}. \tag{1.79}$$

Then the solution obtained with the JWKB method satisfying the boundary condition at $r = r_1$ is:

$$\hat{\xi}_r = A_1 |K_s(r)|^{-1/4} \cos\left(\int_{r_1}^{r} K_s(r')^{1/2} dr' - \frac{\pi}{4} \right). \tag{1.80}$$

Similarly to the previous analysis, if there is a turning point r_2 such as $K_s > 0$ for $r > r_2$, and $K_s < 0$ for $r < r_2$, the asymptotic solution that decays exponentially for $r > r_2$ is:

$$\hat{\xi}_r = A_2 |K_s(r)|^{-1/4} \cos\left(\int_{r}^{r_2} K_s(r')^{1/2} dr' - \frac{\pi}{4} \right). \tag{1.81}$$

To obtain the full solution we have to match smoothly the two separated solutions on a point, let us say $r = r_f$, between r_1 and r_2. To simplify notation let us define:

$$\Psi_1 = \Psi_1(r_f) = \int_{r_1}^{r_f} K_s(r)^{1/2} dr - \frac{\pi}{4} \tag{1.82}$$

$$\Psi_2 = \Psi_2(r_f) = \int_{r_f}^{r_2} K_s(r)^{1/2} dr - \frac{\pi}{4} \tag{1.83}$$

Here we require that $\hat{\xi}_r$ and its first derivative have to be continuous at $r = r_f$. Thus we have:

$$\begin{aligned} A_1 K_s(r_f)^{-1/4} \cos\Psi_1 &= A_2 K_s(r_f)^{-1/4} \cos\Psi_2, \\ -A_1 K_s(r_f)^{-1/4} \sin\Psi_1 &= A_2 K_s(r_f)^{-1/4} \sin\Psi_2, \end{aligned} \tag{1.84}$$

where the terms coming for the differentiation of K_s have been neglected. The solution to this system is:

$$\Psi_1 + \Psi_2 = (n-1)\pi, \tag{1.85}$$

where n is an integer. Thus:

$$\int_{r_1}^{r_2} K_s(r)^{1/2} dr = \left(n - \frac{1}{2}\right)\pi. \tag{1.86}$$

Since K_s depends on the frequency, this equation determines the frequency of the modes trapped between r_1 and r_2.

Also it is possible to find an asymptotic expression for the eigenfunctions. From the definition of $\hat{\xi}_r$ (equations 1.58 and 1.59) and equation 1.80 it follows that in the oscillatory region ($r_1 < r < r_2$ we have:

$$\begin{aligned} \xi_r(r) &= \tilde{A}\rho^{-1/2} r^{-1} c^{-1} \left|\frac{S_\ell^2}{\omega^2} - 1\right|^{1/2} |K_s(r)|^{-1/4} \cos\left(\int_{r_1}^{r} K_s(r')^{1/2} dr' - \tfrac{\pi}{4}\right) \\ &= A\rho^{-1/2} r^{-1} c^{-1/2} \left|\frac{\frac{S_\ell^2}{\omega^2} - 1}{\frac{N^2}{\omega^2} - 1}\right|^{1/4} \cos\left(\int_{r_1}^{r} K_s(r')^{1/2} dr' - \tfrac{\pi}{4}\right), \end{aligned} \tag{1.87}$$

where $A = \hat{A}\omega^{-1/2}$. In the exponential regions, the solutions are:

$$\xi_r(r) \simeq \frac{1}{2} A\rho^{-1/2} r^{-1} c^{-1/2} \left|\frac{\frac{S_\ell^2}{\omega^2} - 1}{\frac{N^2}{\omega^2} - 1}\right|^{1/4} \exp\left(-\int_{r}^{r_1} K_s(r')^{1/2} dr'\right) \tag{1.88}$$

for $r < r_1$, and:

$$\xi_r(r) \simeq \frac{1}{2} A\rho^{-1/2} r^{-1} c^{-1/2} \left|\frac{\frac{S_\ell^2}{\omega^2} - 1}{\frac{N^2}{\omega^2} - 1}\right|^{1/4} \exp\left(-\int_{r_2}^{r} K_s(r')^{1/2} dr'\right) \tag{1.89}$$

for $r > r_2$.

1.3.2 Asymptotic Theory for p Modes

For p modes we have typically $\omega \gg N$. Then $K_s(r)$ can be approximated by:

$$K_s(r) \simeq \frac{1}{c^2}(\omega^2 - S_\ell^2). \tag{1.90}$$

P modes propagates between a turning point r_t and the stellar surface. These modes are standing waves where the restoring force is dominated by pressure. For standing waves, the change in phase of the eigenfunction in the radial direction must

be an integer multiple of π, apart from phase changes at the boundary region. Thus we can write:

$$\int_{r_t}^{R} \frac{(\omega^2 - S_\ell^2)^{1/2}}{c} dr = (n + \alpha)\pi, \tag{1.91}$$

where $\alpha = 1/4 + constant$. We can rewrite this equation as:

$$\int_{r_t}^{R} \left(1 - \frac{L^2 c^2}{\omega^2 r^2}\right)^{1/2} \frac{dr}{c} = \frac{(n + \alpha)\pi}{\omega}, \tag{1.92}$$

where $L^2 = \ell(\ell + 1)$. We notice that the left-hand side of this equation is a function of (L/ω). Thus, defining $\tilde{\omega} = \omega/\mathrm{L}$, it follows that:

$$\frac{(n + \alpha)\pi}{\omega} = F\left(\frac{L}{\omega}\right), \tag{1.93}$$

where

$$F(\tilde{\omega}) = \int_{r_t}^{R} \left(1 - \frac{c^2}{r^2 \tilde{\omega}^2}\right)^{1/2} \frac{dr}{c}. \tag{1.94}$$

Solar oscillations satisfy a relation of the form of equation 1.93. This was first found by (Duvall, 1982), and thus this relation is known as the *Duvall Law*. When the function $F(\tilde{\omega})$ is known from observations, equation 1.94 can be inverted to found the sound speed $c(r)$.

When ℓ is large, we have p modes trapped near the solar surface, in the outer convective zone. This convective zone can be treated adiabatically. If we assume g constant, and in the boundary condition regime where $p = \rho = 0$ at $r = R$ then we have that the sound speed is given by:

$$c^2 = \frac{g}{\mu_p}(R - r), \tag{1.95}$$

where $\mu_p = \frac{1}{\Gamma - 1}$ is an effective polytropic index of the region considered. If the layer is treated as plane parallel, so that r can be replaced by R in the integral of equation 1.94, then we have:

$$F(\tilde{\omega}) = \frac{\pi}{2}\tilde{\omega}\frac{\mu_p R}{g} \tag{1.96}$$

Thus, the dispersion relation 1.93 gives:

$$\omega^2 = (n+\alpha)L\frac{2g}{\mu_p R} \tag{1.97}$$

For low degree modes, r_t is close to the center of the star. Thus, it can be shown that equation 1.92 may be approximated by:

$$F(\tilde{\omega}) = \int_0^R \frac{dr}{c} - \frac{1}{\tilde{\omega}}\frac{\pi}{2}, \tag{1.98}$$

or,

$$\int_0^R \frac{dr}{c} - \frac{L}{\omega}\frac{\pi}{2} = \frac{(n+\alpha)\pi}{\omega}. \tag{1.99}$$

Thus, we obtain:

$$\omega = \frac{(n+\frac{L}{2}+\alpha)\pi}{\int_0^R \frac{dr}{c}}. \tag{1.100}$$

A more precise and accurate asymptotic analysis of the central regions shows that this result is correct at first order (Tassoul, 1980), but L should be replaced by $\ell + \frac{1}{2}$. Doing this we obtain:

$$\nu_{n\ell} = \frac{\omega_{n\ell}}{2\pi} \simeq (n + \frac{\ell}{2} + \frac{1}{4} + \alpha)\Delta\nu, \tag{1.101}$$

where

$$\Delta\nu = 2\left[\int_0^R \frac{dr}{c}\right]^{-1}. \tag{1.102}$$

We notice than $\Delta\nu$ is the inverse of twice the sound travel time between the center and the surface of the star. In addition, equation 1.101 predicts a uniform spacing $\Delta\nu$ of the frequencies of consecutive n orders for a given low degree ℓ. This uniform spacing is called *large separation*. It is a powerful diagnostic to study internal stellar structure. We will come back to them in the following chapters. From equation 1.101 we can also notice that modes with the same value $n + \frac{\ell}{2}$ should be almost degenerate, *i.e*:

$$\nu_{n\ell} \simeq \nu_{n-1,\ell+2} \tag{1.103}$$

Departures from Asymptotic Theory

Asymptotic theory gives us an accurate way to obtain mode frequencies at first order. Nevertheless, in real stars there are departures from this theory. Actually, these deviations give us remarkable informations about internal stellar structure. As mentioned above, equation 1.101 predicts a degeneracy between modes with the same value $n + \frac{\ell}{2}$. Departures from this relation are characterized by the so-called *small frequency separations*:

$$\delta\nu_{n\ell} = \nu_{n\ell} - \nu_{n-1\ell+2}. \tag{1.104}$$

By carrying the asymptotic expansion to higher order, it may be shown that (Tassoul, 1980):

$$\nu_{n\ell} \simeq \left(n + \frac{\ell}{2} + \frac{1}{4} + \alpha\right) - (AL^2 - \delta)\frac{\Delta\nu^2}{\nu_{n\ell}}, \tag{1.105}$$

where

$$A = \frac{1}{4\pi^2\Delta\nu}\left[\frac{c(R)}{R} - \int_0^R \frac{1}{r}\frac{dc}{dr}dr\right]. \tag{1.106}$$

Thus,

$$\delta\nu_{n\ell} \simeq -(4\ell + 6)\frac{\Delta\nu}{4\pi^2\nu_{n\ell}}\int_0^R \frac{1}{r}\frac{dc}{dr}dr, \tag{1.107}$$

where the term in the surface sound speed has been neglected. Thus, $\delta\nu_{n\ell}$ is mainly determined by the conditions in the stellar core. Also, the small separations have substantial sensitivity to the sound-speed gradient, which is sensitive to the composition profile. Then, the separations $\delta\nu_{n\ell}$ are important diagnostics of stellar evolution.

1.3.3 Asymptotic Theory for g Modes

For g modes $\omega \ll S_\ell^2$. In this case $K(r)$ can be approximated by:

$$K_s(r) \simeq \frac{\ell(\ell+1)}{r^2}\left(\frac{N^2}{\omega^2} - 1\right). \tag{1.108}$$

A mode will be trapped in a region limited by r_1 and r_2. These points are two zeros of K. Equation 1.86 is valid in this region and then the frequencies will be determined by:

$$\int_{r_1}^{r_2} L\left(\frac{N^2}{\omega^2}-1\right)^{1/2}\frac{dr}{r}=(n-1/2)\pi, \tag{1.109}$$

or

$$\int_{r_1}^{r_2} \left(\frac{N^2}{\omega^2}-1\right)^{1/2}\frac{dr}{r}=\frac{(n-1/2)\pi}{L}. \tag{1.110}$$

The left-hand side of this equation depends only on ω. Thus, in analogy with equation 1.93, equation 1.110 can be written as:

$$\frac{n-1/2}{L}=G(\omega), \tag{1.111}$$

where

$$G(\omega)=\frac{1}{\pi}\int_{r_1}^{r_2}\left(\frac{N^2}{\omega^2}-1\right)^{1/2}\frac{dr}{r}. \tag{1.112}$$

For high-order low-degree modes, we have that $\omega \ll N$ over most of the integral interval $[r_1, r_2]$. With a proper asymptotic analysis (Tassoul, 1980) it can be shown that the frequencies of low-degree high-order are given by:

$$\omega=\frac{L\int_{r_1}^{r_2} N\frac{dr}{r}}{\pi(n+\alpha_{\ell,g})}, \tag{1.113}$$

where $\alpha_{\ell,g}$ is a phase constant which depends on the boundaries of the trapping region. Equation 1.113 can also be written as:

$$\Pi=\frac{\Pi_0}{L}(n+\alpha_{\ell,g}), \tag{1.114}$$

where

$$\Pi_0=2\pi^2\left(\int_{r_1}^{r_2} N\frac{dr}{r}\right)^{-1}. \tag{1.115}$$

Thus in this case the periods are asymptotically equally spaced in the orders of the modes. The spacing decreases with increasing ℓ. We should notice that the phase term $\alpha_{\ell,g}$ will depend on whether the star has a convective or radiative core. If the star has a radiative core, then $\alpha_{\ell,g}=\ell/2+\alpha_g$, such as the period will depend

on $n + \ell/2$, like in the case of acoustic g modes (equation 1.101). In the case of a convective core, $\alpha_{\ell,g} = \alpha_g$, independent of the angular degree ℓ.

The eigenfunctions in the trapping region are given by equation 1.87. Assuming $\omega \ll S_\ell^2$ we obtain:

$$\xi_r(r) \simeq A\rho^{-1/2}r^{-3/2}\left|\frac{N^2}{\omega^2}-1\right|^{-1/4}\cos\left[L\int_{r_1}^{r}\left(\frac{N^2}{\omega^2}-1\right)^{1/2}\frac{dr'}{r'}-\frac{\pi}{4}\right]. \qquad (1.116)$$

Except close to the turning point r_1 and r_2, we can assume $N^2/\omega^2 \gg 1$ (N increases very rapidly from 0 at the centre and at the base of the convection zone). Thus we have:

$$\xi_r(r) \simeq A\omega^{1/2}\rho^{-1/2}r^{-3/2}N^{-1/2}\cos\left[L\int_{r_1}^{r}\left(\frac{N^2}{\omega^2}-1\right)^{1/2}\frac{dr'}{r'}-\frac{\pi}{4}\right] \qquad (1.117)$$

This equation gives a fairly accurate description of the eigenfunction in the trapping region, where it is expected that $\rho^{1/2}r^{3/2}N^{1/2}\xi_r$ behaves like a distorted cosine function.

For high-degree modes, the behavior will depend on the detailed properties of the buoyancy frequency. Assuming that N has a single maximum N_{max}, from equation 1.112 it follows that:

$$G(\omega) \to 0 \;\; for \;\; \omega \to N_{max} \qquad (1.118)$$

And thus,

$$\omega \to N_{max} \;\; for \;\; L \to \infty \qquad (1.119)$$

1.3.4 Cut-off frequencies and surface effects

In the computations of mode frequencies, the p-waves are assumed to be completely reflected at the stellar surface at some radius, defined as the radius of the star. This may be a good approximation for low frequencies, but a difficulty appears for increasing values. When the wavelength becomes of the same order as the atmosphere scale height, the atmosphere can no more be considered as a unique oscillating layer. The waves undergo a partial propagation outwards, which modify their energy and their frequencies. This is generally referred to as "surface effects". The cut-off frequency is generally defined as:

$$\omega_a = \frac{c_s}{2H}, \tag{1.120}$$

where c_s is the sound velocity and H the atmosphere scale height. When $\omega < \omega_a$, the wave motion decreases exponentially in the atmosphere. When $\omega > \omega_a$, the wave propagates in the atmosphere, and may no more be considered as reflected. As a consequence, no wave with a frequency larger than the cut-off frequency may be trapped inside the star.

The situation is still more complicate as in real stars the waves may have partial dissipation in the atmosphere for frequencies below the cut-off. This is supposed to be the reason why the frequencies observed for low ℓ values in the Sun are shifted compared to the ones obtained from the best solar models. These "surface effects" have to be taken into account in the comparisons between models and observations. It will be discussed in more details in the next chapter, for application to the star HD 52265.

1.4 Comparisons between models and observational data

1.4.1 Exact computations of mode frequencies

Different approaches are possible in order to obtain the fundamental parameters of a star by the means of Asteroseismology. The best precision is reached using good and accurate photometric observations as the ones provided in the last few years by MOST, WIRE, CoRoT and *Kepler* satellites, and also by high-precision and high-performance spectrographs like HARPS and SOPHIE. These observations lead to precise mode identification, which, combined with a correct modeling, allow us to obtain accurate values for the stellar mass, radius and age, and also to study different structures in the stellar interior, as the location of the convective and helium ionization zones.

Exact solutions of the hydrodynamical equations may be obtained using numerical codes. In all our work, we compute theoretical adiabatic oscillation frequencies using the code PULSE (Brassard & Charpinet, 2008). This code computes frequencies for angular degrees from 0 to 3 and for radial orders ranging typically from 4 to 100. The azimuthal order is always m= 0.

Then we use specific frequency combinations for comparison tests with observations. A very useful and widely used tool is the so-called échelle diagram. It is a frequency-frequency diagram in which the mode frequencies are plotted in ordinates,

whereas the same frequencies modulo the averaged large separation are plotted in abscissa. This will be extensively discussed in the next chapters.

1.4.2 Scaling laws

The observational data are not always precise enough for direct mode identification. There are cases where only large and small separations, and the frequency of maximun power can be deduced. In these cases information about fundamental parameters as well as evolutionary state of a star is possible through the scaling relations (Kjeldsen & Bedding, 1995) and the so-called JCD-Diagrams (Christensen-Dalsgaard, 1984). If we know the large separation, the frequency where maximum powers occurs, and the observed effective temperature, it is possible to obtain the mass and the radius of a star with the relations: .

$$\frac{M}{M_\odot} = \left(\frac{135\mu\text{Hz}}{<\Delta\nu>}\right)^4 \left(\frac{\nu_{\max}}{3050\mu\text{Hz}}\right)^3 \left(\frac{T_{\text{eff}}}{5777\text{K}}\right)^{3/2} \tag{1.121}$$

$$\frac{R}{R_\odot} = \left(\frac{135\mu\text{Hz}}{<\Delta\nu>}\right)^2 \left(\frac{\nu_{max}}{3050\mu\text{Hz}}\right) \left(\frac{T_{\text{eff}}}{5777\text{K}}\right)^{1/2}. \tag{1.122}$$

Using equations 1.121 and 1.122, the accuracy in radius and mass can be around $\sim 3\%$ and 9% respectively (Mathur et al., 2012).

1.4.3 Asterodiagrams

Another interesting approach is given by using asterodiagrams. These diagrams can tell us about the structure and the evolutionary state of a star by knowing two of the main asteroseismic observables: the large and small separation. We will first discussed the so-called "JCD-diagrams", found in the literature, and then we will present our own work on this subject.

From asymptotic theory we know that the large separation scales with the mean stellar density, relating this quantity with the mass of the star.

Also, the average small separations can be written as:

$$\delta\nu_{n\ell} \simeq (4\ell + 6)D_0, \tag{1.123}$$

where D_0 is given by:

$$D_0 \simeq -\frac{1}{4\pi^2 x_0}\int_0^R \frac{dc}{dr}\frac{dr}{r}. \tag{1.124}$$

Then, small separations are sensitive to variations in the sound speed gradient near the core.

For an ideal gas, the sound speed is given approximately by:

$$c^2 \simeq \frac{k_B T}{\mu m_u}, \tag{1.125}$$

where k_B is the Boltzmann constant, T is the temperature, μ is the mean molecular weight and m_u is the atomic mass. When a star evolves, the hydrogen content in its core decreases, leading to a increase in the mean molecular weight. Temperature in the central part of the star does not vary significantly during hydrogen burning phase. Thus, the mean molecular weight is the major determining factor affecting the sound speed in the stellar core. Consequently, the increase of the mean molecular weight when the star evolves leads to a decrease of the sound speed, reaching at minimum at the center, where the hydrogen burns fastest. D_0 decreases with increasing age. Thus, the small separations probe the stellar ages.

Motivated by these dependencies of the seismic separations, Christensen-Dalsgaard (1984) proposed to plot the average large and small frequency separations together in a ($\Delta\nu_0$, D_0) diagram, named JCD diagram for its author. An example of this diagram is shown in figure 1.2. As we can see, from the values of $\Delta\nu$ and $\delta\nu_{n\ell}$, and thus D_0, it is possible to deduce the mass and the evolutionary state of the star.

1.4.4 This work: Influence of the chemical composition on the JCD-diagrams

What has been seen so far is that in general these diagrams are used to deduce an approximate value for the mass of a given star regardless of its chemical composition. Using these values for further analysis where accuracy might be important, as for example to estimate the properties of extrasolar planets, could lead to incorrect conclusions. For this reason we performed a preliminary analysis by constructing this diagram for different chemical compositions. We use 3 different sets of ([Fe/H],Y): *(i)* 2 different values for the overall metallicity of the star: 0.30 and a solar value, and, *(ii)* for [Fe/H]=0.30 we use 2 values for the initial helium abundance: a solar value of 0.2714 (Grevesse & Noels, 1993), and Y_G, where Y_G is a helium abundance that increases with Z as expected if the local medium follows the general trend observed for the chemical evolution of galaxies (Izotov & Thuan, 2004, 2010). For [Fe/H]=0.30, Y_G is 0.303.

Model Calculations

Evolutionary tracks were calculated using the Toulouse Geneva Evolution Code (TGEC) for stellar masses of 1.05, 1.10, 1.15, 1.20 and 1.25 solar masses. The

TGEC uses the OPAL equation of state and opacities and the NACRE nuclear reaction rates. Convection was treated using the mixing length theory, with a mixing length parameter adjusted to the solar value α= 1.8. No extra-mixing nor overshooting were introduced. Within each evolutionary track we looked for models with different hydrogen abundance in the center (X_C). A different hydrogen abundance means that the star will be in a different stage of its evolution, being older with less amount of hydrogen in the center. We chose models with 5 different values of X_C: 0.66, 0.60, 0.40, 0.20 and 0.05.

For these five models, within each evolutionary track, we computed theoretical adiabatic oscillation frequencies using the code PULSE (Brassard & Charpinet, 2008). Seismic tests ($\Delta\nu_0$, $\delta\nu$ and D_0) were calculated for frequencies between 1 and 3 mHz. For the calculation of D_0 we only use the small separations between ℓ=0 and 2.

Results and Discussion

In figures 1.2, 1.3 and 1.4 we present our result for JCD diagrams for solar chemical composition, ([Fe/H]=0.30, Y_G), and ([Fe/H]=0.30, $Y_\odot$), respectively.

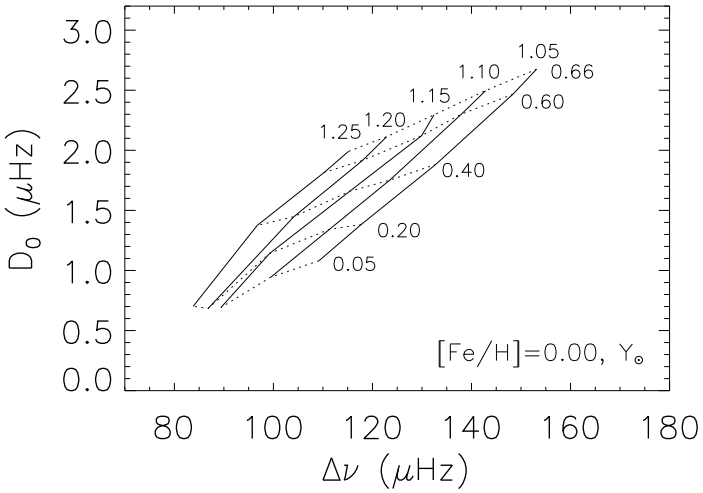

Figure 1.2: JCD diagram for a solar chemical composition.

From these diagrams we can see that the location of the curves does change when either the metallicity or the initial helium content of the star are different. In the former case, regarding the figures 1.2 and 1.4 for which the initial helium content

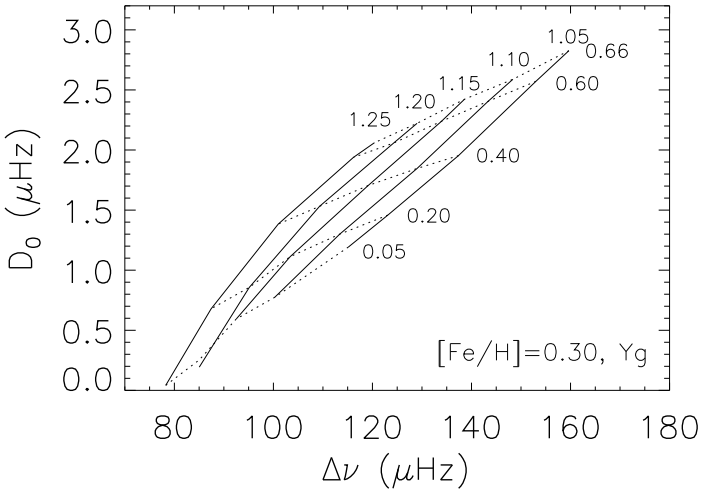

Figure 1.3: JCD diagram for [Fe/H]=0.30 and Y_G.

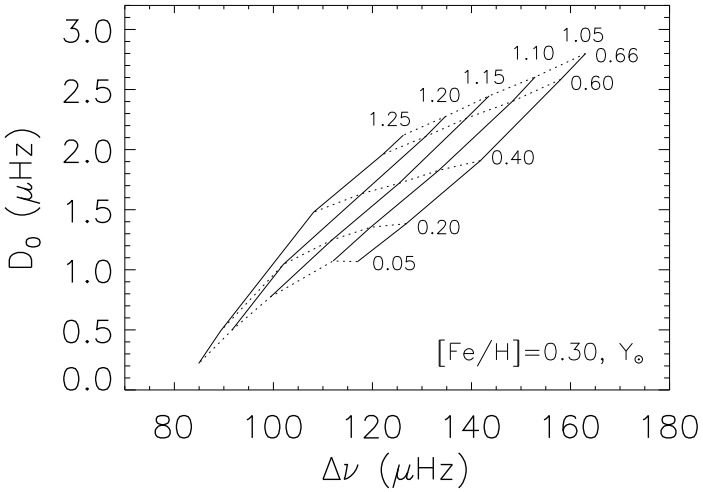

Figure 1.4: JCD diagram for [Fe/H]=0.30 and $Y_\odot$.

is the same ($Y_\odot$), we see that the curves slightly move towards the right, giving a difference of ~ 10 μHz in $\Delta\nu$, which corresponds to a difference of 5% in the mass. Now, comparing results for the same metallicity (0.30) and different helium content

we see the same trend than before for the large separations but with a smaller effect regarding the mass. The slopes of every mass line are slighty different, and the effect on the evolutionary stage of the star seems minimal as well. From figure 1.2 we can infer that this diagram starts to have a more complicated form when the hydrogen content starts to run out in the stellar core, i.e, when the star becomes a subgiant.

In any case, these diagrams are useful to obtain approximate values of the stellar parameters, but they have to be taken with caution because of the uncertainties, particularly on the internal stellar chemical composition.

Chapter 2

HD 52265

In previous chapters we have highlighted why the determination of fundamental parameters of stars is essential in several fields of stellar astrophysics. Here we present the first of the 3 stars that we have studied through asteroseismology: HD 52265. This star has an orbiting extra-solar planet discovered by (Naef et al., 2001) and (Butler et al., 2000). It was observed with the CoRoT satellite as a primary target of the asteroseismology program. This case allowed us to investigate together several subjects: asteroseismic observations from space, stellar modeling and how models can reproduce with good accuracy what is obtained from observations, the characterization of stellar properties, their accuracy and their impact on the planetary system parameters.

2.1 HD 52265

HD 52265 (HIP 33719, HR 2622) is a metal-rich main sequence star. Initially misclassified as a G0III-IV star in the Bright Star Catalog (Hoffleit & Jaschek, 1982), it is now identified as a G0V dwarf (Butler et al., 2000). It has a magnitude of V=6.301 and a parallax of $\pi = 34.54 \pm 0.40$ mas (*Hipparcos catalog*,van Leeuwen (2007)), which leads to a distance of d=28.95 ± 0.34 pc and a luminosity of log $L/L_{\odot} = 0.29 \pm 0.05$. Spectroscopic analysis showed no magnetic signature for this star (Ballot et al., 2011).

2.1.1 Previous studies

To model a star, some fundamental informations are needed in advance. The Toulouse-Geneva Evolution Code (TGEC) uses as main inputs the mass and the metallicity of the star. In addition, to compare the resulting models with observational data, informations as surface gravity, luminosity and effective temperature

have to be known. Thus, before starting any calculation with the TGEC, we perform an exhaustive search on the existing literature to gather all the possible informations about the star that we are studying. Specifically, we look for the previous spectroscopic studies that give the best accuracy about the metallicity, effective temperature and surface gravity of a star.

HD 52265 was studied by several groups, specially in the context of extrasolar planet host-stars, and also in preparation to CoRoT observations. From all spectroscopic studies we have kept for this work the studies of Gonzalez et al. (2001), Santos et al. (2004b), Fischer & Valenti (2005), Gillon & Magain (2006), and Ballot et al. (2011). The first three works were done in the context of extrasolar planet-host stars. With the discovery in 1994 of the first planet orbiting another star than the Sun (51 Peg, Mayor & Queloz (1995)), several surveys were carried out dedicated to planet hunting. As a result a rapidly growing number of extrasolar planetary systems have been discovered. The different nature of such systems compared to our own Solar system emphasized the need to obtain informations about their possible formation scenarios. This leaded to several studies concerning the properties of their parent stars, like age, mass, global metallicity, chemical abundances peculiarities and how these stars could be distinguished from those without known exoplanets. Gillon & Magain (2006) performed a spectroscopic study in preparation of CoRoT observations. They determined the atmospheric parameters and abundances for most of the CoRoT seismology program main targets, among them HD 52265. Finally, Ballot et al. (2011) performed complementary spectroscopic observations of HD 52265 during the CoRoT observations. They used the NARVAL spectropolarimeter installed on the Bernard Lyot Telescope (TBL) at Pic du Midi Observatory (France). Analyzing the spectra they obtained the atmospheric parameters, the chemical abundances and an upper limit on the average magnetic field ($\sim$ 2 G). A summary of these studies is provided in table 2.1. The atmospheric parameters derived by Takeda et al. (2005) are listed for completeness. However they will not be used in our subsequent analysis as they would indicate that HD 52265 is fastly evolving towards the subgiant phase which is in disagreement with its classification as a main sequence G0 star.

2.1.2 The planet

HD 52265 entered in the list of exoplanet host-stars by the discovery of a Jupiter-like planet made independently by Naef et al. (2001) (CORALIE Survey), and Butler et al. (2000) (Keck precision Doppler program) both using radial velocity technique. HD 52665b orbits at 0.5 AU from its parent star with a period of 119 days, and has a minimum mass of $M_p = 1.05 \pm 0.03$ M_J. As for previous findings, HD 52265 has a higher metal content than field stars in the solar neighborhood. The mass of

Table 2.1: Summary of previous spectroscopic studies of HD 52265

[Fe/H]	T_{eff}	log g	Reference
0.27 ± 0.02	6162 ± 22	4.29 ± 0.04	Gonzalez et al. (2001)
0.23 ± 0.05	6103 ± 52	4.28 ± 0.12	Santos et al. (2004b)
0.19 ± 0.03	6069 ± 15	4.12 ± 0.09	Takeda et al. (2005)
0.19 ± 0.03	6076 ± 44	4.26 ± 0.06	Fischer & Valenti (2005)
0.24 ± 0.02	6179 ± 18	4.36 ± 0.03	Gillon & Magain (2006)
0.19 ± 0.05	6100 ± 60	4.35 ± 0.09	Ballot et al. (2011)

the host-star was estimated to be around ∼1.1-1.2 $M_\odot$, and its radius around ∼ 1.2 $R_\odot$. A summary of the planet properties is given in table 2.2, and its radial velocity curve fitted with the best orbital solution is displayed in figure 2.1.

Table 2.2: Summary of HD 52265b properties (Naef et al., 2001).

HD 52265b	
M sin i	1.05 ± 0.03 M_J
Orbital period	119.6 ± 0.4 days
Semi-major axis	0.5 AU
Eccentricity	0.35 ± 0.03
ω	211 ± 6

2.2 CoRoT observations

The CoRoT satellite (Convection, Rotation and planetary Transits; Baglin et al. (2006)) was launched in December 2006 and has two major scientific programs: stellar seismology and planet search using the transit method. It is equipped with a 27 cm telescope with a 4 CCD-camera that have been providing uninterrupted high-precision photometry of thousands of stars for about 6 years. It has now stopped operation since November 2012.

In preparation to CoRoT observations, Soriano et al. (2007) performed preliminary models for HD 52265. Evolutionary tracks for overmetallic and accretion models with masses between 1.18 $M_\odot$ to 1.30 $M_\odot$ were computed with the TGEC, with metallicity values of [Fe/H]=0.19, 0.23 and 0.27. Adiabatic p-mode frequencies for angular degrees ℓ=0 to ℓ= 3 were computed with the PULSE code, and the large and small separations were calculated for each model. Échelle diagrams were

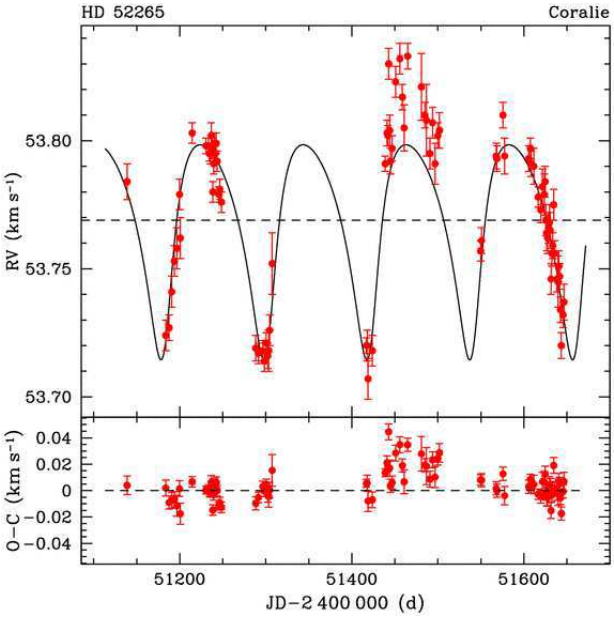

Figure 2.1: HD 52265b radial velocity curve fitted with the best orbital solution (Naef et al., 2001).

presented and analyzed, and the results were compared with five previous spectroscopic studies. The eight models whose parameters were in best agreement with spectroscopic constraints were kept for further analysis. A large separation of ~ 100 μHz was predicted for HD 52265, except for models corresponding to Takeda et al. (2005) spectroscopic constraints ($\Delta\nu \sim 75\mu$Hz), which were finally excluded.

CoRoT observations were carried out during 117 consecutive days from 13 November 2008 to 3 March 2009, during the second long run in the galactic anti-center direction (LRa02). HD 52265 was the only star with an orbiting exoplanet observed in the CoRoT main program, being an excellent opportunity to join the two CoRoT scientific programs. Asteroseismic results were presented by Ballot et al. (2011), where p-mode identifications were reported, as well as an extensive analysis of other fundamental properties of this star. As previously mentioned, a spectroscopic follow-up was done during the CoRoT observations with the NARVAL spectropolarimeter installed on TBL at the Pic du Midi Observatory (France). Analyzing the high signal-to-noise ratio spectra obtained, they found an upper limit of $\sim$ 1-2G for the magnetic field of this star. Abundances and atmospheric parameters where also obtained and they are summarized in table 2.3.

The HD 52265 light curve obtained by CoRoT is presented in figure 2.2 (top), and after removal of a third-order polynomial to correct for the slowly decreasing trend due to instrumental effects (bottom). It shows clear quasi-periodic modulations that

Table 2.3: Fundamental parameters of HD 52265 as obtained by Ballot et al. (2011)

T_{eff}	6100 ± 60 K
log g	4.35 ± 0.09
[M/H]	0.19 ± 0.05
$v \sin i$	$3.6^{+0.3}_{-1.0}$ km s^{-1}

is attributed to stellar activity, specifically to spots in the photosphere of the star. Thanks to this, a rotational period of $P_{rot} = 12.3 \pm 0.15$ days was obtained.

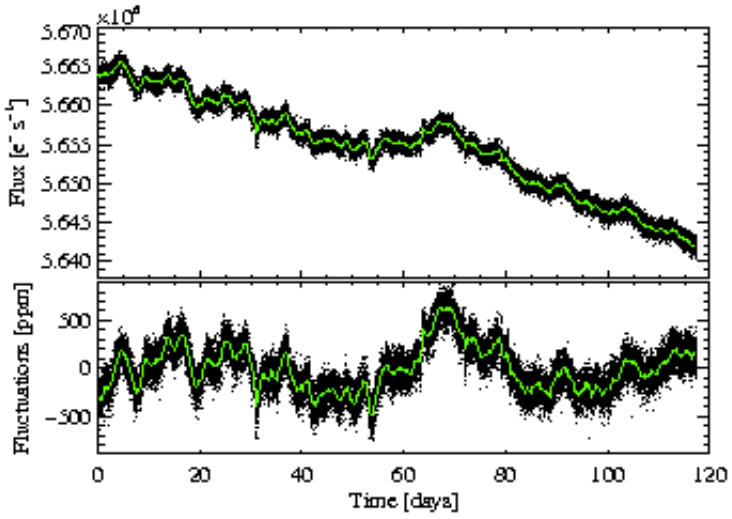

Figure 2.2: HD 52265 light curve obtained from CoRoT observations (Ballot et al., 2011)

The power spectrum density (PSD) obtained from CoRoT data is presented in figure 2.3. Around 2000 μHz a comb-like structure typical of solar-like oscillations is clearly visible. Thirty one p-modes were identified (see table 2.4), between 1500-2550 μHz, corresponding to ℓ=0 to 2. From these results, a large separation of $<\Delta\nu>$=98.4±0.1 μHz and a small separation of $<\delta\nu_{02}>$=8.1±0.2 μHz were derived.

2.3 Modeling

The exquisite results from CoRoT observations made HD 52265 a very promising object for stellar modeling. As already highlighted asteroseismology allow us to obtain with high accuracy fundamental stellar properties of stars, by comparing

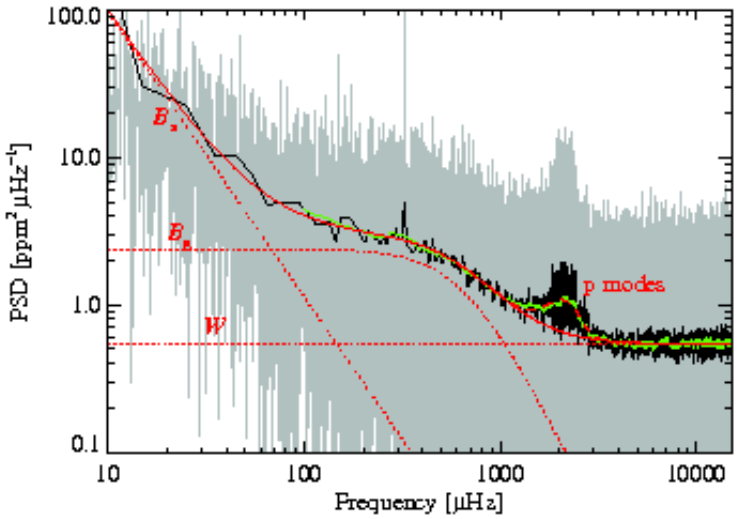

Figure 2.3: HD 52265 power density spectrum obtained from CoRoT data (Ballot et al., 2011)

Table 2.4: HD 52265 mode frequencies reported by Ballot et al. (2011)

n	ℓ	$\nu_{n,\ell}$ [μHz]	ℓ	$\nu_{n,\ell}$ [μHz]	ℓ	$\nu_{n,\ell}$ [μHz]
14	0	1509.17±0.06	1	1554.33±0.42	2	...
15	0	1606.51±0.33	1	1652.80±0.34	2	1696.88±0.53
16	0	1704.88±0.33	1	1749.85±0.48	2	1793.02±1.13
17	0	1801.15±0.56	1	1845.74±0.51	2	1890.81±0.77
18	0	1898.22±0.38	1	1943.94±0.25	2	1988.38±0.40
19	0	1996.32±0.20	1	2041.81±0.23	2	2086.48±0.45
20	0	2094.92±0.25	1	2141.32±0.20	2	2186.20±0.31
21	0	2193.75±0.23	1	2240.31±0.26	2	2284.02±0.33
22	0	2292.86±0.24	1	2338.11±0.38	2	2382.56±0.77
23	0	2389.78±0.76	1	2437.27±0.44	2	2479.76±1.14
24	0	2489.85±0.71	1	2536.07±1.19	2	...

observed and theoretical frequencies. Given the good results obtained in previous asteroseismic studies for other stars, where accurate mode identification and proper modeling were performed (ex. ι Hor, μ Arae, Vauclair et al. (2008); Soriano & Vauclair (2010)), it was expected to repeat the same success with HD 52265. In this section we describe in detail the modeling performed for this star.

2.3.1 Stellar models and frequency calculations

Stellar models were computed using the TGEC (Hui-Bon-Hoa, 2008; Théado et al., 2012), with the OPAL equation of state and opacities (Rogers & Nayfonov, 2002; Iglesias & Rogers, 1996), and the NACRE nuclear reaction rates (Angulo et al., 1999). Convection was treated using the mixing length theory (Böhm-Vitense, 1958). No overshooting nor extra-mixing were considered in our modeling. Gravitational settling of helium and metals was included using the Paquette prescription (Paquette et al., 1986; Michaud et al., 2004). Radiative accelerations on metals were introduced for some models using the SVP method (Single Value Parameter approximation, Alecian & LeBlanc (2002); LeBlanc & Alecian (2004); Théado et al. (2009)). Most evolutionary codes neglect these radiative accelerations. We perform a comparison and analyze the effect of including them or not in the next sections.

Evolutionary tracks were computed from 1.10 to 1.30 solar masses using two metallicity values and two different initial helium abundances. Initial metallicity values were chosen as [Fe/H]=0.23 and 0.30, so that after diffusion the final value lies inside the observed range. [Fe/H] represent the global overmetallicity with respect to the Sun, defined as:

$$[Fe/H] = log(Z/X)_{\star} - log(Z/X)_{\odot}, \tag{2.1}$$

where Z and X are computed at the stellar surface. As initial helium abundances we used $Y_{\odot}$ and Y_G, where $Y_{\odot}$ is the solar helium value taken from Grevesse & Noels (1993) and Y_G is the helium abundance that increases with Z following the general trend observed for chemical evolution of galaxies (Izotov & Thuan, 2004, 2010).

Adiabatic oscillation frequencies were computed using the PULSE code (Brassard & Charpinet, 2008). For several models along each evolutionary track p-modes frequencies for angular degrees from ℓ=0 to 2 were calculated. To have consistency with observations, seismic test were calculated using only angular degrees ℓ=0,1 and 2, and for a frequency range between 1500 μHz and 2550 μHz.

2.3.2 Seismic Tests

It is well known that p-modes of the same angular degree with successive radial order n are equally spaced in frequency. This is the *large separation* as defined in 1.102. In real stars the large separation slightly varies with frequency, so an average has to be used when comparing models with observations. Moreover, one has to be careful and use the same frequency range in both cases to do the computations. Taking this into account, the first step in the asteroseismic modeling process is to fit the large separations of models and observations. For that theoretical frequencies for several models along a specific evolutionary track are computed and their large

separations are measured. Thus models with the mean large separation which best fits the observational value of $\Delta\nu = 98.4 \pm 0.1$ μHz are identified. As the large separation continuously decrease as the star evolves, then only one model is found with the observed value, within the uncertainties, on each evolutionary track.

Another characteristic of p-modes is that the difference between (n,ℓ) and (n-1,ℓ+2) modes varies very slowly with frequency. These *small separations*, as defined in 1.107, are sensitive to processes occurring in the stellar core. For each set of computations done with a given initial metallicity and helium abundance, ([Fe/H],Y), we compute the small separations for those models that best fits the observational mean large separation. Then we searched for the model, in each set, that also best fit the small separation observed between modes ℓ=0 and 2, $\delta\nu = 8.1 \pm 0.2$ μHz.

Finally, detailed comparison between observed and computed échelle diagrams are made. In an échelle diagram the frequencies against the frequencies modulo the large separation are plotted. This, with some statistical test, will help us in the search for the model that best fits both the asteroseismic and spectroscopic constraints. The detailed results of this comparison for HD 52265 are presented in section 2.4.

2.3.3 Radiative accelerations

Atomic diffusion is a very important process inside stars. It can modify the atmospheric abundances and the distribution of the chemical species inside the star. This may have strong implications on the internal structure of stars (Richard et al., 2001; Michaud et al., 2004; Théado et al., 2009). Most of stellar evolution codes developed to present include the gravitational settling, but do not include the computation of radiative accelerations on heavy elements. These accelerations, which oppose gravitation, are negligible for the Sun but become significant for more massive stars (Michaud et al., 1976). To take this into account, an improved version of the TGEC was developed which includes radiative accelerations on C, N, O, Ca and Fe (Théado et al., 2012).

We used this new TGEC version to compare the frequencies calculated with or without including the radiative accelerations in the models. We computed two models with a mass of 1.28 $M_\odot$ and the same average large separation of 98.26 μHz. In one of them radiative accelerations were included and in the second one they were not. The two evolutionary tracks and the location of the models taken for the comparison are shown in figure 2.4 (left) with the difference obtained in frequencies for every ℓ (right). We obtain that the difference in the average small separations between these two models is ~ 0.01 μHz. These differences decrease with decreasing stellar mass. We conclude that for solar-type stars (masses less than 1.30 $M_\odot$) the difference in the computed frequencies is small, and thus radiative accelerations may

be neglected in our computations.

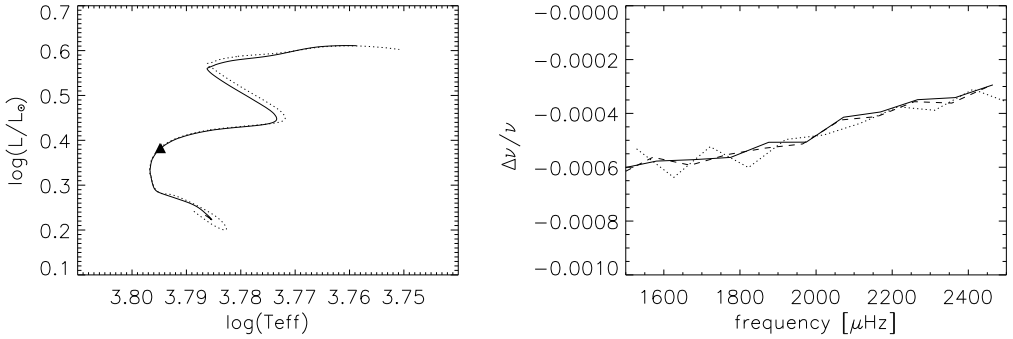

Figure 2.4: *Left*: Log $L/L_\odot$ vs $T_{\rm eff}$ diagram for 1.28 $M_\odot$ and $Y_\odot$. Tracks were calculated including radiative accelerations (solid line) and without including them (dotted line). The triangle shows the location of the models used to estimate the frequency differences. *Right*: Relative frequency differences between the two TGEC versions, for ℓ=0 (*solid line*), ℓ=1 (*dotted line*) and ℓ=2 (*dashed line*).

2.4 Results

From CoRoT results we expect HD 52265 to be a main sequence star. For this reason, the spectroscopic study from Takeda et al. (2005), for which HD 52265 would be a more evolved star was excluded (see Soriano et al. (2007) and their HR diagrams for details). Evolutionary tracks were calculated for masses ranging from 1.10 to 1.30 solar masses, for 4 different sets of ([Fe/H], Y). Some of these tracks, for every set ([Fe/H], Y), are presented in a log g- log $T_{\rm eff}$ plane and as HR diagrams in figures 2.6 and 2.8, respectively. Error boxes corresponding to the spectroscopic studies given in table 2.1 are also drawn in these figures.

As previously explained, along each evolutionary track we find one model with a mean large separation which is the closest to the observational value, computed in the same frequency range, of $\sim$ [1500-2550] μHz. The location of all these models is indicated by the iso-$<\Delta\nu>$ line, with $<\Delta\nu>$=98.4 μHz, in figures 2.6 and 2.8. For each case, we also computed the small separation between modes ℓ=0 and 2. The results of these computations, as well as the stellar properties of each model are presented in table 2.5, where metallicity, helium abundances, mass, age, log g, log $T_{\rm eff}$, log $(L/L_\odot)$, Radius, mean density, large and small separations ($<\Delta\nu>$ and $<\delta\nu_{02}>$, respectively) are indicated. In this table, the sub-index i refers to a initial state, i.e, the value given initially for the calculation of the evolutionary

track, and the sub-index s refers to the value at the surface when the evolution has already been taken place. This two values are different due to the action of atomic diffusion during stellar evolution, where the different elements are mixed or depleted in deeper layers inside the star. From observations only surface metallicity can be derived. This is the value that models should match to do a reliable comparison. As we can see from this table, for the models with the same large separation, the small separation increases with increasing mass. This mean that within every set ([Fe/H], Y), there is only one model which best fits the asteroseismic constraints.

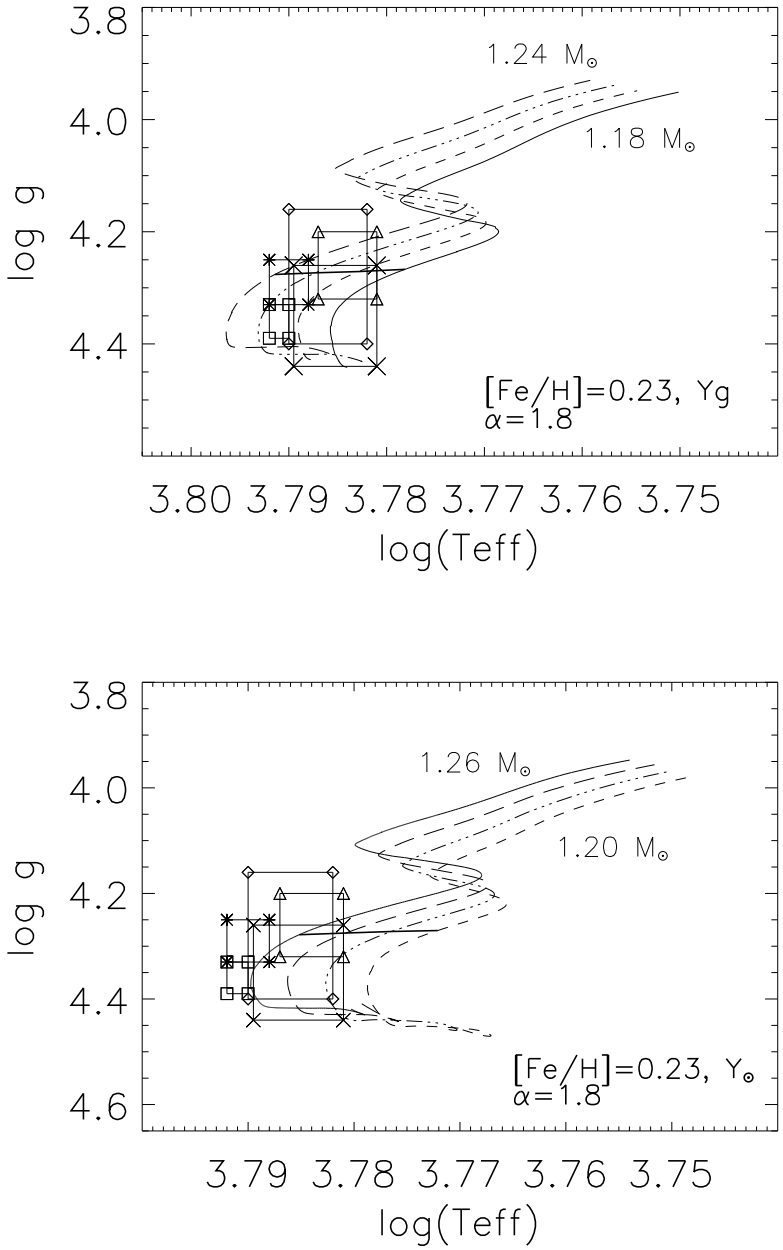

Figure 2.5: Evolutionary tracks in the log g versus log $T_{\rm eff}$ plane for [Fe/H]= 0.23 and two different values of helium abundances, for $\alpha = 1.8$ (see text for details). The symbols indicate the error boxes of Gonzalez et al. (2001) (*asterisks*), Santos et al. (2004b) (*diamonds*), Gillon & Magain (2006) (*squares*), Fischer & Valenti (2005) (*triangles*), and Ballot et al. (2011) (*crosses*). The straight thick line represents the iso-$<\Delta\nu>$ line, with $<\Delta\nu>$=98.4 μHz.

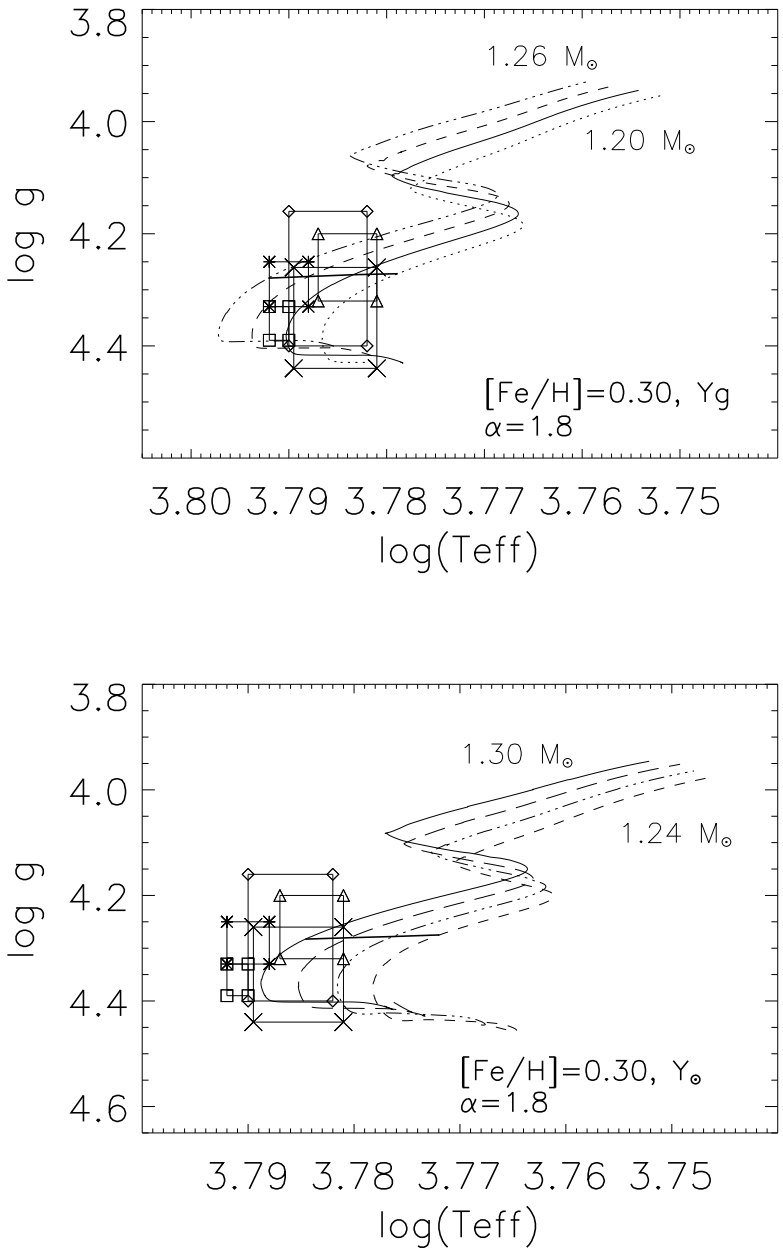

Figure 2.6: Evolutionary tracks in the log g versus log $T_{\rm eff}$ plane for [Fe/H]= 0.30 and two different values of helium abundances, for $\alpha = 1.8$ (see text for details). The symbols indicate the error boxes of Gonzalez et al. (2001) (*asterisks*), Santos et al. (2004b) (*diamonds*), Gillon & Magain (2006) (*squares*), Fischer & Valenti (2005) (*triangles*), and Ballot et al. (2011) (*crosses*). The straight thick line represents the iso-$<\Delta\nu>$ line, with $<\Delta\nu>$=98.4 μHz.

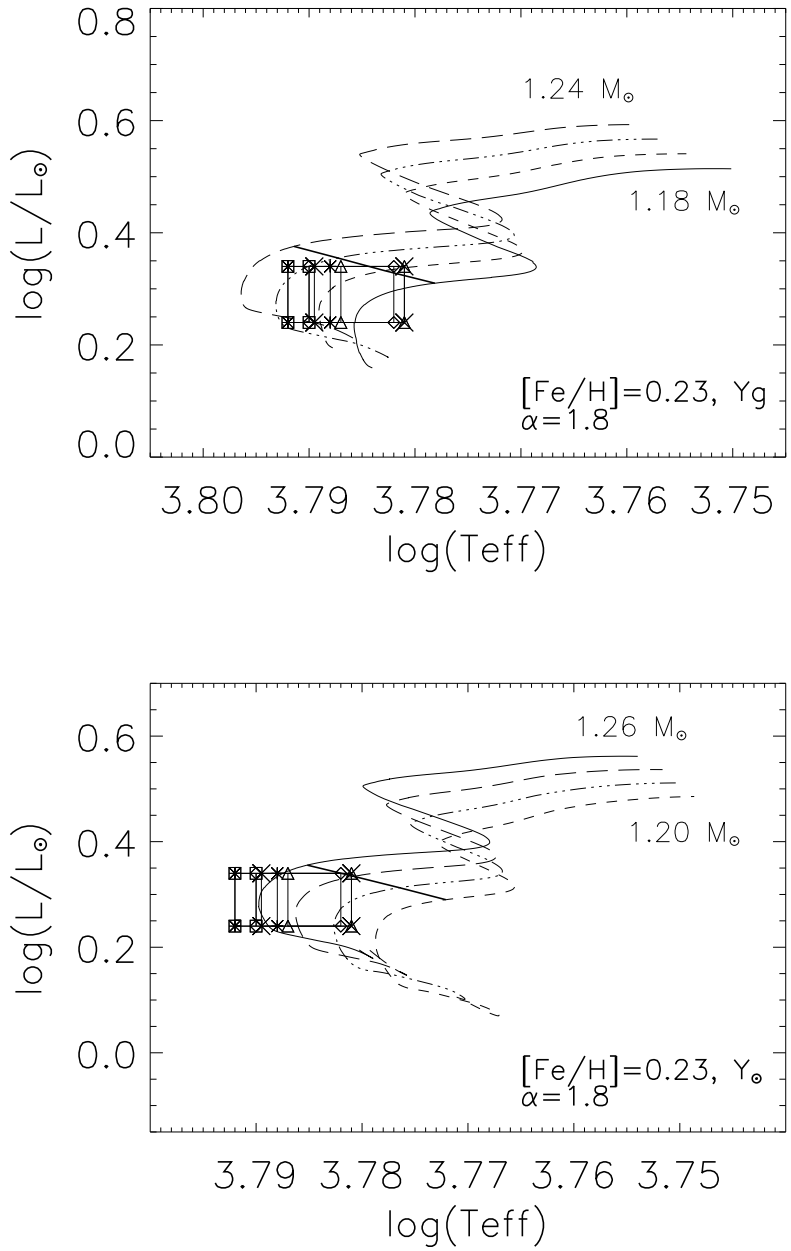

Figure 2.7: HR diagrams for $\alpha = 1.8$ and [Fe/H]=0.23. Error boxes are the same horizontally as presented in Figure 2.6, for the effective temperatures, and correspond vertically to the luminosity uncertainty. The straight thick line represents the iso-$<\Delta\nu>$ line, with $<\Delta\nu>$=98.4 μHz.

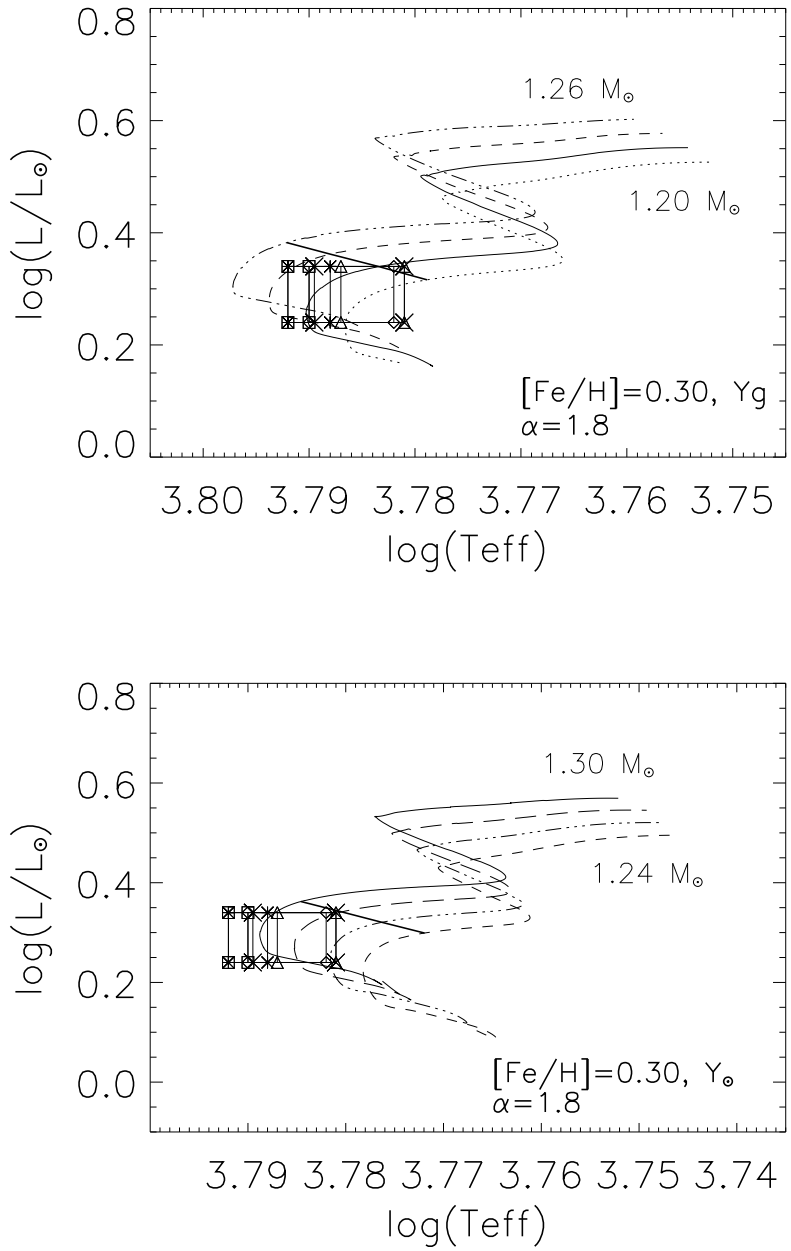

Figure 2.8: HR diagrams for $\alpha = 1.8$ and [Fe/H]=0.30. Error boxes are the same horizontally as presented in Figure 2.6, for the effective temperatures, and correspond vertically to the luminosity uncertainty. The straight thick line represents the iso-$<\Delta\nu>$ line, with $<\Delta\nu>$=98.4 μHz.

Table 2.5: Examples of models with α=1.8, without surface effects. $[Fe/H]_i$ and Y_i refer to initial metallicity and helium abundance of the models, and, $[Fe/H]_s$ and Y_s to the surface metallicity and helium abundance of the models at the given age (see text for details).

$[Fe/H]_i$	Y_i	$M/M_\odot$	Age [Gyr]	$[Fe/H]_s$	Y_s	log g [K]	log $T_{\rm eff}$	log $(L/L_\odot)$	$R/R_\odot$	M/R^3 [solar units]	$<\Delta\nu>$ [μHz]	$<\delta\nu_{02}>$ [μHz]
0.23	0.293	1.18	3.682	0.16	0.246	4.267	3.778	0.310	1.328	0.50	98.31	7.08
0.23	0.293	1.20	3.204	0.16	0.246	4.271	3.782	0.332	1.333	0.51	98.38	7.54
0.23	0.293	1.22	2.820	0.16	0.248	4.273	3.787	0.355	1.341	0.51	98.36	7.85
0.23	0.293	1.24	2.416	0.15	0.242	4.276	3.791	0.375	1.347	0.51	98.34	8.33
0.23	0.271	1.22	3.756	0.16	0.228	4.272	3.776	0.312	1.343	0.51	98.33	7.11
0.23	0.271	1.24	3.283	0.16	0.228	4.275	3.780	0.334	1.349	0.51	98.31	7.80
0.23	0.271	1.26	2.865	0.16	0.230	4.278	3.785	0.355	1.355	0.51	98.34	7.98
0.23	0.271	1.28	2.461	0.16	0.227	4.281	3.789	0.375	1.361	0.51	98.35	8.30
0.30	0.303	1.20	3.209	0.23	0.257	4.271	3.778	0.316	1.333	0.51	98.42	7.35
0.30	0.303	1.22	2.820	0.23	0.258	4.273	3.783	0.339	1.341	0.51	98.35	7.75
0.30	0.303	1.24	2.431	0.23	0.261	4.276	3.787	0.361	1.347	0.51	98.38	8.11
0.30	0.303	1.26	2.072	0.22	0.254	4.282	3.792	0.382	1.354	0.51	98.38	8.59
0.30	0.271	1.24	3.771	0.23	0.231	4.274	3.771	0.299	1.349	0.51	98.32	7.11
0.30	0.271	1.26	3.293	0.23	0.231	4.277	3.776	0.320	1.356	0.51	98.37	7.64
0.30	0.271	1.28	2.865	0.23	0.231	4.280	3.780	0.341	1.363	0.51	98.34	7.87
0.30	0.271	1.30	2.476	0.24	0.233	4.282	3.784	0.362	1.369	0.51	98.39	8.25

Now we proceed to the detailed frequency-frequency comparison between models and observations. For that we plotted the échelle diagrams for the four models, one for each set ([Fe/H], Y), that better represents the asteroseismic constraints. The results of this comparison are presented in figure 2.9, where theoretical and observational frequencies are plotted against each other in the same échelle diagram. In spite of the good match seen in this figure, we have to emphasize that it was accomplished by shifting all the model frequencies by $\sim$ 20 μHz. This offset is attributed to surface effects induced by the wave behavior in the outer layers of the star. We discuss these effects and their impact on the results in the following section.

2.4.1 Surface Effects

It is well known that current stellar models fail in correctly representing the near-surface layers of the stars. As a consequence, there is a systematic offset between observed and computed frequencies. This offset is independent of the angular degree ℓ and increases with frequency. This has been studied in the case of the Sun, and a similar offset is expected to occur in other stars.

Using the Sun as a reference, Kjeldsen et al. (2008) suggested that the near-surface corrections to the frequencies may be approximated by:

$$\nu_{\rm obs}(n) - \nu_{\rm best}(n) = a \left[\frac{\nu_{\rm obs}(n)}{\nu_0} \right]^b , \tag{2.2}$$

where $\nu_{obs}(n)$ are the observed ℓ=0 frequencies with radial order n, $\nu_{best}(n)$ are the calculated frequencies for the best model, where the best model is the model that most closely describes the star but still fails to correctly model the near-surface layers, and ν_0 is a constant reference frequency chosen to be the frequency at the maximum amplitude in the power spectrum.

If we have a reference model with frequencies $\nu_{ref}(n)$ that is close to the best model, then it follows that:

$$\nu_{\rm best}(n) = r\nu_{\rm ref}(n). \tag{2.3}$$

Thus we have:

$$\nu_{\rm obs}(n) - r\nu_{\rm ref}(n) = a \left[\frac{\nu_{\rm obs}(n)}{\nu_0} \right]^b . \tag{2.4}$$

Differentiating, combining and rearranging the equations we obtain:

$$r = (b-1) \left[b \frac{\nu_{\rm ref}(n)}{\nu_{\rm obs}(n)} - \frac{\Delta\nu_{\rm ref}(n)}{\Delta\nu_{\rm obs}(n)} \right], \tag{2.5}$$

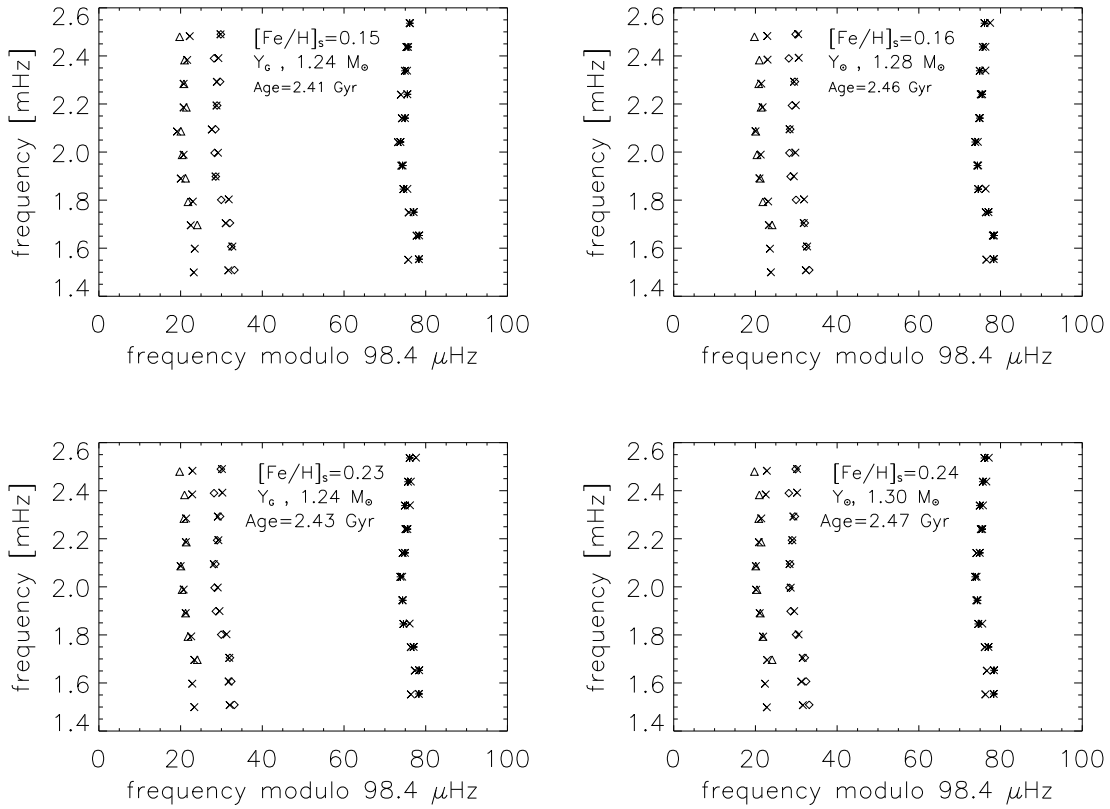

Figure 2.9: Échelle diagrams for the best-fit model found for each set of evolutionary tracks calculated with $\alpha = 1.8$. In this set of models, the surface effects are not included. The model frequencies (*crosses*) are compared to the observed frequencies, which are represented as diamonds (ℓ=0), asterisks (ℓ=1), and triangles (ℓ=2).To obtain these best fits, we had to shift the model frequencies by respectively (top left, top right, bottom left, bottom right) 27, 25, 24, and 22 μHz (see text).

and

$$b = \left[r \frac{\Delta\nu_{\rm ref}(n)}{\Delta\nu_{\rm obs}(n)} \right] \left[r \frac{\nu_{\rm ref}(n)}{\nu_{\rm obs}(n)} - 1 \right]^{-1} . \tag{2.6}$$

Knowing either b or r, then it is possible to obtain a from equation 2.4. Applying this method to the Sun, Kjeldsen et al. (2008) found $b = 4.90$, using the model S (Christensen-Dalsgaard et al., 1996) as best model and Solar data from the GOLF instrument on the SOHO spacecraft (Lazrek et al., 1997). This value of b was determined using the nine strongest radial modes in the solar data. They found that repeating the analysis for a different number of modes could change the value of b from 4.4 to 5.25, but the values of a varied less than 0.1 μHz in all cases.

In the same way that Kjeldsen et al. (2008) applied their analysis to α Cen A, α Cen B and β Hyi, we applied their method to HD 52265. Calculating the frequency corrections that we have to apply to our models, we calculate the large separations with the new set of corrected frequencies, which leads to a new average large separation, $<\Delta\nu^*>$, slightly larger than the observational one. We proceed as before to compute models for the same sets of values of the helium abundance and metallicity, using $\alpha = 1.8$. The results are presented in table 2.6. In figure 2.10 the échelle diagrams for the new best-fit models are displayed. In these graphs, the frequency corrections were applied to the new model frequencies in order to compare them directly with the observations.

Table 2.6: Examples of models with α=1.8, including surface effects. Listed properties are the same as in table 2.5. Here $<\Delta\nu^*>$ represents the Kjeldsen et al. (2008)-corrected large separations.

$[Fe/H]_i$	Y_i	$M/M_\odot$	Age [Gyr]	$[Fe/H]_s$	Y_s	log g [K]	log $T_{\rm eff}$	log $(L/L_\odot)$	$R/R_\odot$	M/R^3 [solar units]	$<\Delta\nu^*>$ [μHz]	$<\Delta\nu>$ [μHz]	$<\delta\nu_{02}>$ [μHz]
0.23	0.293	1.18	3.548	0.16	0.247	4.275	3.779	0.306	1.315	0.52	99.67	98.27	7.27
0.23	0.293	1.20	3.069	0.16	0.247	4.279	3.784	0.328	1.321	0.52	99.68	98.27	7.83
0.23	0.293	1.22	2.670	0.16	0.250	4.282	3.788	0.350	1.327	0.52	99.86	98.19	8.11
0.23	0.293	1.24	2.251	0.16	0.244	4.287	3.792	0.369	1.331	0.52	100.08	98.19	8.47
0.23	0.271	1.20	4.130	0.16	0.228	4.276	3.773	0.287	1.325	0.52	99.51	98.19	6.85
0.23	0.271	1.22	3.622	0.16	0.228	4.279	3.777	0.309	1.331	0.52	99.56	98.18	7.26
0.23	0.271	1.24	3.149	0.16	0.229	4.283	3.781	0.330	1.337	0.52	99.61	98.18	7.69
0.23	0.271	1.26	2.730	0.16	0.232	4.286	3.786	0.351	1.343	0.52	99.62	98.07	8.11
0.30	0.303	1.20	3.089	0.23	0.258	4.278	3.780	0.313	1.322	0.52	99.64	98.32	7.70
0.30	0.303	1.22	2.685	0.23	0.260	4.282	3.784	0.335	1.328	0.52	99.72	98.13	7.94
0.30	0.303	1.24	2.296	0.24	0.263	4.285	3.788	0.357	1.334	0.52	99.78	98.15	8.34
0.30	0.303	1.26	1.907	0.23	0.257	4.290	3.793	0.376	1.337	0.52	100.23	98.20	8.84
0.30	0.271	1.24	3.637	0.23	0.231	4.282	3.773	0.295	1.338	0.52	99.56	98.27	7.30
0.30	0.271	1.26	3.173	0.23	0.232	4.284	3.777	0.317	1.345	0.52	99.50	98.16	7.64
0.30	0.271	1.28	2.730	0.23	0.233	4.288	3.781	0.337	1.351	0.52	99.64	98.09	8.08
0.30	0.271	1.30	2.326	0.23	0.236	4.291	3.785	0.357	1.355	0.52	99.80	98.20	8.52

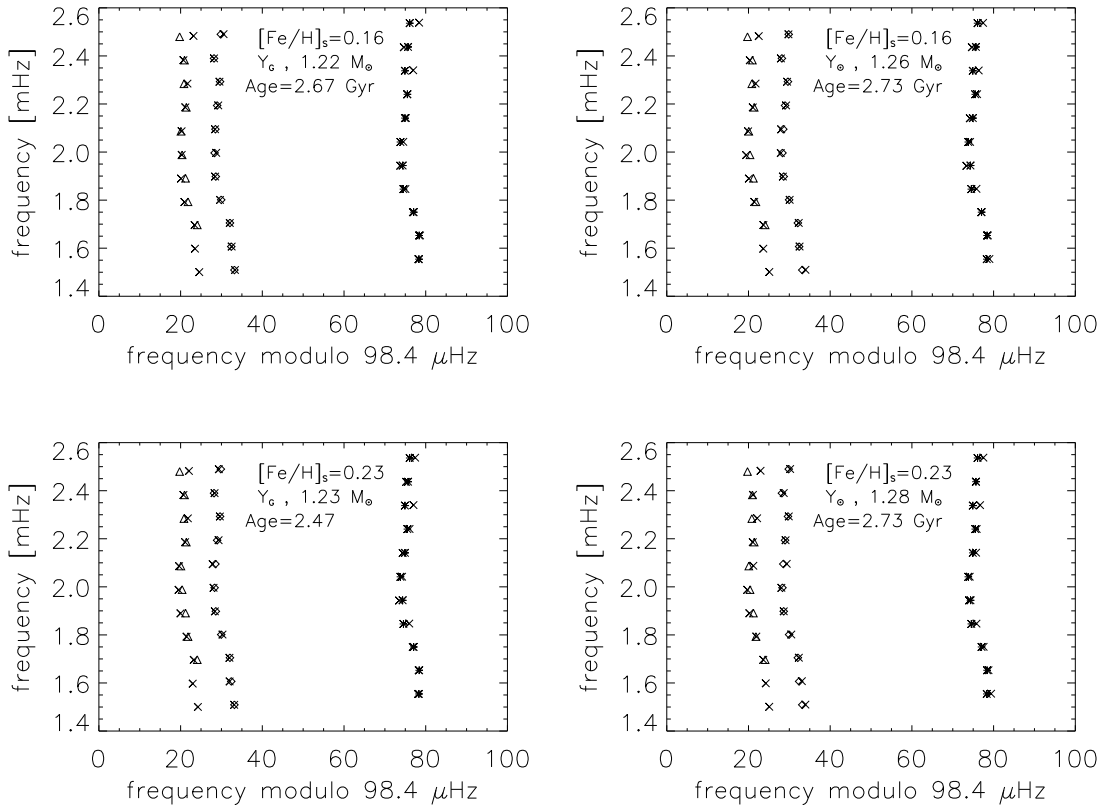

Figure 2.10: Échelle diagrams for the best-fit model, including near-surface corrections, as proposed by Kjeldsen et al. (2008),found for each set of evolutionary tracks calculated with $\alpha = 1.8$, in comparison with the observed frequencies. The symbols are the same as those in figure 2.9.

2.5 Discussion

In table 2.7 we present the properties of the best-fit models that were obtained for the four different sets of chemical composition. These models were computed with a mixing length parameter adjusted to 1.8 (solar value), their frequencies have been corrected for surface effects and the computed large and small separations are the closest to the observational values in the sample. We also give χ^2 values for the comparisons of the three $\ell = 0, 1, 2$ ridges in the échelle diagrams.

Table 2.7: Best-fit models obtained with the TGEC code, including near surface corrections.

$M/M_\odot$	$L/L_\odot$	$R/R_\odot$	log g	$T_{\rm eff}$ [K]	age [Gyr]	$[Fe/H]_i$	Y_i	$[Fe/H]_s$	Y_s	χ^2
1.22	2.239	1.327	4.282	6143	2.670	0.23	0.293	0.16	0.250	5.06
1.23	2.219	1.330	4.283	6120	2.476	0.30	0.303	0.23	0.262	3.34
1.26	2.244	1.343	4.286	6109	2.730	0.23	0.271	0.16	0.232	6.42
1.28	2.173	1.351	4.288	6043	2.730	0.30	0.271	0.23	0.233	3.51

By looking table 2.7 one can derive several conclusions. Regarding stellar gravity, we see that it is derived with a precision of 0.1%, which is the standard in asteroseismic analysis. The mass and the age depend basically on the chosen value for the initial helium content. For a low helium value, the mass is between 1.26 $M_\odot$ and 1.28 $M_\odot$, with an age of 2.73 Gyr, whereas for a higher helium abundance the mass is slightly lower (around 1.22-1.23 $M_\odot$) as well as the age (2.48 to 2.68 Gyr). In any cases, the radius and the luminosity of the star are derived with an accuracy of $\sim$ 2% and $\sim$ 3% respectively.

To continue further in our analysis it is necessary to have a closer insight to the different asteroseismic tests. Figure 2.11 displays the large and small separations as a function of frequencies for both, observations and best-fit models. We can see that the pattern observed in the large separation is well-reproduced by the models. For the small separations, we also obtain a very good agreement, except for the 2 points at high frequencies (2284 μHz and 2479 μHz). This suggests that the uncertainties given in Ballot et al. (2011) for these points could have been underestimated.

We can go further and compare the effective temperatures derived with the models with the spectroscopic observations. In figure 2.12 we present the location of the best-fit models in the log g -log $T_{\rm eff}$ diagram, together with the error boxes of the different spectroscopic studies. As previously found in the cases of μ Arae (Soriano & Vauclair, 2010)and ι Hor (Vauclair et al., 2008), the effective temperatures of the best-fit models are lower for lower initial helium abundances and higher for lower metallicities. In the present case, we found that the model with the highest metallicity and lowest helium abundance, represented by a black square in figure 2.12,

is at the coolest limit of the observational error boxes and thus may be excluded from the sample on spectroscopic grounds. Then, we derive the stellar parameters for HD 52265 from the mean value of the resulting three models. This final result is presented in table 2.8.

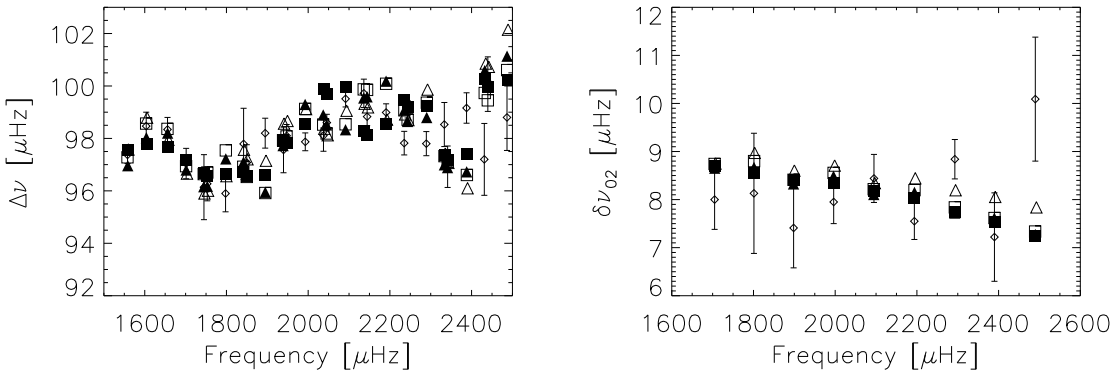

Figure 2.11: Comparisons between the large separations (*left*) and the small separations (*right*) of the four best-fit models indicated by squares for models with $[Fe/H]_s$=0.23 ($[Fe/H]_i$=0.30) and triangles for models with $[Fe/H]_s$=0.16 ($[Fe/H]_i$=0.23). Empty symbols are used to indicate a helium abundance according to Y_g, and filled symbols for a solar helium abundance. Observations are represented as white diamonds.

Table 2.8: Final results for the parameters of the exoplanet-host star HD 52265 obtained with the TGEC code.

$M/M_\odot = 1.24 \pm 0.02$	$[Fe/H]_i = 0.27 \pm 0.04$
$R/R_\odot = 1.33 \pm 0.02$	$Y_i = 0.28 \pm 0.02$
$L/L_\odot = 2.23 \pm 0.03$	$[Fe/H]_s = 0.20 \pm 0.04$
$\log g = 4.284 \pm 0.002$	$Y_s = 0.25 \pm 0.02$
Age (Gyr) $= 2.6 \pm 0.2$	$T_{\rm eff}$ (K) $= 6120 \pm 20$

We can also compare our results with what is obtained from the scaling relations proposed by Kjeldsen & Bedding (1995). As previously shown, if we know the average large separation, $<\Delta\nu>$, the frequency of maximum power, ν_{max}, and the observed effective temperature, $T_{\rm eff}$, then it is possible to obtain first estimates of the mass and the radius of a star by:

$$\frac{M}{M_\odot} = \left(\frac{135\mu\mathrm{Hz}}{<\Delta\nu>}\right)^4 \left(\frac{\nu_{\rm max}}{3050\mu\mathrm{Hz}}\right)^3 \left(\frac{T_{\rm eff}}{5777\mathrm{K}}\right)^{3/2} \tag{2.7}$$

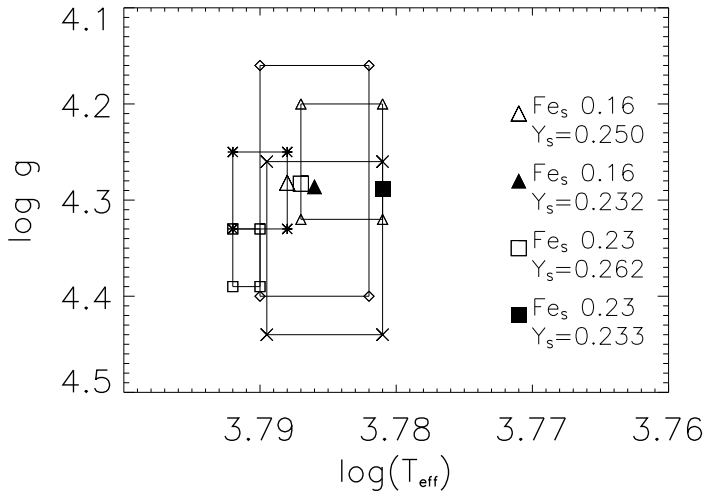

Figure 2.12: Location of the best-fit models in the log g vs log $T_{\rm eff}$ plane. Triangles indicate models with $[{\rm Fe/H}]_s$=0.16 ($[{\rm Fe/H}]_i$=0.23), and squares indicate models with $[{\rm Fe/H}]_s$=0.23 ($[{\rm Fe/H}]_i$=0.30). Filled symbols are used to show the models with a solar helium value. Error boxes correspond to the Gonzalez et al. (2001) (*asterisks*), Santos et al. (2004b) (*diamonds*), Gillon & Magain (2006) (*squares*), Fischer & Valenti (2005) (*triangles*), and Ballot et al. (2011) (*crosses*) spectroscopic studies.

$$\frac{R}{R_\odot} = \left(\frac{135\mu{\rm Hz}}{<\Delta\nu>}\right)^2 \left(\frac{\nu_{max}}{3050\mu{\rm Hz}}\right) \left(\frac{T_{\rm eff}}{5777{\rm K}}\right)^{1/2}, \tag{2.8}$$

where $<\Delta\nu>_\odot$=135 μHz, $\nu_{max,\odot}$=3050 μHz, and $T_{{\rm eff},\odot}$=5777 K, are the values for the large separations, the frequency at maximum power and the effective temperature for the Sun, respectively. In the case of HD 52265, the frequency at the maximum power is ν_{max}=2090$\pm$20 μHz (Ballot et al., 2011). With a large separation of 98.4 μHz and a effective temperature of 6100 K we obtain from these relations M=1.23 $M_\odot$ and R=1.32 $R_\odot$. Comparing with table 2.8, we can see that these values are in good agreement, within uncertainties, with our results.

2.5.1 Automatic Fits

Giving the growing amount of data and improvements that space mission as *Kepler* and CoRoT have brought to the asteroseismic community several automatic codes has been developed to analyze large data sets. In particular, we refer to automatic codes that are capable to give as a result the best-fit model. We compare our results

with two of such codes: SEEK (Quirion et al., 2010) and the Asteroseismic Modeling Portal (AMP, Metcalfe et al. (2009)).

SEEK uses a large grid of stellar models computed with the Aarhus Stellar Evolution Code (ASTEC) to search for the best-fit model corresponding to a seismic observed star. The models in the grid are constructed using the OPAL equation of state (Rogers & Nayfonov, 2002), with the solar mixture of Grevesse & Sauval (1998). Convection is treated using the mixing-length theory (Böhm-Vitense, 1958). Diffusion and overshooting are not considered in the calculations. SEEK generates a grid of models with different combinations of metallicity (Z), initial hydrogen mass fraction (X_i) and mixing length parameter α. The input parameters are the large and small separations ($<\Delta\nu>$, $\delta\nu_{02}$), the spectroscopic observables ($T_{\rm eff}$, log g, [Fe/H]), and the absolute magnitude. The oscillation properties of the models are computed using the Aarhus Adiabatic Pulsation Code (ADIPLS, Christensen-Dalsgaard (2008)). Once this is done, SEEK compares the observational constraints with every model in the grid using Bayesian statistics. As final result the code gives the stellar mass, radius and age of the star. In the case of HD 52265 the results are:

- Mass = 1.27 $\pm$ 0.03 $M_\odot$
- Radius = 1.34 $\pm$ 0.02 $R_\odot$
- Age = 2.37 $\pm$ 0.29 Gyr

AMP is capable to compare individual frequencies in order to obtain a best-fit model. The AMP provides a web-based interface for deriving stellar parameters of sun-like stars from asteroseismic data and it was developed at the High Altitude Observatory and Computational & Information Systems Laboratory of the National Center of Atmospheric Research. As SEEK, it uses ASTEC to calculate different models and ADIPLS to calculate their theoretical adiabatic frequencies. With a parallel genetic algorithm (Metcalfe & Charbonneau, 2003) it optimizes the match between the models and the observations. But in the case of AMP, computations with ASTEC include diffusion following the prescription of Michaud & Proffitt (1993). Models are generated with different combinations of metallicity (Z), initial helium mass fraction (Y_i) and mixing length parameter α. AMP also includes an empirical correction for near-surface effects following the prescription proposed in Kjeldsen et al. (2008). This correction is applied before comparing the corrected frequencies with observations. Then the code performs two χ^2 statistical tests, one using the mode frequencies, χ^2_{seis}, and the other using the non-asteroseismic observables ($T_{\rm eff}$, log g, [Fe/H], L), χ^2_{spec}. AMP will optimize the mean of the two χ^2 values to finally obtain the best-fit model. In the case of HD 52265, two different computations were done with AMP. One, that we call AMP(a), using all the observed frequencies given by Ballot et al. (2011), and a second one, AMP(b), using only the most reliable

frequencies ((ℓ=0, n=14), (ℓ=1, n=14), and (ℓ=2, n=15), were excluded). The resulting parameters given by AMP are given in table 2.9.

Table 2.9: Final results for the parameters of the exoplanet-host star HD 52265 obtained from AMP automatic analysis, using (a) all observed frequencies or (b) only the most reliable frequencies (see text for details).

Parameter	AMP(a)	AMP(b)
$M/M_\odot$	1.22	1.20
$R/R_\odot$	1.321	1.310
$L/L_\odot$	2.058	2.128
log g	4.282	4.282
[Fe/H]	0.23	0.215
Y	0.280	0.298
Age (Gyr)	3.00	2.38
$T_{\rm eff}$	6019	6097

Regarding the mass and age, we see that the values given by SEEK are slightly larger than our results using TGEC and PULSE codes, and the age is younger. In the case of AMP, the results are in good agreement with our results. Interestingly, AMP also found solution for a mass of 1.27 $M_\odot$ with both, a small Y (about 0.26) and a young age (about 2.7 Gyr), but the χ^2 tests showed that this result corresponds to a secondary minimum, but is not the best-fit solution. Thus, we consider that the difference seen between our results with TGEC and PULSE codes, and SEEK may be related to: (i) a different initial helium abundance, (ii) to slightly different values of the average large and small separations as given by Gizon et al. (2012), or (iii) to this fact that SEEK result corresponds to a secondary minimum of probability as shown with the AMP code.

2.6 Conclusions and Perspectives

We have performed a detailed modeling of the exoplanet host-star HD 52265. This star was observed by the CoRoT satellite during 117 consecutive nights, as one of the main targets. As a result of these observations, 33 p-mode where identified by Ballot et al. (2011). The precise observing results obtained from CoRoT observations allowed us to perform a precise determination of the stellar properties of this star. Stellar evolutionary tracks where calculated using the TGEC and frequencies for several models where obtained using the PULSE code. A comparison between computed models and observational frequencies gave as a result the stellar parameters presented in table 2.8, with high accuracy.

We demonstrated that detailed modeling is necessary to correctly characterize a star through asteroseismology.

Chapter 3

94 Cet

More than 50% of stars are in multiple systems. Furthermore, secondary non-stellar bodies are sometimes found to orbit these systems. 94 Cet is a binary system, where an exoplanet has been found in orbit at a distance of 1.42 AU. Studying this star was also motivated by given the fact that another star with characteristics very similar to 94 Cet had already been studied by means of asteroseismology: β Virginis. This gave us a unique opportunity of exploring the properties of 94 Cet system, but also of comparing it with a star with similar characteristics but without exoplanet. Additionally, the radius for this star has been accurately measured with interferometry. The expected mass for 94 Cet was large enough for radiative accelerations on heavy elements to become important in the atomic diffusion processes. This gives the opportunity to test internal physics by comparing models calculated with radiative accelerations taken into account and models where they are not included.

3.1 94 Cet

94 Cet (HD 19994, HR 962, HIP 14954, GJ 128) is classified as an F8V star. Its visual magnitude is V = 5.08. Its parallax, $\pi = 44.29 \pm 0.28$ (*Hipparcos catalogue*, van Leeuwen (2007)) puts it at a distance of d = 22.38 pc. Its secondary companion is an M dwarf, which is 6.4 magnitudes fainter at a distance of $\sim$ 100 AU (Hale, 1994).

3.1.1 The planet: HD 19994b

A Jupiter-like companion to HD 19994 was first announced by Queloz et al. (2000). A more precise orbital solution was later given by Mayor et al. (2004). Discovered by using radial velocity technique, this planet has a minimum mass of 1.68 M_J and orbits its parent star at a distance of 1.42 AU with a period of $\sim$ 535.7 days. A summary of the properties of HD 19994b is given in Table 3.1

Table 3.1: Summary of HD 19994b properties (Mayor et al., 2004)

HD 19994b	
M sin i	1.68 M_J
Orbital period	535.7 ± 3.1 days
Semi-major axis	1.42 AU
Eccentricity	0.30 ± 0.04
ω	211 ± 6

3.2 Previous Spectroscopic Studies

Several spectroscopic studies exist about this star. We have chosen for our final comparisons the most recent studies with the best precision. Roughly speaking, we found two kinds of results for the metallicity of this star: overmetallic or with a nearly solar metallicity value. The former studies mainly focused on the exoplanet host-star status of 94 Cet. On this road we found the studies of Santos et al. (2001, 2003, 2004b), where they present 94 Cet among their general studies of statistical properties, metal-rich nature and spectroscopic [Fe/H] for exoplanet-host stars. We take the metallicity values of their 2004 work, which presents a summary and a revision of the previous results, giving separately the values for [Fe/H] obtained with four different instruments: CORALIE, FEROS, UVES and UES.

Valenti & Fischer (2005) also included 94 Cet in their spectroscopic study of cool stars. Their results are in agreement with Santos et al. results, i.e., this star shows an overmetallicity with respect to the Sun. They also gave estimates of the age, mass and radius of the star. Maldonado et al. (2012) analyzed spectroscopically 94 Cet as part of their survey about metallicity of solar-like stars with debris disk and planets. Their results are also in agreement with the previous mentioned analyses.

In the latter studies 94 Cet is presented as a star with a nearly solar metallicity. Edvardsson et al. (1993), in their study of the chemical evolution of the galactic disk, gave a metallicity of 0.09 for 94 Cet. Eight years later, Smith et al. (2001) in their work exclusively focused on 94 Cet and its abundance distribution, gave a similar metallic value for this star.

A summary of the spectroscopic studies previously mentioned is presented in table 3.2

3.3 β Virginis

β Virginis is an F9V star, at a distance of 11 pc with a visual magnitude of V=3.61 (*Simbad Astronomical Data Base*). This star is part of a binary system, and also

Table 3.2: Summary of previous spectroscopic studies of 94 Cet

[Fe/H]	T_{eff}	log g	Reference
0.09 ± 0.10	6104 ± 100	4.10 ± 0.20	Edvardsson et al. (1993)
0.09 ± 0.05	6030 ± 20	3.95 ± 0.05	Smith et al. (2001)
0.25 ± 0.08	6217 ± 67	4.29 ± 0.08	Santos et al. (2004b) (CORALIE)
0.32 ± 0.07	6290 ± 58	4.31 ± 0.13	Santos et al. (2004b) (FEROS)
0.19 ± 0.05	6121 ± 33	4.06 ± 0.05	Santos et al. (2004b) (UVES)
0.21 ± 0.08	6132 ± 67	4.11 ± 0.23	Santos et al. (2004b) (UES)
0.19 ± 0.03	6188 ± 44	4.24 ± 0.06	Valenti & Fischer (2005)
0.19 ± 0.03	6140 ± 31	4.35 ± 0.09	Maldonado et al. (2012)

shows an overmetallicity compared to the Sun ([Fe/H]$\simeq$0.14). The characteristics of this star, very close to those of 94 Cet, could give an opportunity to compare their properties, and thus look at the differences between two similar stars, the first one harboring an exoplanet and the second one without any detected exoplanet.

Solar like oscillations in β Virginis were first reported by Martic et al. (2004), but no individual mode identification was possible. One year later Carrier et al. (2005) were successful in this task. Using CORALIE observations they reported 31 individual p-modes frequencies, for angular degrees ℓ=0,1,2. A large separation of $\Delta\nu$=72.1 μHz and a small separation of $\delta\nu_{02}$=6.3 μHz were derived. The identified modes and the observational ED diagram are presented in table 3.3 and figure 3.1, respectively.

Asteroseismic stellar modeling for β Virginis was carried out by Eggenberger & Carrier (2006). They computed different evolutionary tracks using the Geneva Evolution Code, and they include rotation in their calculations. As non asteroseismic input they used the metallicity ([Fe/H]=0.14±0.05), luminosity ($L/L_{\odot}$=3.51±0.10), effective temperature (T_{eff}=6130±50 K) and surface velocity (V$\sim$4.3 km.s^{-1}). Theoretical mode frequencies were computed using the Aarhus adiabatic pulsation package (after ADPLS, Christensen-Dalsgaard (2008)).

Using a χ^2 minimization algorithm they obtained two models that well reproduce the asteroseismic and non-asteroseismic constraints: (i) A main-sequence model with M=1.28±0.03 $M_{\odot}$, and (ii) a post-main sequence model with a mass of M=1.21±0.02 $M_{\odot}$.

To investigate if there were any difference by applying our method, we performed a new modeling for this star. We took a metallicity of [Fe/H]=0.14 as input. Evolutionary tracks for masses ranging from 1.16 $M_{\odot}$ to 1.34 $M_{\odot}$ were computed for two different helium abundances: (i) Y_{ini}= $Y_{\odot}$, and (ii) Y_{ini}= Y_g. Large and small separations were computed within the observational range, i.e, [0.7-2.4] mHz. For each evolutionary track, only one model fits closely the observational large sepa-

Table 3.3: Observational oscillation frequencies (in μHz) for β Virginis (from Carrier et al. (2005))

n	ℓ=0	ℓ=1	ℓ=2
8	...	731.7	...
9	...	803.0	...
10	...	...	...
11	909.3	...	...
12	982.6	...	...
13	...	...	...
14	1124.9	1153.7	...
15	...	1224.2	1258.7
16	1266.1	1298.7	...
17	1340.7	1370.6	1403.2
18	1409.6	1442.5	1478.5 *
19	...	1516.2	1553.6
20	...	1587.1	1624.1
21	...	...	1697.8
22	1702.7	...	1766.5
23	...	1807.3	...
24	1846.6	1875.2	...
25	...	...	...
26	...	...	...
27	...	...	...
28	2135.4	2168.4	...
29	...	2238.2	...
30	...	...	...
31	2352.5	...	...

ration, and for each case of chemical composition, only one model closely fits the observational small separation.

In Figure 3.2 we present the échelle diagram for the model which best fits the observational asteroseismic constraints in the case of ([Fe/H], Y_i) = (0.21, Y_G). Due to the dispersion in the frequencies of the identified modes, as given by Carrier et al 2005, it is quite difficult to fit a realistic model on these observations and the precision is poor. We conclude that the available observations are not precise enough to allow an accurate modeling for β Virginis.

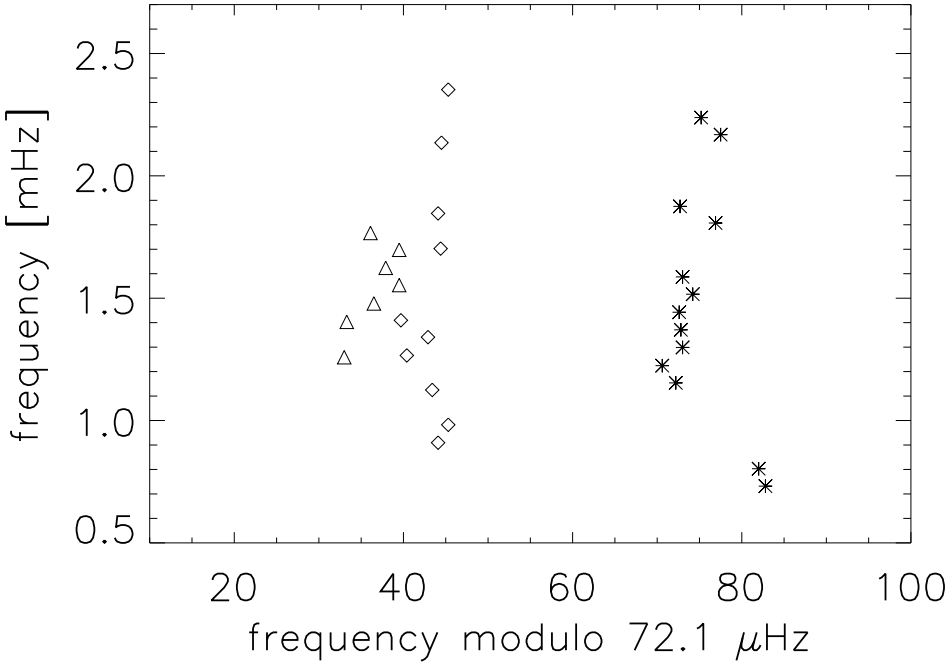

Figure 3.1: Observational échelle diagram for β Virginis, where modes with angular degree ℓ= 0 (*diamonds*), ℓ=1 (*asterisks*), and $\ell = 2$ (*triangles*) are displayed. The average large separation is $<\Delta\nu>\sim$72.1 μHz (Carrier et al., 2005).

3.4 94 Cet observations

94 Cet was observed with the HARPS spectrograph mounted on the ESO 3.6 m telescope, at La Silla Observatory, Chile. The observations were carried out during 7 consecutive nights in November 2007.

3.5 Mode Identification

The Fourier transform was first analyzed with the Period 04 code to extract the most important peaks. However, due to aliasing it may happen that high amplitude peaks are combinations of aliases instead of real modes. For this reason we preferred studying manually the Fourier transform, step by step, using the window function to pick out the real peaks and eliminate the surrounding aliases. We then used stellar models to identify the modes corresponding to the detected frequencies. This

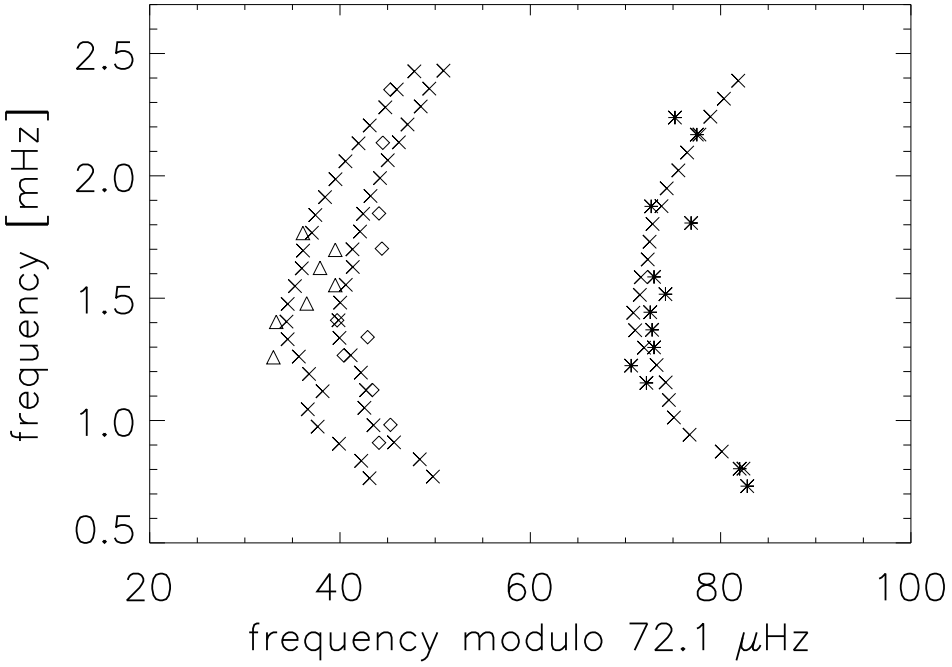

Figure 3.2: Échelle diagram for a model computed with ([Fe/H], Y_i) = (0.21, Y_G), and a mass of 1.24 $M_\odot$. Theoretical frequencies are represented by crosses and observational frequencies by diamonds (ℓ= 0), asterisks (ℓ=1), and triangles ($\ell = 2$).

method was quite successful, allowing us to recognize 28 modes in a convincing way.

The frequencies of these identified modes are given in table 3.4 with an uncertainty evaluated to 1μHz. The corresponding ED is shown in figure 3.3. The average large and small separations are $<\Delta\nu>$= 64.3 μHz and $<\delta\nu_{0,2}>$= 4.6 μHz.

3.6 Stellar Modeling

To model this star we proceed as before, computing several evolutionary tracks using the TGEC (Hui-Bon-Hoa, 2008; Théado et al., 2012). Evolutionary tracks were obtained for a mass range between 1.20 and 1.46 solar masses. The initial metallicity was chosen as $[Fe/H]_i$=0.26, so as to obtain a final value of 0.15 to 0.20 at the stellar surface, which corresponds to the highest observed metallicity. The helium value was assumed to follow the chemical evolution law.

Models were computed using a mixing length parameter adjusted to the so-

Table 3.4: Identified p-mode frequencies (in μHz) for 94 Cet.

ℓ=0	ℓ=1	ℓ=2	ℓ=3
1223.8	...	1217.4	1246.4
1287.5	1316.1	1282.5	1309.4
1351.7	1376.7	1347.2	...
1414.5	1442.0	1410.8	1438.0
1478.6	1507.4	1475.0	1501.4
1543.0	1571.6	...	...
1608.0	1635.0	...	1628.0
1674.0	1702.0	1669.0	...

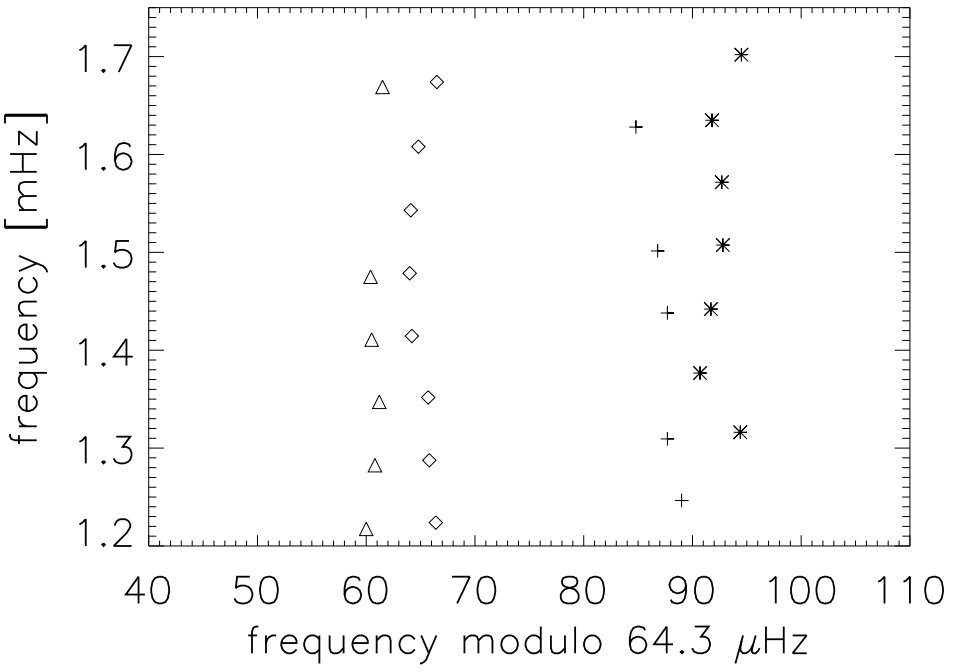

Figure 3.3: Observational échelle diagram for 94 Cet, where modes with angular degree ℓ= 0 (*diamonds*), ℓ=1 (*asterisks*), ℓ = 2 (*triangles*), and ℓ=3 (*plus signs*) are displayed. The average large separation is $<\Delta\nu>\sim$64.3 μHz.

lar value (α =1.8). We calculated models with and without overshooting. For those models with overshooting (hereafter OV models), an overshooting parameter of 0.2 H_p and 0.3 H_p, where H_p is the pressure scale height, were used. Addition-

ally, models were calculated with the last version of TGEC which includes radiative accelerations on heavy elements in diffusion processes.

Theoretical mode frequencies were calculated using the PULSE code (Brassard & Charpinet, 2008). Seismic tests were calculated within the observational range, i.e between [1200-1700] μHz, and for angular degrees ℓ =0,1,2 and 3. Large separation for several models within each evolutionary track were obtained, and we keep the model which best fits the observational large separation of $\Delta\nu = 64.3$ μHz for further analysis. Then, small separation were calculated for these *best-fit models*.

3.7 Results

3.7.1 Models without overshooting

Evolutionary tracks in the log g - log T_{eff} plane, computed without overshooting, are presented in figure 3.4. For clarity only masses from 1.34 to 1.46 are shown. Error boxes from the different spectroscopic studies presented in table 3.2 are also displayed. Stellar properties of the best-fit model within each evolutionary track are presented in table 3.5, which includes initial overall metallicity and helium abundances (columns 1 and 2), mass (column 3), age (column 4), final surface metallicity and helium abundance (column 5 and 6), log g (column 7), log T_{eff} (column 8), log $L/L_{\odot}$ (column 9) , radius (column 10), M/R^3 (column 11), and large and small separations (column 12 and 13). It is worth noticing that M/R^3 is the same for every model, as expected from the asymptotic theory.

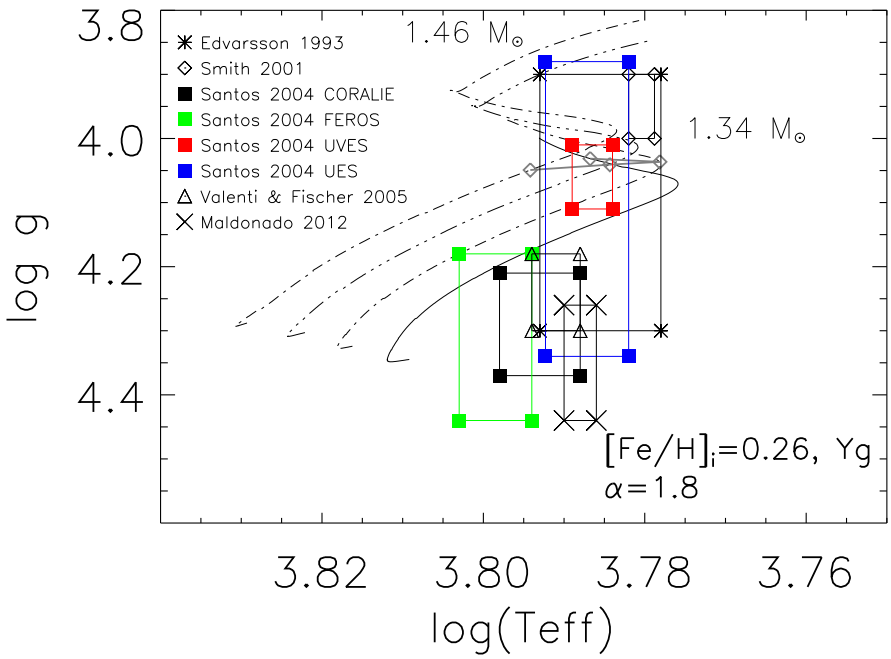

Figure 3.4: Evolutionary tracks in the log g versus log $T_{\rm eff}$ plane calculated with [Fe/H]$_i$ =0.26, Y$_i$=Y$_G$ and without overshooting. The symbols indicate the error boxes of Edvardsson et al. (1993) (*asterisks*), Smith et al. (2001) (*diamonds*), Santos et al. (2004b) (CORALIE) (*black squares*), Santos et al. (2004b) (FEROS) (*green squares*), Santos et al. (2004b) (UVES) (*red squares*), Santos et al. (2004b) (UES) (*blue squares*), Valenti & Fischer (2005) (*triangles*), and Maldonado et al. (2012) (*crosses*). The straight thick line represents the iso-$<\Delta\nu>$ line, with $<\Delta\nu>$=64.3 μHz.

Table 3.5: Examples of models with α=1.8, without overshooting. [Fe/H]$_i$ and Y$_i$ refer to initial metallicity and helium abundance of the model, and, [Fe/H]$_s$ and Y$_s$ to the surface metallicity of the model at the given age (see text for details).

[Fe/H]$_i$	Y$_i$	M/M$_\odot$	Age [Gyr]	[Fe/H]$_s$	Y$_s$	log g [K]	log $T_{\rm eff}$	log $(L/L_\odot)$	R/R$_\odot$	M/R^3 [solar units]	$<\Delta\nu>$ [μHz]	$<\delta\nu_{02}>$ [μHz]	χ^2
0.26	0.297	1.38	2.989	0.20	0.252	4.036	3.778	0.608	1.873	0.21	64.35	4.12	2.40
0.26	0.297	1.42	2.553	0.19	0.245	4.041	3.784	0.641	1.891	0.21	64.18	4.36	2.90
0.26	0.297	1.46	2.120	0.15	0.218	4.049	3.794	0.684	1.899	0.21	64.35	4.58	3.11

The best-fit model must fulfill the observational constraints, i.e, the (log g, log $T_{\rm eff}$, [Fe/H]) triplet. In this respect, the 1.46 $M_{\odot}$ model has to be ejected as it falls outside all error boxes from spectroscopic studies. Additionally, the model with M=1.38 $M_{\odot}$, is located just at the turn-off (TO) point. At this stage, the star begins a rapid core contraction phase followed by the hydrogen shell burning during the sub-giant phase. This rapid phase is unlikely to be observed and 94 Cet is definitely not in the sub-giant phase of evolution. In consequence, this model is also discarded.

3.7.2 Radiative accelerations

As already mentioned in previous chapters, a new version of the TGEC that includes radiative accelerations on heavy elements has been developed (Théado et al., 2012). We used this version to compute several evolutionary tracks with the same inputs as for the tracks computed without overshooting and without radiative accelerations. The range of masses in this case goes from 1.24 to 1.42 $M_{\odot}$. Some of these tracks are presented in the log g - log $T_{\rm eff}$ plane in figure 3.5. For clarity, only masses from 1.34 to 1.42 are shown. Error boxes from the different spectroscopic studies presented in table 3.2 are also displayed.

For masses above 1.30-1.40 $M_{\odot}$ we expect that the effects of radiative acceleration on heavy elements begin to be important, thus having consequences on the evolution and the chemical composition of the star. In table 3.6 the properties of the best-fit models (the model with the $<\Delta\nu>$ closest to the observational value) in each evolutionary track for 1.38 and 1.42 solar masses are presented. The columns are the same as for table 3.5. These are the models that better approach the observational non-asteroseismic contraints (see also figure 3.5). The 1.38 $M_{\odot}$ model falls at the TO point, so this model is discarded for further analysis. If we look at specific stellar properties, we see some differences in age for the M=1.42 $M_{\odot}$ model, when comparing it with the same mass model computed without the radiative accelerations.

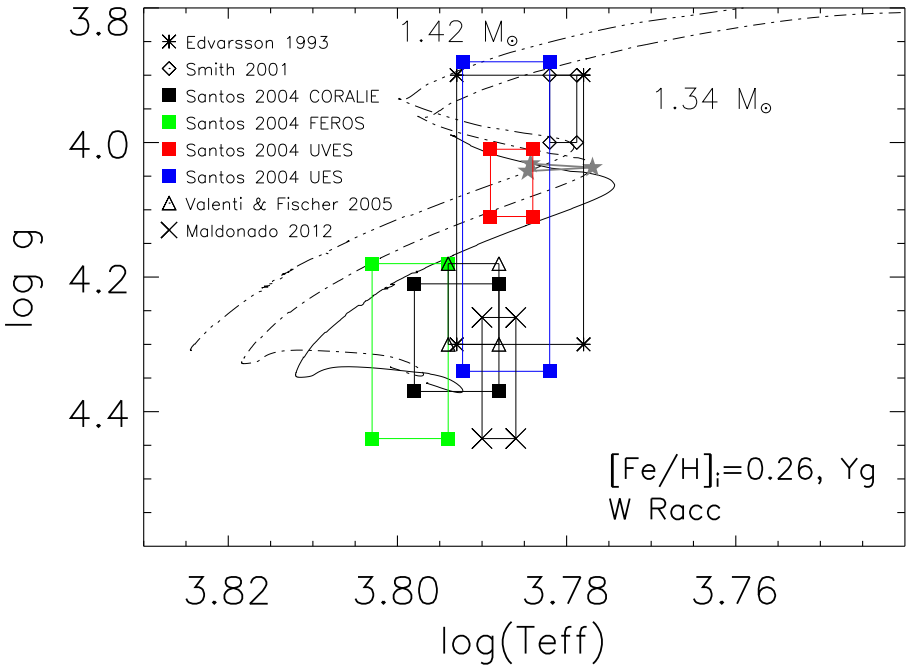

Figure 3.5: Evolutionary tracks in the log g versus log $T_{\rm eff}$ plane calculated with $[Fe/H]_i$ =0.26, Y_i=Y_G, obtained using the new version of the TGEC that includes radiative accelerations on heavy elements. No overshooting was considered. Error boxes displayed are the same as figure 3.4. The straight thick line represents the iso-$<\Delta\nu>$ line, with $<\Delta\nu>$=64.3 μHz.

Table 3.6: Examples of models computed with radiative accelerations included. No overshooting was considered for the computations. The columns are the same as in table 3.5.

$[Fe/H]_i$	Y_i	$M/M_\odot$	Age [Gyr]	$[Fe/H]_s$	Y_s	$\log g$ [K]	$\log T_{\rm eff}$	$\log (L/L_\odot)$	$R/R_\odot$	M/R^3 [solar units]	$<\Delta\nu>$ [μHz]	$<\delta\nu_{02}>$ [μHz]	χ^2
0.26	0.297	1.38	2.987	0.19	0.253	4.037	3.777	0.603	1.872	0.21	64.35	4.21	2.41
0.26	0.297	1.42	2.517	0.18	0.244	4.042	3.784	0.641	1.887	0.21	64.27	4.38	2.88

We would expect that the surface metallicity would not decrease as much when considering radiative accelerations in the computations. Nevertheless, it is not the case for the models discussed here. This is due to the fact that by [Fe/H] we refer to the overall metallicity, which considers several chemical elements, not only Fe. The effect of radiative accelerations depends on the chemical element considered. Thus, some elements diffuse downwards more than others, depending on the efficiency of the radiative accelerations to compensate gravitational settling. To have a closer look at the effects of radiative accelerations in the stellar interior we present in figure 3.6 the sound speed profile of the two models with M=1.42 $M_\odot$. Also, we plot the profiles for C, N, O for the same models (figures 3.7 to 3.9), and the profiles for Ca and Fe for the models where radiative accelerations were considered (figures 3.10 and 3.11).

Now we explore the differences in frequencies between models with and without radiative accelerations. In figure 3.12 the small separations $\delta\nu_{02}$ for models with M=1.38 $M_\odot$ and M=1.42 $M_\odot$ are shown. Red triangles represent the models calculated with the version of the TGEC without radiative accelerations, and green stars models including radiative accelerations. We notice that the differences between the two code versions increase for the 1.42 $M_\odot$ model. This is in agreement with what we expect when radiative accelerations are included in the calculations, since their effects are more important for more massive stars. Additionally, as small separations are sensitive to the stellar core, where nuclear reactions take place determining the evolution of the star, these differences also indicate the effect induced on the stellar age by the different chemical composition, when the radiative accelerations begin to be important.

We have also plotted the relative difference of small separations for these models. They are presented in figure 3.13. They confirm our conclusion from figure 3.12. The difference on the small separations for the 1.38 $M_\odot$ model are ~ 0.025 μHz, and for the 1.42 $M_\odot$ model ~ 0.15 μHz.

3.7.3 Models with overshooting

We also computed models considering overshooting in the stellar core. Overshooting is introduced as an extension of the convective core, with an extension of $\alpha_{ov}H_p$, where H_p is the pressure scale height. Here we consider two cases: (i) α_{ov}=0.20 and (ii) α_{ov}=0.30.

The evolutionary tracks computed using these overshooting parameters are presented in figure 3.14, for α_{ov}=0.20, and in figure 3.15 for α_{ov}=0.30. Models for masses ranging from 1.20 to 1.46 $M_\odot$ were computed, but for clarity only tracks from 1.34 to 1.46 are presented on the figures. Comparing figures 3.14 and 3.15 with the case without overshooting (figure 3.4) we see that when overshooting is

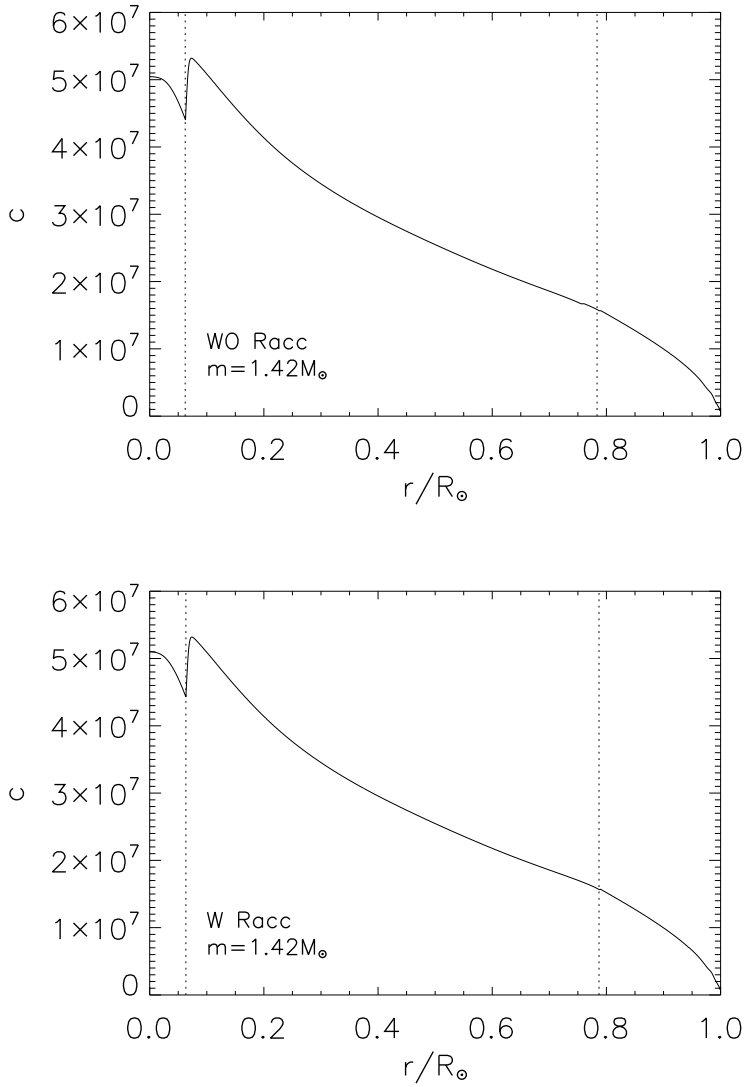

Figure 3.6: Sound speed profiles for models with M=1.42 $M_\odot$, calculated with (*upper panel*) and without (*lower panel*) including radiative accelerations. Dashed lines indicate the base of the surface convection zone and the boundary of the convective core.

included, the star passes more time on its main-sequence (MS) phase, *retarding* evolution. This is clearly seen in 1.34 and 1.38 $M_\odot$ models: while they fall in TO and SGB phase in the case without overshooting, they are still in the MS for models with overshooting. Stellar parameters for different models, from 1.38 to 1.46 $M_\odot$ are presented in table 3.7. Columns are the same as in tables 3.5 and 3.6.

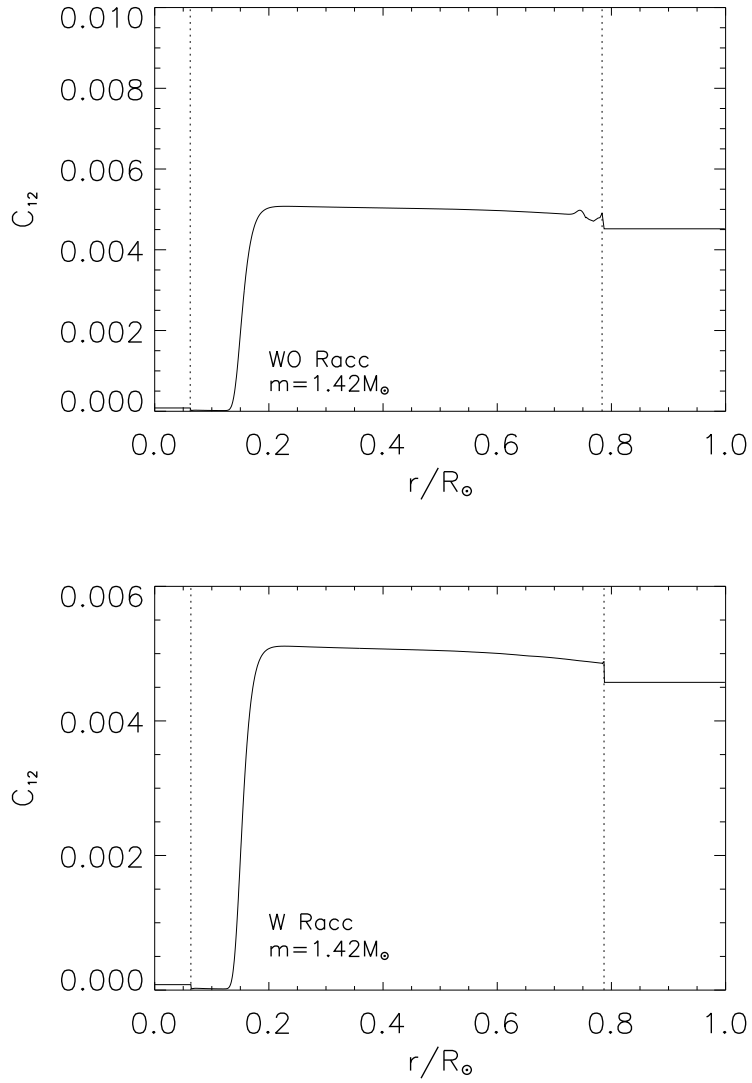

Figure 3.7: C profiles for models with M=1.42 $M_{\odot}$, calculated with (*upper panel*) and without (*lower panel*) including radiative accelerations. Dashed lines indicate the base of the surface convection zone and the boundary of the convective core.

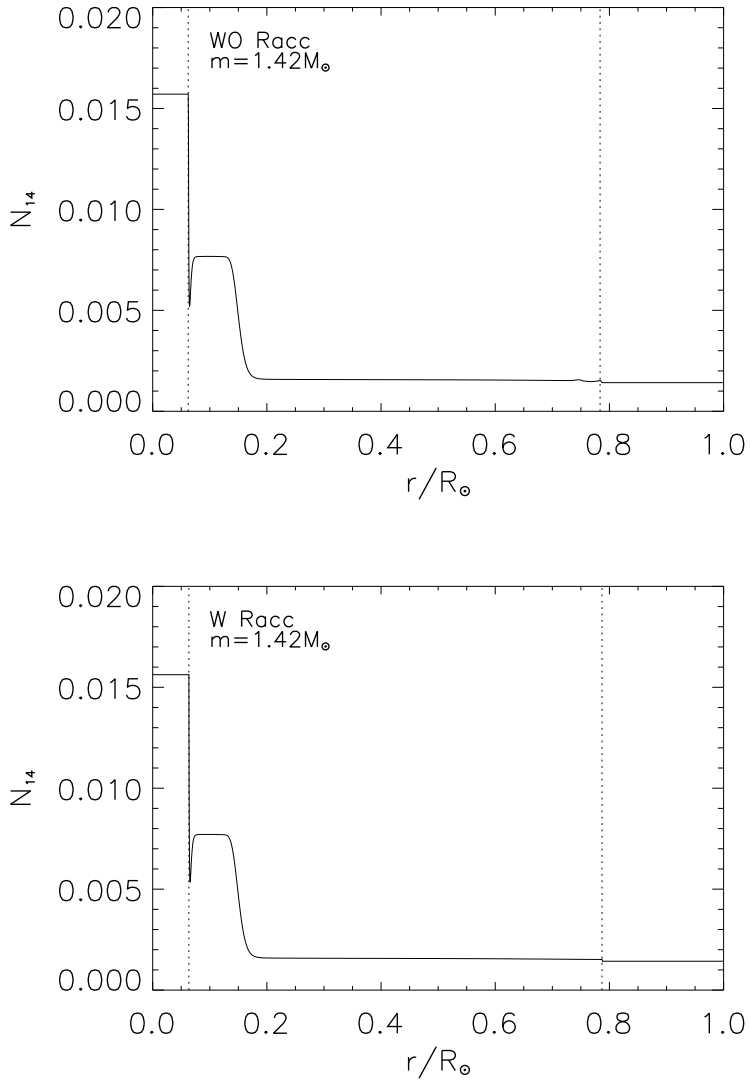

Figure 3.8: N profiles for models with M=1.42 $M_{\odot}$, calculated with (*upper panel*) and without (*lower panel*) including radiative accelerations. Dashed lines indicate the base of the surface convection zone and the boundary of the convective core.

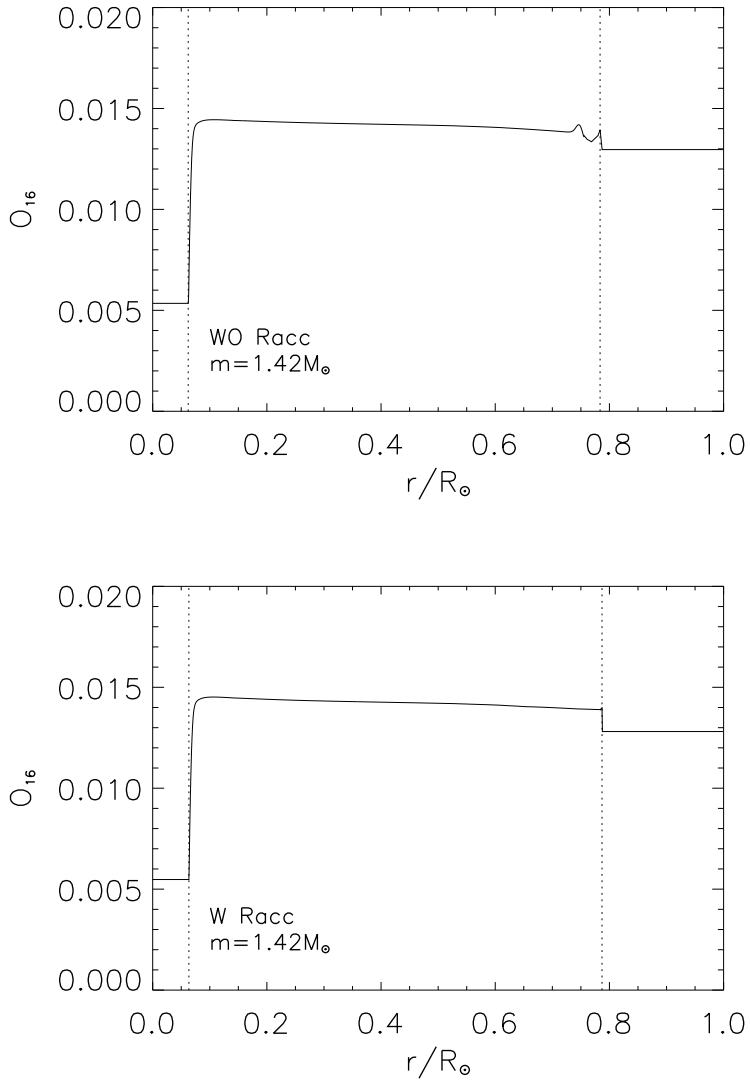

Figure 3.9: O profiles for models with M=1.42 $M_\odot$, calculated with (*upper panel*) and without (*lower panel*) including radiative accelerations. Dashed lines indicate the base of the surface convection zone and the boundary of the convective core.

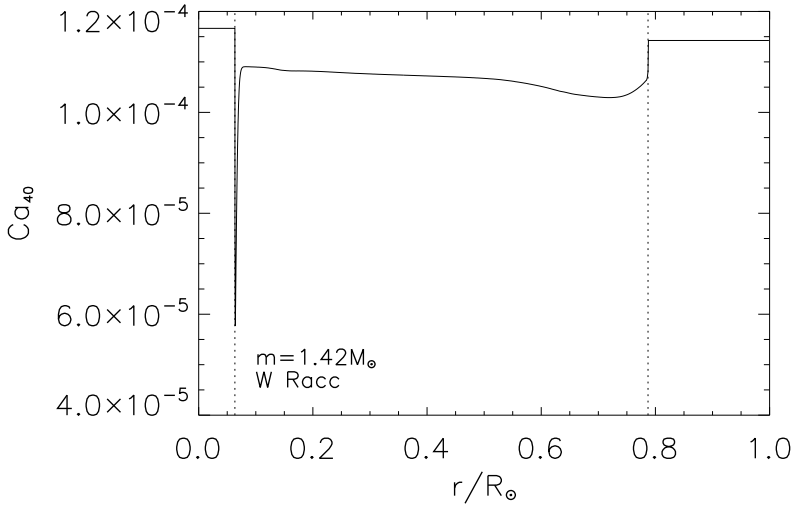

Figure 3.10: Ca profile for M=1.42 $M_\odot$ model calculated including radiative accelerations. Dashed lines indicate the base of the surface convection zone and the boundary of the convective core.

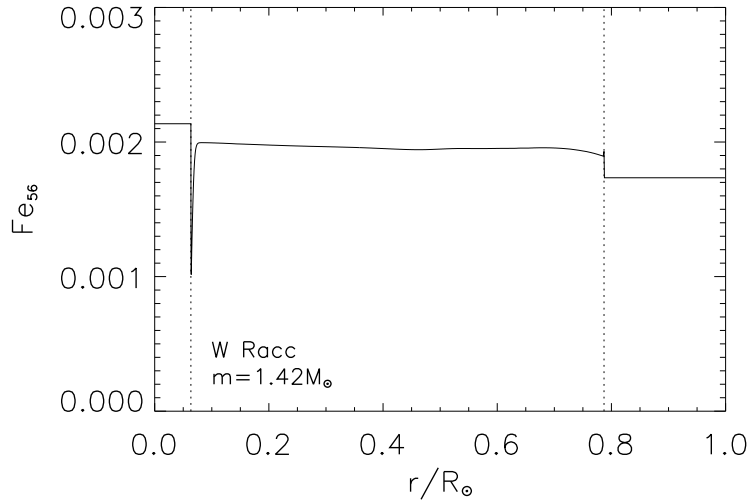

Figure 3.11: Fe profile for M=1.42 $M_\odot$ model calculated including radiative accelerations. Dashed lines indicate the base of the surfacz convection zone and the boundary of the convective core.

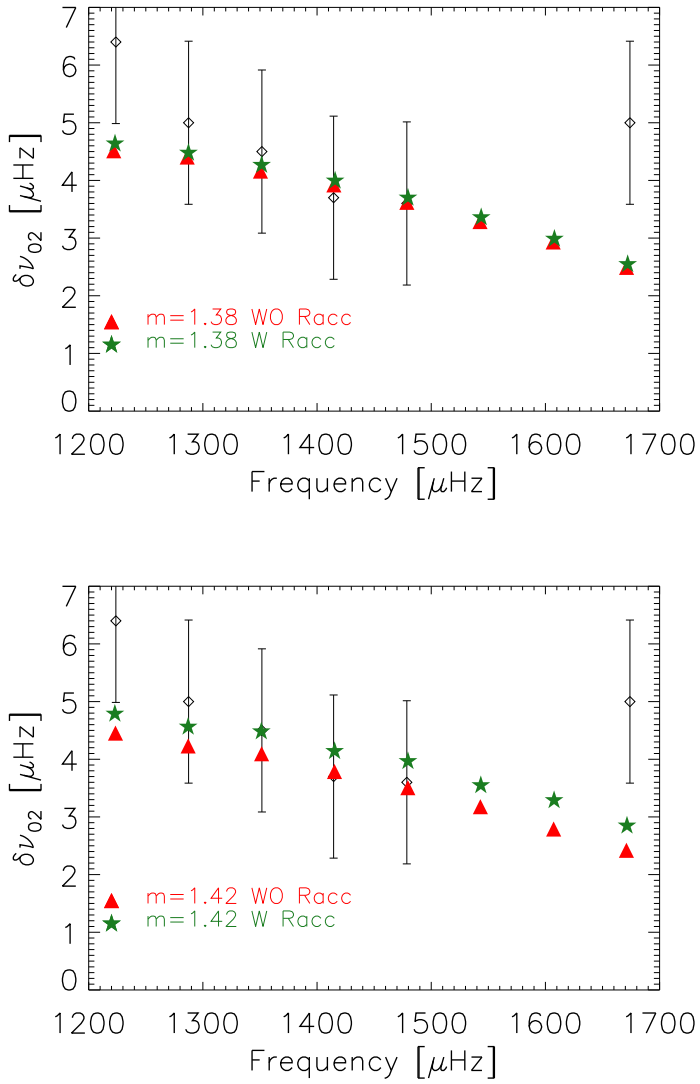

Figure 3.12: Small separations $\delta\nu_{02}$ for M=1.38 $M_\odot$ (*upper panel*) M=1.42 $M_\odot$ (*lower panel*) models. Red triangles and green stars indicate models obtained using the version (without overshooting) of TGEC without radiative accelerations and the new version including radiatiave accelerations, respectively. Observations are represented by empty diamonds.

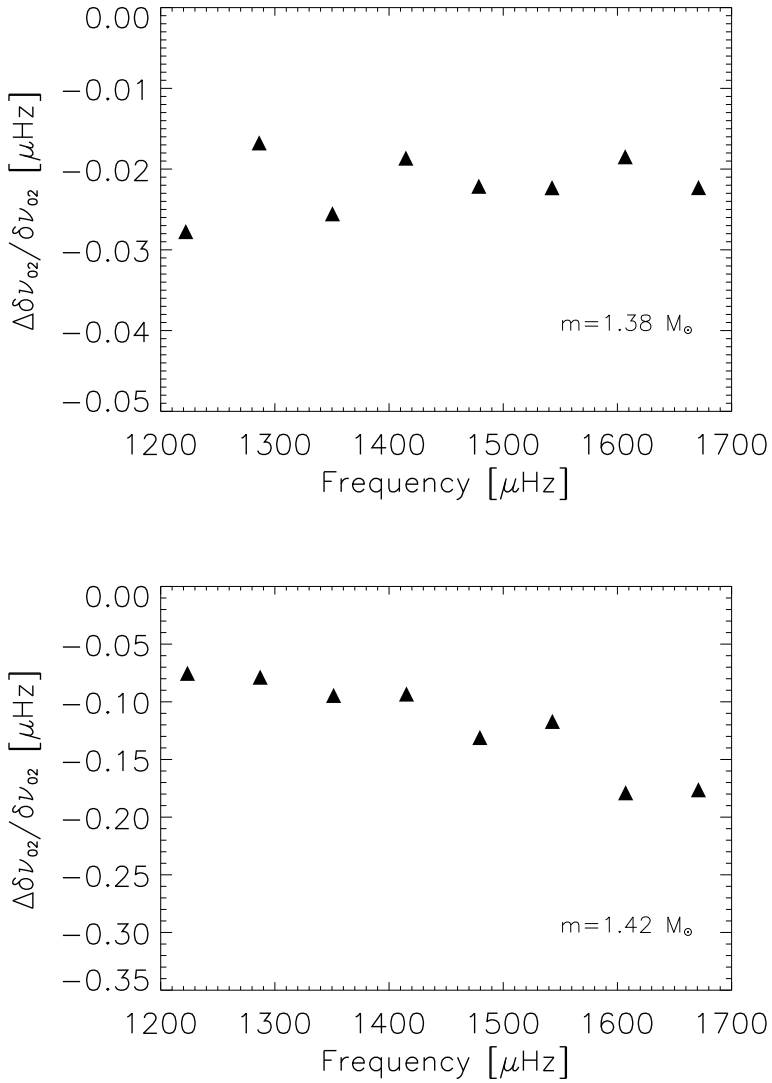

Figure 3.13: $\Delta\delta\nu_{02}/\delta\nu_{02}$ ratio for M=1.38 $M_\odot$ (*upper panel*) and M=1.42 $M_\odot$ (*lower panel*) models, obtained by including or not radiative accelerations.

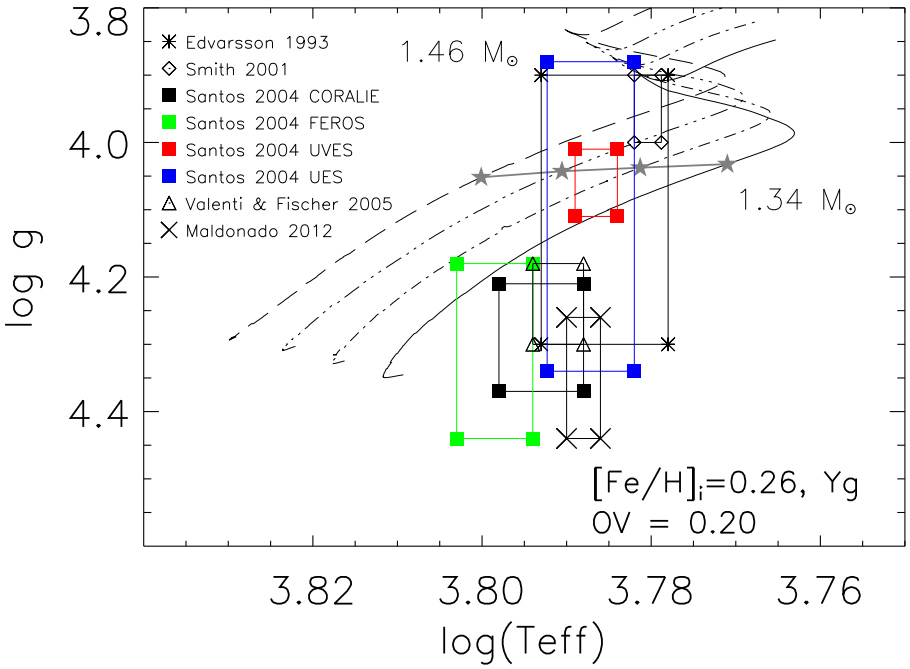

Figure 3.14: Evolutionary tracks in the log g versus log $T_{\rm eff}$ plane calculated with $[Fe/H]_i$ =0.26, Y_i=Y_G, and considering overshooting in the stellar core, with α_{ov}=0.20.The symbols indicating the error boxes are the same as figure 3.4. The star symbols indicate the location of the model which, on each evolutionary track, has the required $<\Delta\nu>$. They are linked by the straight thick line representing the iso-$<\Delta\nu>$ line, with $<\Delta\nu>$=64.3 μHz.

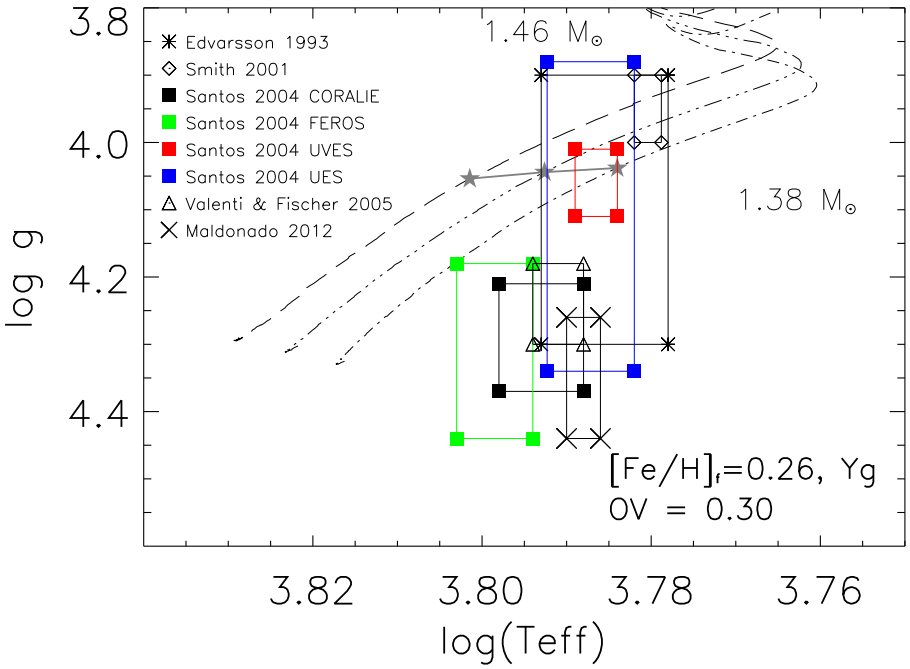

Figure 3.15: Evolutionary tracks in the log g versus log $T_{\rm eff}$ plane calculated with $[Fe/H]_i$ =0.26, Y_i=Y_G, and considering overshooting in the stellar core, with α_{ov}=0.30.The symbols indicating the error boxes are the same as figure 3.4. The star symbols indicate the location of the model which, on each evolutionary track, has the required $<\Delta\nu>$. They are linked by the straight thick line representing the iso-$<\Delta\nu>$ line, with $<\Delta\nu>$=64.3 μHz.

Table 3.7: Examples of models obtained including overshooting in the calculations. The columns are the same as in table 3.5.

$[Fe/H]_i$	Y_i	$M/M_\odot$	Age [Gyr]	$[Fe/H]_s$	Y_s	$\log g$ [K]	$\log T_{\rm eff}$	$\log (L/L_\odot)$	$R/R_\odot$	M/R^3 [solar units]	$<\Delta\nu>$ [μHz]	$<\delta\nu_{02}>$ [μHz]	χ^2
$\alpha_{ov} = 0.200$													
0.26	0.297	1.38	3.184	0.19	0.249	4.037	3.781	0.620	1.871	0.21	64.32	3.61	4.86
0.26	0.297	1.42	2.673	0.15	0.217	4.042	3.790	0.664	1.886	0.21	64.28	3.97	4.30
0.26	0.297	1.46	2.194	0.08	0.171	4.051	3.800	0.705	1.893	0.21	64.33	4.78	4.47
$\alpha_{ov} = 0.300$													
0.26	0.297	1.38	3.348	0.17	0.229	4.038	3.784	0.630	1.870	0.21	64.36	3.67	5.14
0.26	0.297	1.42	2.823	0.12	0.201	4.044	3.792	0.671	1.884	0.21	64.33	4.16	5.17
0.26	0.297	1.46	2.314	0.04	0.145	4.054	3.801	0.709	1.889	0.21	64.35	4.86	5.54

From this table we can see that when overshooting is included, and also when the value of α_{ov} increases, the age of the model increases, but the stars have not left the MS phase. In this case, stellar evolution takes a longer timescale. Luminosities are also higher for models including overshooting. The radii of the models are slightly smaller than in models without overshooting. We also notice that the final metallicity value is not the same for all the models. For this reason. we have performed new iterations until we obtained models with a final surface metallicity of [Fe/H]=0.19. In table 3.8 we present these new models. For M=1.46 $M_{\odot}$ it was not possible to obtain models with the good metallicity, given that the initial metallicity value that should be used as an input was too high to be realistic.

Table 3.8: Examples of models obtained performing new iterations to obtain the final surface metallicity in agreement with spectroscopic observations. The columns are the same as in table 3.5.

$[Fe/H]_i$	Y_i	$M/M_\odot$	Age [Gyr]	$[Fe/H]_s$	Y_s	$\log g$ [K]	$\log T_{\rm eff}$	$\log (L/L_\odot)$	$R/R_\odot$	M/R^3 [solar units]	$<\Delta\nu>$ [μHz]	$<\delta\nu_{02}>$ [μHz]	χ^2
No OV													
0.26	0.297	1.38	2.989	0.20	0.252	4.036	3.778	0.608	1.873	0.21	64.35	4.12	2.40
0.26	0.297	1.42	2.553	0.19	0.245	4.041	3.784	0.641	1.891	0.21	64.18	4.36	2.90
0.30	0.302	1.46	2.134	0.20	0.231	4.048	3.792	0.677	1.902	0.21	64.26	4.54	3.14
$\alpha_{ov} = 0.20$													
0.26	0.297	1.38	3.184	0.19	0.249	4.037	3.781	0.620	1.871	0.21	64.32	3.61	4.86
0.30	0.302	1.42	2.658	0.19	0.226	4.043	3.789	0.659	1.885	0.21	64.34	4.20	4.51
$\alpha_{ov} = 0.30$													
0.28	0.299	1.38	3.348	0.19	0.235	4.037	3.782	0.626	1.872	0.21	64.29	3.60	5.28
0.33	0.307	1.42	2.837	0.21	0.222	4.043	3.789	0.658	1.884	0.21	64.34	4.15	5.60

Regarding the final models with overshooting in table 3.8, we can notice that the differences on a specific stellar parameter are very small. Luminosity, temperature and radius stay at the same value for a given mass. Only differences in age are slightly larger, meaning that with a more efficient overshooting, the evolution of the star takes longer. Also we notice that only two models, of M=1.38 $M_\odot$ and 1.42 $M_\odot$ lie inside the error boxes presented in figure 3.14 and 3.15.

3.8 Analysis and Discussion

We have computed theoretical frequencies for models along several evolutionary tracks. We have considered models with and without overshooting. We also performed calculations including radiative acceleration on heavy elements for the treatment of atomic diffusion. Among all these models, we kept only the ones that better fit observational and asteroseismic constraints. To use all the potential that asteroseismology provides through the comparison of model and observational frequencies it is now necessary to go further in the frequency comparisons. To do this, we obtain the échelle diagrams for models that represent the best the observational constraints in log g, log $T_{\rm eff}$, and [Fe/H] (figures 3.16 to 3.19).

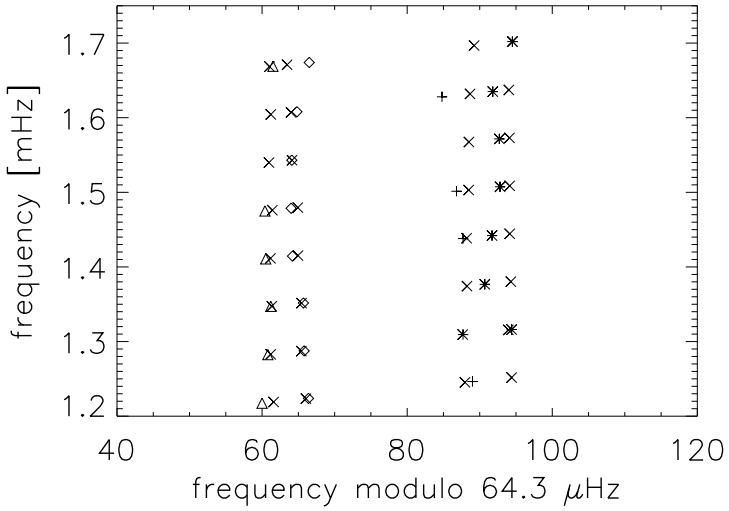

Figure 3.16: Echelle diagram for M=1.42 $M_\odot$, for a model computed without considering overshooting in the core. Observational frequencies are represented by diamonds ($\ell = 0$), asterisk ($\ell = 1$), triangles ($\ell = 2$), and plus signs ($\ell = 3$). Crosses represent theoretical mode frequencies.

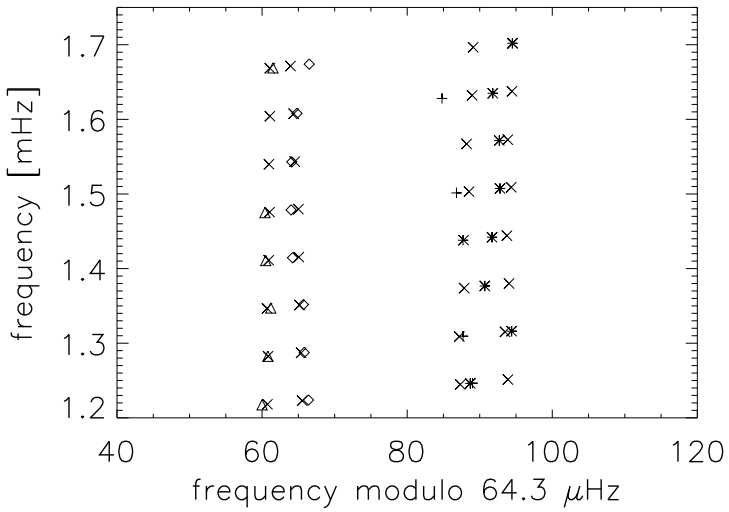

Figure 3.17: Echelle diagram for M=1.42 $M_\odot$, for a model computed without overshooting in the core, and including radiative accelerations on heavy elements. Symbols are the same as figure 3.16

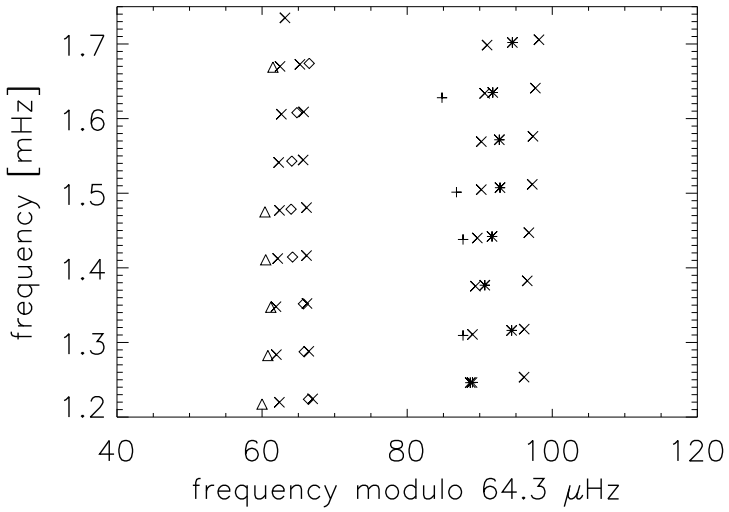

Figure 3.18: Echelle diagram for M=1.42 $M_\odot$, for a model computed with overshooting, with α_{ov}=0.20, and $[Fe/H]_i$=0.30. Symbols are the same as figure 3.16

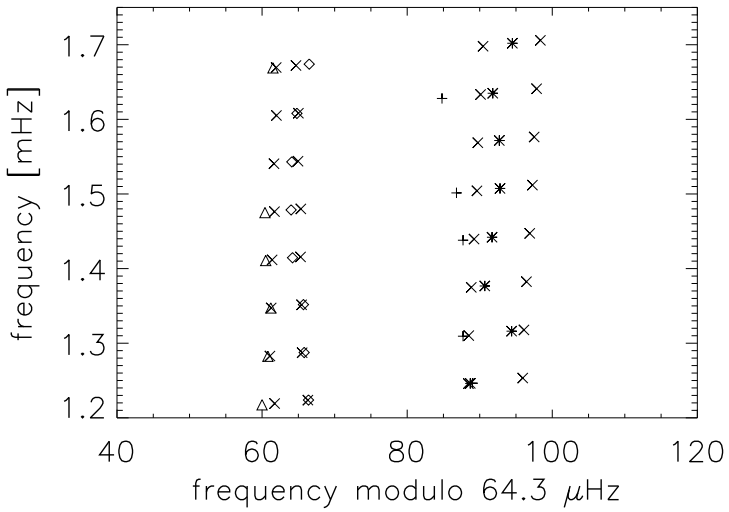

Figure 3.19: Echelle diagram for M=1.42 $M_\odot$, for a model computed with overshooting, with α_{ov}=0.30, and $[Fe/H]_i$=0.33. Symbols are the same as figure 3.16

From these figures we see a very good fit for the ℓ=0 and ℓ=2 ridges. But the fit is not as good for the ℓ=1 and 3 ridges. For ℓ=3 the mode amplitudes are very low, making very difficult their identification given the daily aliases that affect ground-based observations. For ℓ=1, we have found that this star is seen in a equator-on angle, which has strong consequences on the visibility of the modes for this particular angular degree. Given the projected rotation velocity $v \sin i$, the rotation period P_{rot}, and the linear radius R_{star}, the inclination angle i of the rotation axis on the line of sight can be determined. In the case of 94 Cet, P_{rot}=12.2 days (Mayor et al. (2004), from R_{HK} activity indicator), $R/R_\odot$=1.898±0.070 from interferometric observations (van Belle & von Braun, 2009). We obtain $\sin i \approx 1.02$ which finally gives and inclination angle of $i = 90°$. When a star is seen equator on, Gizon & Solanki (2003) showed that for ℓ=1 modes, the central $m = 0$ component should not be seen. Only are visible the $m = \pm 1$ components of ℓ=1 modes. With a rotation period of P_{rot}=12.2 days, the shift induced by rotational splitting is $\sim$ 0.95 μHz. Thus, in 94 Cet case, we expect to see the $m = \pm 1$ components of ℓ=1 modes separated by $\sim$ 1.9 μHz. For ℓ=2 modes, Gizon & Solanki (2003) predict the visibility of three components: $m = 0$ and $m = \pm 2$. The frequency shift between visible components should be also $\sim$ 1.9 μHz. However, since the predicted amplitudes for $m = 0$ component are lower than $m = \pm 2$ components, there may be cases where only $m = \pm 2$ component are identified. The case for ℓ=3 is not

discussed in Gizon & Solanki (2003). We have to take this into account for our analysis since, when comparing observed and model frequencies, we performed these comparisons with the $m = 0$ components of the modes. If we come back to the échelle diagrams in figures 3.16 to 3.19, we can think that the poorer fits seen in ℓ=1 and ℓ=3 ridges, could be due to this visibility problem caused by the line of sight along which we observe 94 Cet.

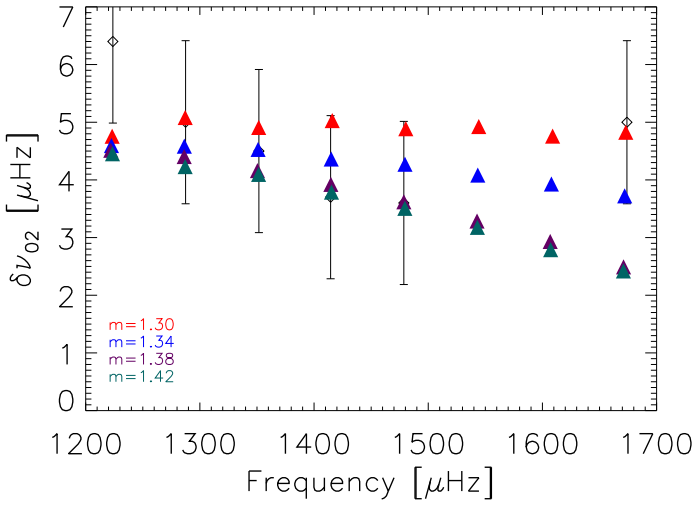

Figure 3.20: Small separations $\delta\nu_{02}$ vs frequency for models computed without overshooting. Observations are represented as empty diamonds. Triangles of different colors indicate models with 1.30 $M_\odot$ (*red*), 1.34 $M_\odot$ (*blue*), 1.38 $M_\odot$ (*purple*) and 1.42 $M_\odot$ (*green*). Notice the different slope depending on the mass of the model.

We also made a comparison between observed and model frequencies using other seismic tests. In figure 3.20 we present the small separations $\delta\nu_{02}$, for the models without overshooting together with the observed values. Small separations obtained from observational data are represented by empty triangles, with their corresponding error bar ($\sigma_{obs} \sim 0.1$ μHz). Models are represented by filled triangles of different colors depending on their mass. Figures 3.22 and 3.23 show the small separation comparison for the two cases involving overshooting, and Figure 3.21 for models computed including radiative accelerations.

From all these figures, we see how the slope of $\delta\nu_{02}$ changes with the mass of the model. Depending on their mass, the stars are on a different stage of their evolution. Thus this variation of the slope reflects the age of a given model. Moreover, we also see a variation of the average value of the small separations. We see how when going from the 1.20 $M_\odot$ model to the more massive ones, the small separations

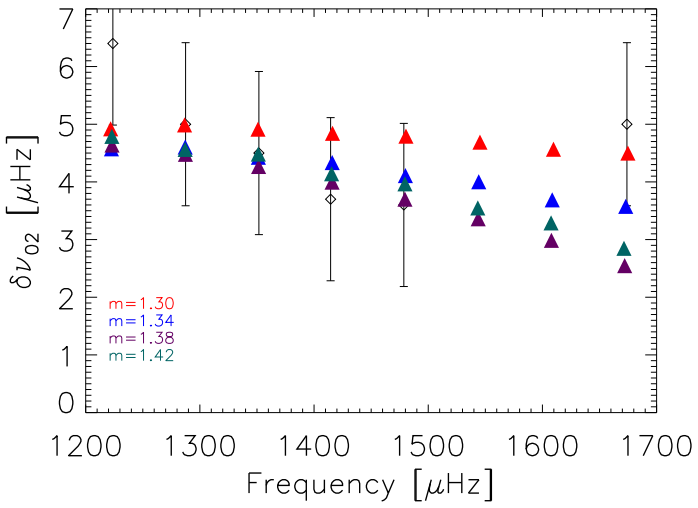

Figure 3.21: Small separations $\delta\nu_{02}$ vs frequency for models computed including radiative accelerations. Observations are indicated as empty diamonds and theoretical results as filled triangles. Colors indicate the same masses as in figure 3.20. Notice the different slope depending on the mass of the model.

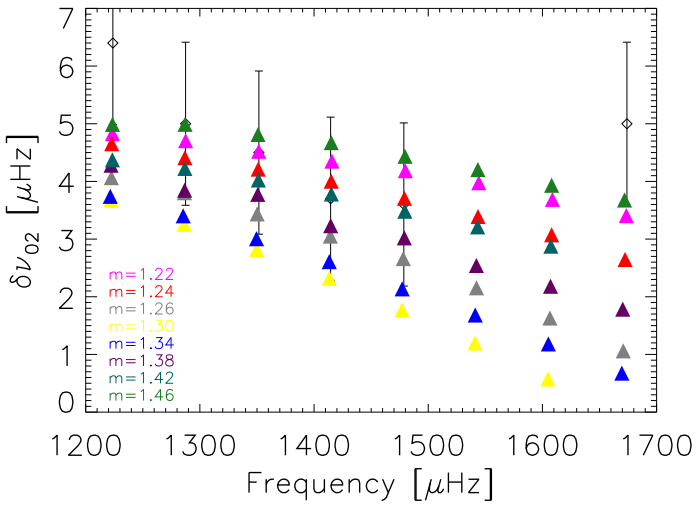

Figure 3.22: Small separations $\delta\nu_{02}$ vs frequency for models computed including overshooting, with α_{ov}=0.20. Models are displayed as filled triangles and observations as empty diamonds. Each color representing a different mass value as indicated on the figure. As in previous figure, notice the slope depending on the mass of the model.

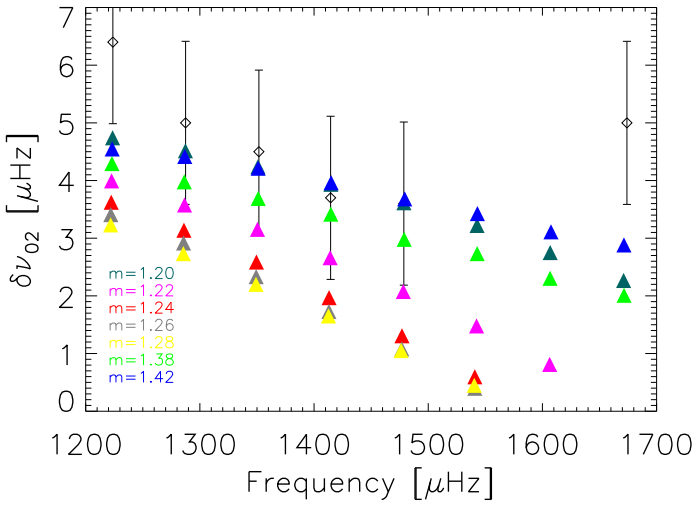

Figure 3.23: Small separations $\delta\nu_{02}$ vs frequency for models computed including overshooting, with α_{ov}=0.30. Models are displayed as filled triangles and observations as empty diamonds. Each color representing a different mass value as indicated on the figure.

globally decrease and start increasing again towards more massive models (like 1.42 for example). This change in *direction* is related to the evolutionary phase of the star. Whereas 1.20 mass models are subgiants, more massive models are younger, i.e., in an early stage of their evolution. For models still on the MS, the decreasing trend is reverted. In main sequence stars, we expect the small separations to increase for increasing mass. This has been for example the case of HD 52265 (see table 2.6 in chapter 2).

Even if the 1.2 $M_\odot$ model seems to well fit the observed $\delta\nu_{02}$ values, it is possible to see from figure 3.4 that these less massive models fall far away from the observational error boxes from spectroscopic studies. Then, they cannot correctly represent 94 Cet. At this point, with all the analysis done so far, we can conclude that the models which better represent 94 Cet are the models with a mass $\sim$ 1.42 $M_\odot$.

We present the 1.42 $M_\odot$ models in the log g - log Teff diagram in Figure 3.24. Here we only show two models, the first one without overshooting, the second one with an overshooting parameter α=0.20. In this diagram, the models obtained with or without radiative accelerations cannot be distinguished. In the same way, the models with an overshooting parameter of 0.30 are too close to those obtained with 0.20 to be visible (see Table 3.8)

As already mentioned in previous sections, the radius for this star is know with a high precision from interferometric observations. Using data from Center of High Angular Resolution Astronomy (CHARA) Array, van Belle & von Braun (2009) obtained $R/R_\odot$=1.898±0.070 for 94 Cet.

With all this information, we deduce the following stellar parameters for 94 Cet:

- $M/M_\odot = 1.41 \pm 0.02$
- $R/R_\odot = 1.88 \pm 0.01$
- log g = 4.04 ± 0.005
- $T_{\rm eff} = 6025 \pm 50$ K
- $L/L_\odot = 0.62 \pm 0.02$

3.9 Conclusion

We have performed a complete asteroseismic study, including observations and modeling, of the star 94 Cet. Observation for this star were done with the HARPS spectrograph mounted on the ESO 3.6 m telescope in La Silla observatory, Chile. Twenty eight p-mode frequencies were identified, with a sigma of $\sim$ 1 μHz.

Several evolutionary tracks were calculated using the TGEC and theoretical mode frequencies were obtained using the PULSE Code. We obtained tracks for

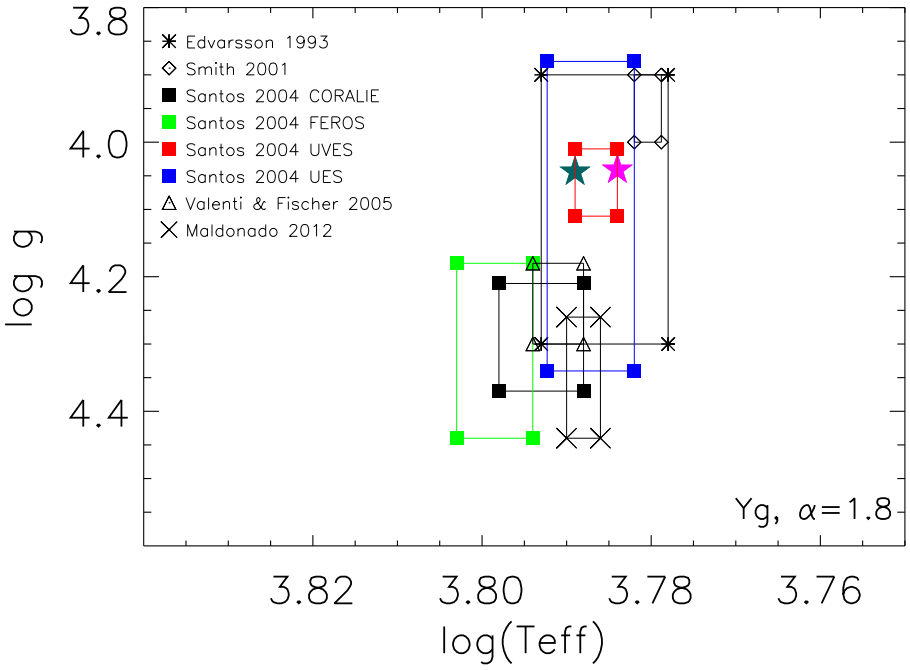

Figure 3.24: Log g versus log $T_{\rm eff}$ plane where m=1.42 $M_{\odot}$ models are displayed. The symbols indicating the error boxes are the same as figure 3.4. The star symbols indicate the location of the model with no overshooting or radiative accelerations included (*pink star*), and the model with α_{ov}=0.20 (*magenta star*).

different masses, ranging from 1.20 to 1.46 $M_{\odot}$, and for a metallicity $[Fe/H]_s$=0.19 and an initial helium abundance Y_G. Models with and without overshooting were obtained. Also, models including the radiative accelerations on heavy elements in the diffusion processes were computed, thanks to a new and improved version of the TGEC.

Results showed that 94 Cet should be a moderate mass star with a mass M= 1.41±0.02, a radius of 1.88 ± 0.01 and a log g= 4.04±0.005. It is remarkable to see how asteroseismology can precisely constraint log g value. The radius we obtained is in good agreement with the result obtained from interferometric observations, of 1.898±0.070.

Thanks to the mass of this star we were able to test internal physics by comparing the results obtained with the two versions of the TGEC, which includes or not radiative accelerations. We see, as expected, that the difference in internal structure, as seen on the different seismic tests, is more important for larger masses.

When comparing with the "twin" star of 94 Cet, β Virginis, no definitive conclusion can be made due to the poor accuracy of the asteroseismic observational results for this star. Nevertheless, with the data available now from seismic studies, we can confirm the overmetallicity of the stars hosting extra-solar planets, but we can not really distinguish between different mixing process inside the stars. To achieve that goal, higher accuracy on the frequencies that the one achieved nowadays is needed, or new techniques have to be developed.

Chapter 4

51 Pegasi

The discovery of the first planet orbiting another star than the Sun, by Mayor & Queloz (1995), namely 51 Peg began a new era of knowledge, not only for the existence of other solar systems, but also for the processes involved in their formation. Since then, great efforts have been made to detect new extra-solar worlds and infer their properties. For this purpose, a needed step is the precise characterization of their parent stars. Here we present our aim to reach a better and more accurate understanding of the properties of 51 Peg by asteroseismology that, as we have already seen, can give results with a precision not possible with other techniques. We present the observations that we have made at the Haute Provence Observatory (France), the difficulties in the identification of the oscillation modes and the results we obtained. Also a preliminary stellar modeling for this star was performed and is presented at the end of this chapter.

4.1 The 51 Pegasi System

4.1.1 The central star

The star 51 Pegasi (HD 217014, HR 8729, HIP 113357) is a G2IV main sequence star located at 13.7 pc (RA 22 57 27, DEC +20 46 07). Its characteristics place it as a star very similar to the Sun, except for its overmetallicity, a very common feature presented in planet-host stars. It has a visual magnitude of V=5.49 (*Simbad Astronomical Database*), and a parallax of $\pi = 64.07 \pm 0.38$ mas (*Hipparcos catalog*, van Leeuwen (2007)). This gives a luminosity of $log(L/L_{\odot}) = 0.13 \pm 0.03$.

4.1.2 Previous Spectroscopic Studies

As already explained in previous chapters, to correctly model a star we need to know in advance basic parameters like its effective temperature and metallicity. In particular the ([Fe/H], T_{eff}, log g) triplet deduced from spectroscopic studies is of main importance. Several previous studies have been done about 51 Peg. Most of them focus on its planet-host star status, but it has also been studied in the framework of general studies of the Galactic disk (Bensby & Feltzing, 2003), as well as nearby F-K dwarfs and subgiants (Takeda et al., 2005). A summary of the main spectroscopic observations that include 51 Peg is given in table 4.1.

Table 4.1: Summary of previous spectroscopic studies of 51 Peg

[Fe/H]	T_{eff}	log g	Reference
0.06 ± 0.10	5755 ± 100	4.18 ± 0.20	Edvardsson et al. (1993)
0.20 ± 0.07	5793 ± 70	4.33 ± 0.10	Fuhrmann et al. (1997)
0.23 ± 0.05	5750 ± 50	4.25 ± 0.05	Heiter & Luck (2003)
0.20 ± 0.10	5789 ± 100	4.34 ± 0.10	Bensby & Feltzing (2003)
0.20 ± 0.05	5804 ± 36	4.42 ± 0.07	Santos et al. (2004b)
0.20 ± 0.02	5779 ± 15	4.30 ± 0.03	Takeda et al. (2005)
0.20 ± 0.03	5787 ± 44	4.45 ± 0.06	Valenti & Fischer (2005)
0.20 ± 0.10	5654 ± 70	4.27 ± 0.10	Chen & Zhao (2006)
0.215 ± 0.023	5832 ± 50	4.38 ± 0.07	Ramirez et al. (2009)
0.11 ± 0.03	5710 ± 20	4.15 ± 0.16	Maldonado et al. (2012)

It is possible to notice from table 4.1 that almost all spectroscopic studies agree on a [Fe/H] value of ~ 0.20, with the exception of the studies of Edvardsson et al. (1993) and Maldonado et al. (2012). For the preliminary modeling of this star we will calculate models with $[Fe/H]_s \simeq 0.20$

4.1.3 Stellar Radius

The radius of 51 Pegasi has been measured by interferometry using two different interferometers (van Belle & von Braun, 2009). The first one is the Palomar Testbed Interferometer (PTI), an 85 a 110 m interferometer, working in H 1.6 μm and K 2.2 μm bands, located at Palomar Observatory (Colavita, 1999). The second one is the CHARA Array of the Georgia State University, an optical/near-infrared interferometer similar to PTI, but with longer baselines (up to 330 m), allowing for resolution of smaller objects (Baines et al., 2008).

The results obtained by van Belle & von Braun (2009) for 4 exoplanet-host stars, including 51 Peg, show that the angular diameters obtained with CHARA are

systematically larger than those obtained with PTI, by about 5 to 10 %. For 51 Peg, the PTI value is 1.141±0.133 whereas the CHARA value is 1.23±0.02. The reasons for the differences obtained with the two instruments is unclear.

4.1.4 The planet

The 51 Pegasi planet companion was detected for the first time by Mayor & Queloz (1995), and later verified by Marcy et al. (1997). With a mass of 0.468 M_J, this Jupiter-like planet is located at 0.05 AU from its parent star, orbiting with a period of 4.23 days. Naef et al. (2004) updated the orbital solution for 51 Peg, as presented in table 4.2.

Table 4.2: Orbital Solution for 51 Peg (Naef et al., 2004)

51 Peg b	
Period	4.23077 ± 0.00004
Msin i [M_J]	0.468 ± 0.007
a [AU]	0.052
Eccentricity	0 (fixed)

4.2 Observations

Two observing runs were carried out to obtain asteroseismic data for 51 Peg. First this star was observed during nine consecutive nights in August 2007. Three years later a new campaign was done, performing observations during 12 consecutive nights in August 2010. Both observing runs were performed using the spectrograph SOPHIE mounted in the 1.93 m telescope at the Haut Provence Observatory (OHP), France.

4.2.1 SOPHIE

SOPHIE is an échelle spectrograph installed in a temperature-controlled room at the 1.93m telescope at the Haut Provence Observatory, France. It is in service for the scientific community since October 2006. Initially designed for extra-solar planet searches, thanks to its high performance it may also be used for asteroseismic observations.

SOPHIE is associated with a high-efficiency coupling fiber feeding system, allowing simultaneously observations and wavelength calibration. The CCD detector is

an EEV 44-82 with 4102x2048 pixels of 15 microns, kept at a constant temperature of -100°C in a dewar with an autonomy of 48 hours. The readout time is $\sim$ 30 sec in fast mode with a readout noise $\sim$ 8 e^-, and of $\sim$ 3 min in slow mode with a readout noise $\sim$ 4 e^-. Each of the two optical fibers sets feeding SOPHIE consists on two circular entrance apertures of 3 arcsec diameter, separated by 1.86 arcmin in the focal plane. The optical fibers are of 100 micron diameter. Fiber A is used for the target and Fiber B for calibrations (sky spectrum or Thor-Ar lamp exposures).

Two operation modes are available:

- High-resolution Mode (HR). It can reach resolution of R=70000.
- High-efficiency (HE). Used to observe fainter stars. It can reach a resolution of R=40000.

The spectra covers a wavelength range of 3872 to 6943 Å. The calibration is done using a Thorium-Argon calibration lamp. SOPHIE is controlled by computer and a standard data reduction pipeline is available on site. This allows automatic process of the data upon CCD readout, giving as a results RV values such precises as 2-3 m/sec (depending on S/N value). The main technical characteristics of SOPHIE are presented in table 4.3.

The instrument stability is very important for the observations. In the SOPHIE case, the spectrograph is isolated in a thermally controlled chamber where temperature and humidity are under control. The chamber is in an air-conditioned room and it has a special insulated wall. The pressure is also controlled and kept constant, and the temperature is stable at $\pm$ 0.01°C.

Table 4.3: Main technical characteristics of SOPHIE spectrograph

OPTICAL DESIGN	cross-dispersed échelle spectrograph
RESOLUTION	40000 (HE mode) or 75000 (HR mode)
NUMBER OF ORDERS	39
WAVELENGTH COVERAGE	387 nm - 694 nm
SKY COVERAGE	3 arcsec
DETECTOR	1 CCD EEV 44-82 4102x2048 pixels

4.2.2 Observing Runs

August 2007

51 Pegasi was observed from August 6 to 15, 2007 with the spectrograph SOPHIE at the Haute Provence Observatory. For this observations High Resolution (HR)

mode was used. Science exposures for this star were simultaneously taken with Th-Ar lamp calibration exposures. The Journal for these observations is presented in table 4.4.

A total of 1014 Radial Velocity measurements were obtained, with a signal-to-noise ratio above 50. During the first and the two last nights, it was not possible to obtain as many data as expected due to bad weather. Also, technical problems due to temperature control system happened between August 11 to 13, having as a consequence a large dispersion on the data as well as higher values for the drift.

In figures 4.1 and 4.2 we present the radial velocity measurements for the 2007 campaign. Clearly in figure 4.1 it is possible to see the effect of the planet on the observations, with a period of $\sim$ 102 hours. In figure 4.2 the effect due to the planet orbit has been removed.

We also obtained the power spectrum from Fourier transform of radial velocity measurements, which is presented in figure 4.3. We can notice that the data are very noisy. Nevertheless, solar-like oscillations are clearly present.

Table 4.4: Journal of the observations of 51 Peg obtained in August 2007 with the spectrograph SOPHIE.

Date	Number of exposures	Hours
06	70	3.00
08	151	6.43
09	158	6.72
10	160	6.80
11	160	6.81
12	170	7.23
13	159	6.79
14	160	6.80

August 2010

As the data obtained in 2007 were not good enough to allow a reliable identification of frequency modes, a second observational campaign was carried out for 51 Peg from August 2 to 13, 2010. A total of 1631 radial velocity measurements were obtained. During the night of August 4 no observations were done due to technical problems. Observations were performed using the HR mode, taking at the same time the exposure for the star as well as the Th-Ar lamp exposure. Exposure time was set at 120 sec, plus 53 sec of readout time.

The journal of 2010 observing run is presented in table 4.5. Some nights present less measurements mainly due to bad weather conditions. The power spectrum

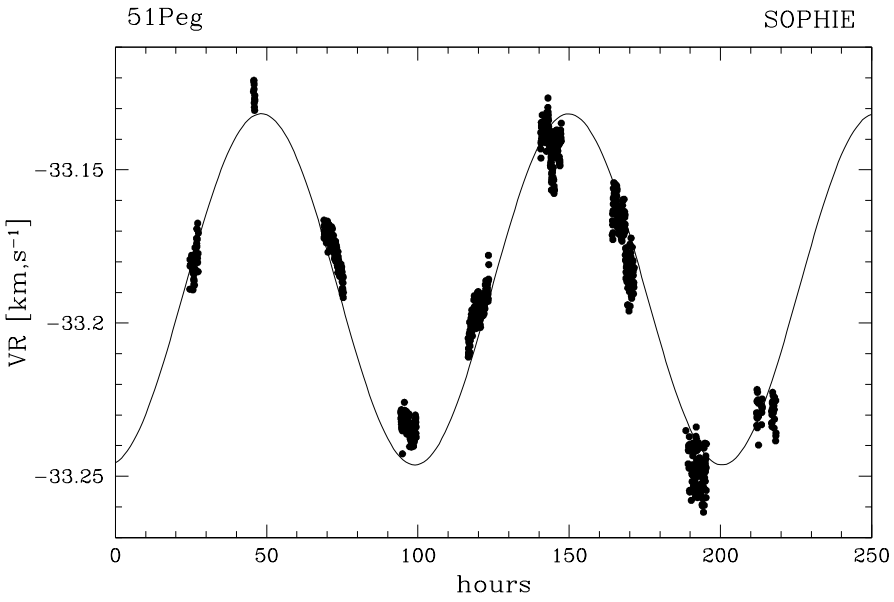

Figure 4.1: Radial velocity measurements for 51 Peg, for the observing campaign done in 2007. The dashed line corresponds to the planet orbit fit.

obtained from radial velocity measurement for 2010 observations is presented in figure 4.5, and the radial velocity measurements in figure 4.4. Even though this power spectrum is also noisy, we were able to identify several mode oscillation frequencies. In particular this was possible by correcting the data for instrumental effects (Isabelle Boisse, private communication). The list of the identified modes as well as the method used for their identification will be presented in next section.

4.3 Mode Identification

The power spectra obtained for the two runs in 2007 and 2010 differ in the mode amplitudes, but the data are not precise enough to take it as real variations. The

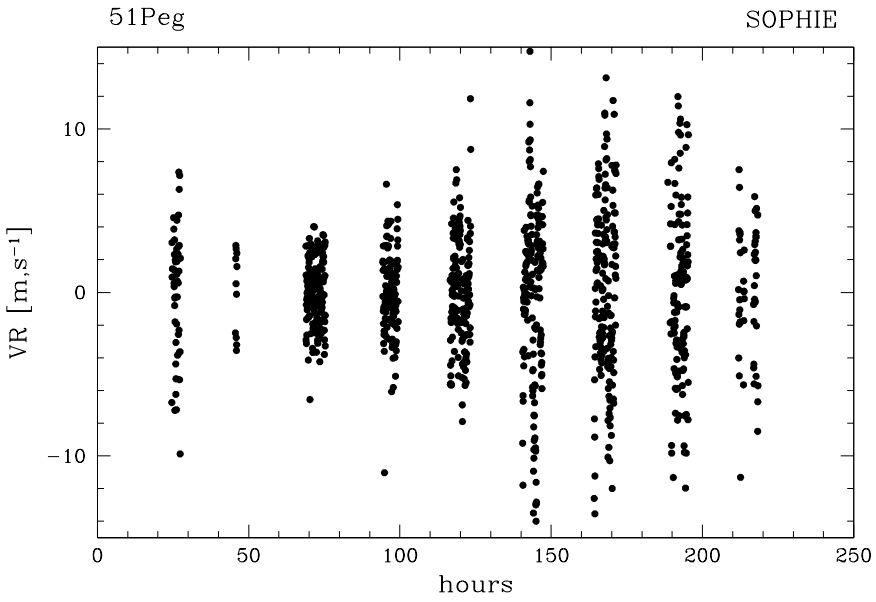

Figure 4.2: Radial velocity measurements for 51 Peg, for the observing campaign done in 2007. The effect due to the planet orbit has been removed.

power spectrum of 2010 observations presented in figure 4.5 suggests a power excess typical from solar-like oscillation at a maximum frequency ~ 2.5 μHz . This does not appear in the same way in the 2007 data. However, when trying to identify modes with the 2010 data, we find that the identified modes are also present in the 2007 data. Mode identification is not an easy task for ground-based observations. Daily aliases coming for the day-night gap in observations makes a forest of peaks were real mode oscillations are difficult to identify. A careful analysis of the power spectrum has to be done and checked several times to finally obtain a reliable list of frequency oscillations.

The method used at this moment was to pass the observing window in front of a zoomed version of the power spectrum in the region of interest. Thus, it is possible to visually identify the mode frequency and its aliases. This method is

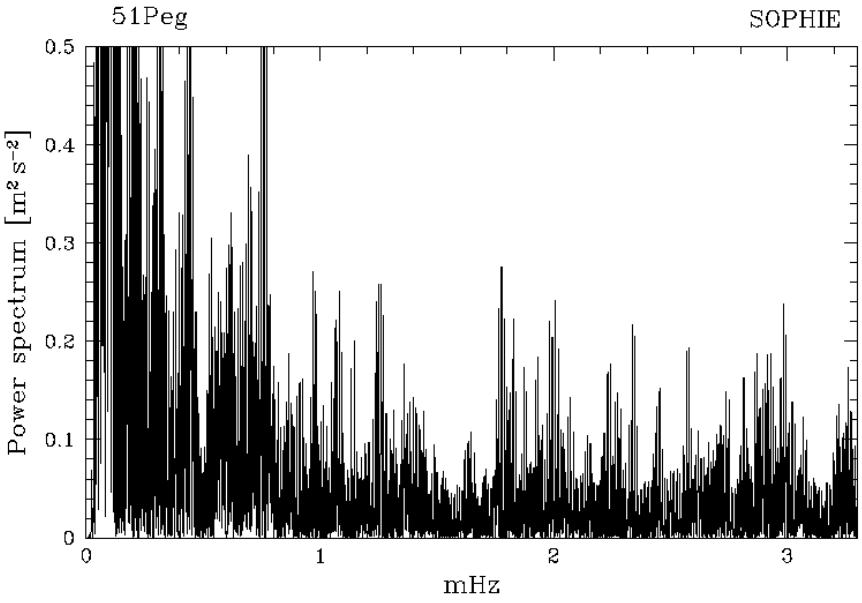

Figure 4.3: Power spectrum obtained from radial velocity measurement of 51 Peg, from observations taken in 2007.

Table 4.5: Journal of the observations of 51 Peg obtained in August 2010 with the spectrograph SOPHIE.

Date	Number of exposures	Hours
02	150	6.40
03	140	6.00
05	150	6.36
06	116	4.94
07	157	6.70
08	168	7.14
09	127	5.39
10	171	7.30
11	153	6.50
12	148	6.31
13	151	6.42

reliable to identify modes with high amplitudes, but can fail or give less accurate results when we deal with low amplitude modes. Identified p-mode frequencies for 51

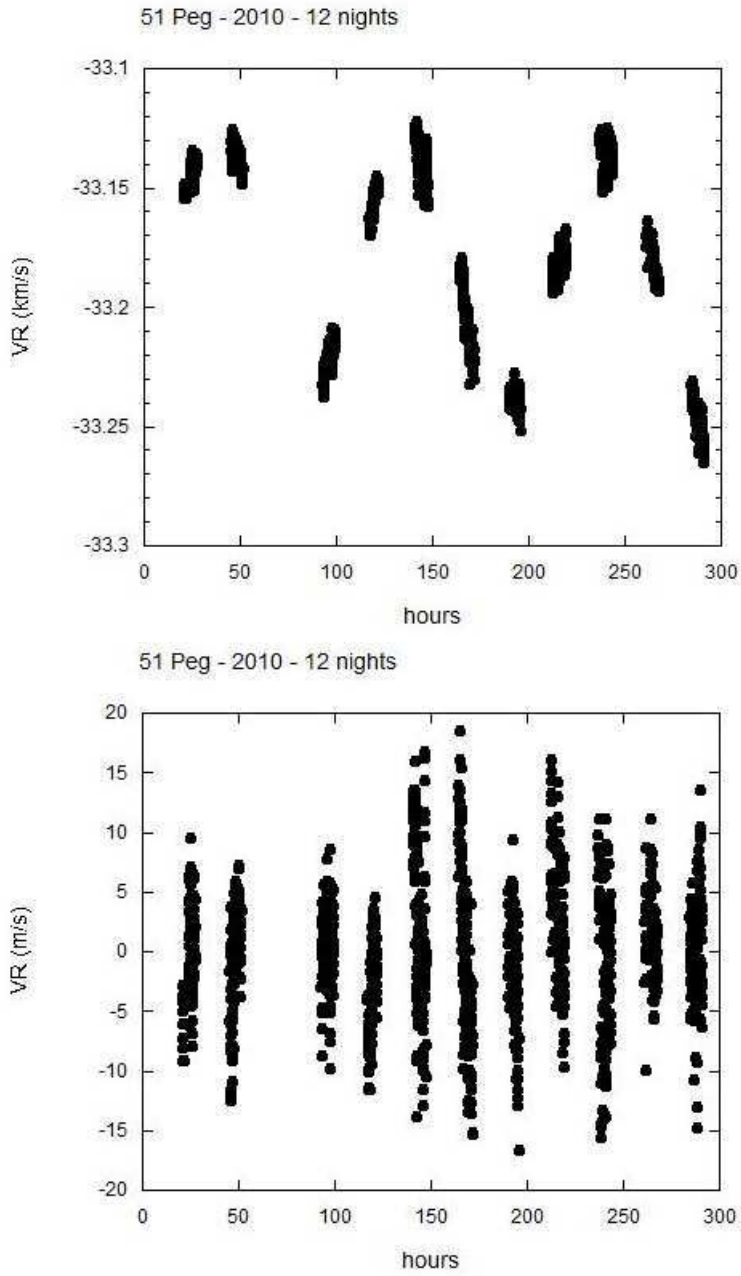

Figure 4.4: Radial velocity curve with the planet included (*upper pannel*) and radial velocity curve with the planet effect removed (*lower pannel*) for 51 Peg, for the observing campaign done in 2010.

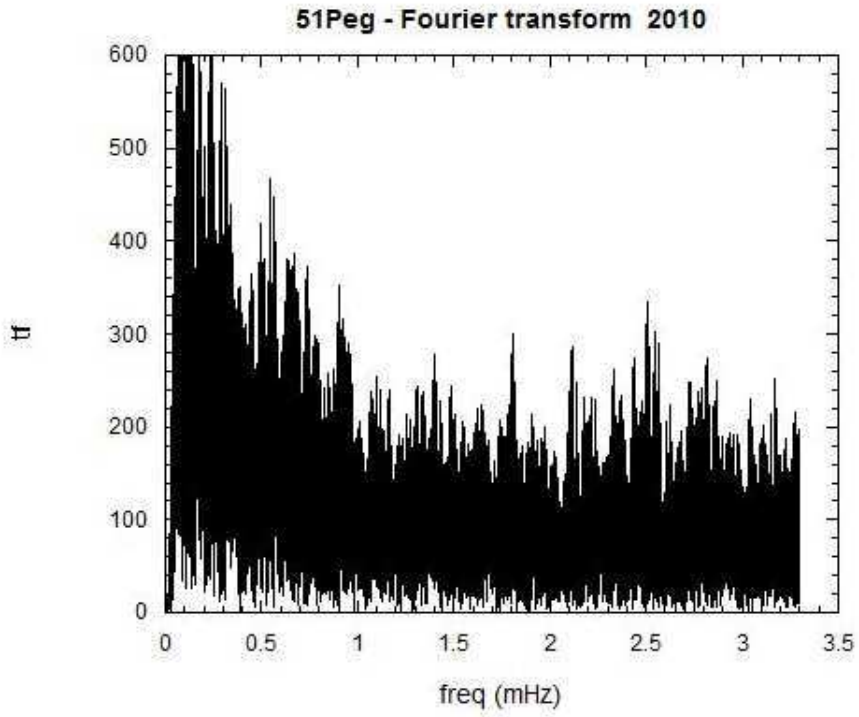

Figure 4.5: Power spectrum obtained from radial velocity measurement of 51 Peg, from observations taken in 2010.

Peg are presented in table 4.6, and their corresponding échelle diagram is presented in figure 4.6. From identified p-mode frequencies, we obtain a large separation of $<\Delta\nu>$=117.5 μHz.

In the future, it would be interesting to observe again 51 Peg with a multi-site campaign to obtain better data with less aliases. Nevertheless we tried to fit models on the observed data to infer the external parameters of the star.

4.4 Preliminary Modeling

Several evolutionary tracks were computed using the TGEC. We used the version which does not include radiative acceleration on heavy elements in the treatment of diffusion, as the mass expected for 51 Peg is smaller than 1.1 Msun, where the role of the radiative accelerations on asteroseismology is negligible. The mixing length parameter was adjusted to the solar value (α = 1.8). We obtained evolutionary tracks for masses ranging from 0.94 $M_\odot$ to 1.12 $M_\odot$. For each track, we searched for

Table 4.6: Identified p-mode frequencies (in μHz) for 51 Peg.

ℓ=0	ℓ=1	ℓ=2	ℓ=3
...	2273.0	...	...
2335.0	2394.0	...	2379.0
2454.0	2514.0	2448.0	2500.0
2572.0	2632.0	2566.0	...
...	2751.0	2683.0	2738.0
2809.0	...	2802.0	...
2927.0	3103.0	2919.0	...
...	...	3157.0	...

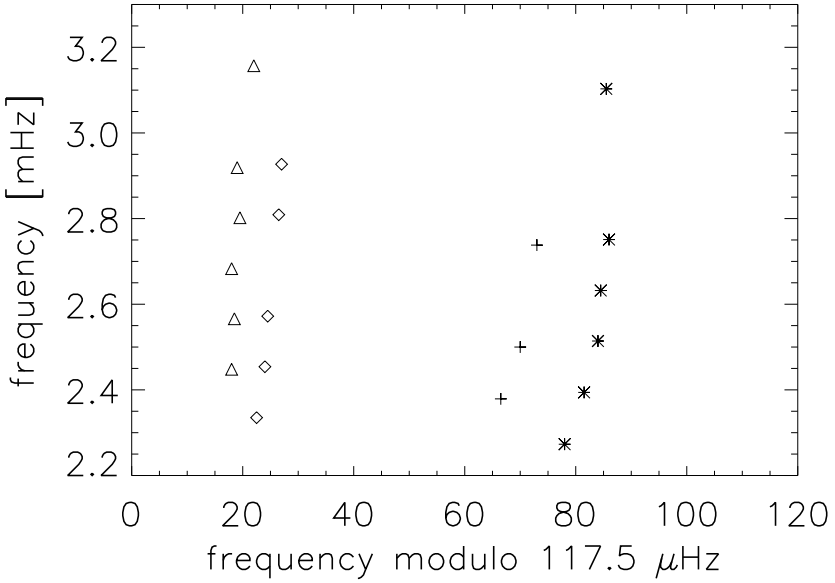

Figure 4.6: Observational échelle diagram for 51, obtained from 2010 RV measurements. Frequency modes with angular degree ℓ= 0 (*diamonds*), ℓ=1 (*asterisks*), $\ell = 2$ (*triangles*) and $\ell = 3$ (*crosses*) are displayed. The average large separation is $<\Delta\nu>\sim$117.5 μHz. The horizontal axis has been shifted by 37.5 μHz.

the model which best fit the observational large separation. These models were kept for further analysis. In figure 4.7 we present the computed evolutionary tracks in the log g - log T_{eff} diagram. In the same way as we proceed before, for other stars, an iso-$<\Delta\nu>$ line indicates the models that have a theoretical mean large separation closest to the observational value. Error boxes from the different spectroscopic

studies presented in table 4.1 are also shown.

In table 4.7 the properties for the best-fit models displayed in figure 4.7 are presented. The échelle diagram for m=1.06 $M_{\odot}$ together with observational mode frequencies is presented in figure 4.8.

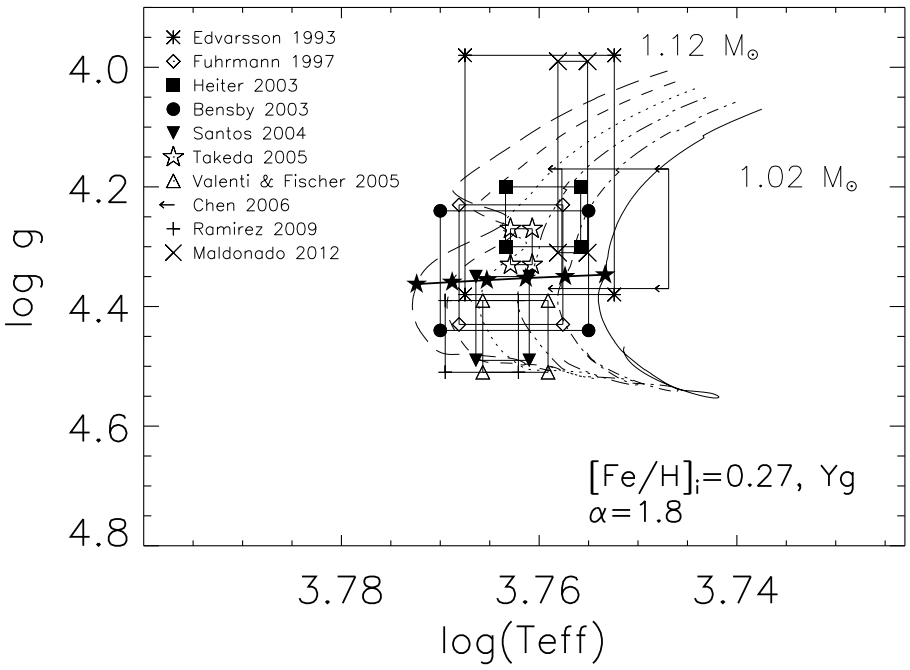

Figure 4.7: Evolutionary tracks in the log g versus log $T_{\rm eff}$ plane for $[Fe/H]_i$ =0.27, Y_i=Y_G and without considering overshooting. The symbols indicate the error boxes of Edvardsson et al. (1993) (*asterisks*), Fuhrmann et al. (1997) (*diamonds*), Heiter & Luck (2003) (*black squares*), Bensby & Feltzing (2003) (*black circles*), Santos et al. (2004b) (*upside down black triangles*), Takeda et al. (2005) (*stars*), Valenti & Fischer (2005) (*triangles*), Chen & Zhao (2006) (*arrows*), Ramirez et al. (2009) (*plus signs*) and Maldonado et al. (2012) (*crosses*). The straight thick line represents the iso-$<\Delta\nu>$ line, with $<\Delta\nu>$=117.5 μHz.

Table 4.7: Examples of models $[Fe/H]_{ini} = 0.27$, $Y_{ini}=Y_G$, α=1.8 and without considering overshooting. $[Fe/H]_i$ and Y_i refer to initial metallicity and helium abundance of the model, and, $[Fe/H]_s$ and Y_s to the surface metallicity of the model at the given age.

$[Fe/H]_i$	Y_i	$M/M_\odot$	Age [Gyr]	$[Fe/H]_s$	Y_s	$\log g$ [K]	$\log T_{\rm eff}$	$\log (L/L_\odot)$	$R/R_\odot$	M/R^3 [solar units]	$<\Delta\nu>$ [μHz]	$<\delta\nu_{02}>$ [μHz]
0.27	0.298	1.02	6.957	0.20	0.252	4.346	3.753	0.067	1.127	0.71	117.55	5.34
0.27	0.298	1.04	6.119	0.20	0.254	4.349	3.757	0.089	1.134	0.71	117.50	5.93
0.27	0.298	1.06	5.327	0.20	0.256	4.352	3.761	0.111	1.141	0.71	117.51	6.54
0.27	0.298	1.08	4.579	0.20	0.259	4.356	3.765	0.131	1.147	0.71	117.54	7.19
0.27	0.298	1.10	3.861	0.21	0.262	4.359	3.769	0.150	1.154	0.71	117.55	7.90
0.27	0.298	1.12	3.218	0.21	0.265	4.362	3.772	0.169	1.159	0.72	117.56	8.57

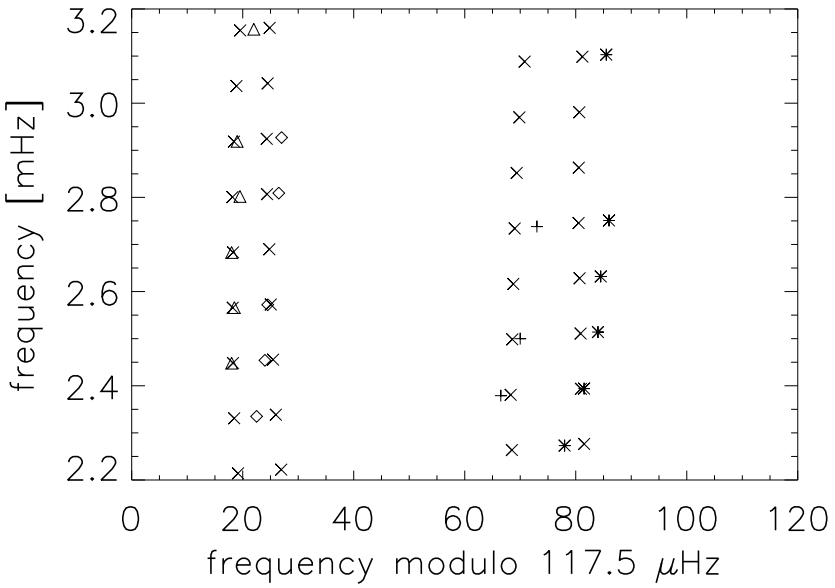

Figure 4.8: Échelle diagram for 51 Peg, obtained for m=1.06 $M_\odot$, [Fe/H]=0.27 and Y_g. Theoretical frequencies are represented by crosses. Observational p-mode frequencies are represented by diamonds ($\ell = 0$), asterisk ($\ell = 1$), triangles ($\ell = 2$), and plus signs ($\ell = 3$). The horizontal axis has been shifted by 37.5 μHz

4.5 Conclusion

We presented mode identification and a preliminary modeling for the star 51 Peg, the first star around which an orbiting exoplanet was found. Observations were done using the SOPHIE spectrograph installed at the Haut Provence Observatory, France. Two observing runs were carried out: the first one in August 2007, and a second one in August 2010. Mode identification was possible, for 20 p-mode frequencies.

Preliminary modeling has been done by computing different models using the TGEC and obtaining theoretical mode frequencies using the PULSE code. At this stage, evolutionary tracks were computed for the most probable set of chemical composition, that is $[Fe/H]_s$=0.20 and an initial helium abundance of Y_{ini}=Y_G. The best stellar parameters that we deduce from these computations are:

- M = 1.06±0.02 $M_\odot$
- Age = 5.3±0.8 Gyr

- $\log g = 4.35 \pm 0.04$
- $T_{\rm eff} = 5770 \pm 50$ K
- $\log L/L_{\odot} = 0.11 \pm 0.02$
- $R/R_{\odot} = 1.14 \pm 0.01$

We can see that all these values lie in the spectroscopic range (Table 4.1). It is interesting to note that the radius that we find is in good agreement with the value obtained using the PTI experiment, which is 6% smaller than the value obtained with the CHARA experiment (van Belle & von Braun, 2009). We also note that our present results are close to the model proposed by Murphy et al. (2004). Before giving a definitive conclusion about the uncertainties on these determinations, we need to compute other models with different chemical compositions (especially for helium, which is not spectroscopically observed) and study the possible influence of near-surface effects. This is presently underway.

Conclusion

This thesis work had several purposes. First we wanted to characterize in a detailed way some central stars of planetary systems using asteroseismic methods, and compare the results we obtained with those given by automatic procedures when available. Second we were interested in investigating whether asteroseismology may give some hints about the difference between stars with and without observed planets.

To reach these purposes, we deeply studied three exoplanet-host stars:

- HD 52265, the CoRoT main target observed continuously during more than one month, gave the most precise results as the observed frequencies presented no or very little aliases (the only ones being due to the South Atlantic Anomaly). We could do a very precise analysis of this star and find precise results on its mass, radius, age, and external gravity. We could compare these results with those obtained using two different automatic procedures: SEEK and AMP. While the second one gave results very similar to ours, the first one gave somewhat different values for the stellar parameters. In our discussion in chapter 2, we suggest that the difference is basically due to a wrong helium value found by the SEEK code. In these automatic codes, many different parameters are treated together, and the fact that it settles on one maximum of probability is sometimes a delicate process. If one of the parameters is not quite correct, the other ones follow. In this case, we noticed that the results given by SEEK correspond to a secondary maximum of probability in AMP. This shows the limits of automatic methods.

- 94 Ceti was observed with HARPS (Chile) during 8 nights. This was a mono-site observation and we suffered from the day-gap induced aliases in the identification of the oscillation modes. However we were able to obtain good results with the determination of external parameters of this star. The aim of this particular choice was that a "twin" of 94 Ceti, β Virginis, had already been studied with asteroseismology by other authors. Contrary to 94 Ceti, β Virginis has no observed planet. Whereas 94 Ceti presents an overabundance of heavy elements, β Virginis has normal abundances. We hoped to be able to

obtain some asteroseismic clear differences between both stars, which could be related to the presence of planets. Unfortunately it appeared that the precision obtained on both stars, β Virginis first, 94 Ceti in second, was not sufficient to reach that purpose.

- 51 Peg was also observed from a ground-based instrument, SOPHIE (OHP), during two runs of 8 and 12 nights respectively. I myself did observations in the second run. During these observations, we had several problems with the weather first, but also with the instrument which was not always stable in temperature. The noise in the data is much larger than for 94 Ceti and the solar like oscillations were difficult to characterize. The aliases problem was also very important. The characteristic structure of solar like oscillations in the Fourier transform appear more clearly in the second run that in the first one. They seem to lie around 2.5 μHz. Mode identifications were done using comparisons between the two Fourier transform. The results lead to models with a large separation of $\sim$ 117 μHz and models similar to the ones computed by Murphy et al. (2004). More work should be done on this star in the future.

At the present time, so many stars are observed with *Kepler* that simplified procedures are used for their characterization. The *Kepler* team has shown that the knowledge of the large separation, which may be easily obtained from space data, is enough to obtain the stellar radius with a few percent accuracy. The knowledge of this radius is very important for exoplanets characterization. However, when one wants to reach a good determination of all stellar parameters, it is important to do complete modeling with correct chemical abundances. In this respect, whereas the metallicity is an observed parameter, this is not the case for the helium content. We have shown that differences in the assumed helium internal abundance may lead to large differences in the derived parameters. Tests of the errors which may be made if the right chemical composition is not taken into account are shown in chapter 1, with the so-called "JCD diagrams".

Another purpose of our computations was to test the importance of introducing radiative accelerations in the treatment of atomic diffusion. Radiative accelerations on a number of heavy elements are introduced in the TGEC code, so that stellar evolution can be computed with and without this effect. As the three stars that we studied have different masses, 94 Ceti being the most massive one, we could check that introducing radiative accelerations do not change the final results on the stellar parameters for masses smaller than 1.4 Msun. On the other hand, it begins to have some effect for larger masses. For 94 Ceti, the difference is of a few percent only.

In conclusion, we showed that asteroseismology is a very good tool to obtain precise values of the stellar external parameters. The results obtained from space observations are much more precise than those obtained from the ground, provided

that the star may be observed on a long enough time, like HD 52265. For ground-based observations, the importance of having access to multi-site simultaneous observations is clear. In this respect, the SONG (Stellar Oscillation Network Group) project, which is presently in progress with already one node in Canary Islands, one node in China and in the near future one node in Chile, will help getting more precise data.

During these 4 years of thesis work I have performed asteroseismic studies of solar-like stars with orbiting exoplanets, both on the observing side (doing observations in OHP) and on the modeling side. I obtained some interesting results, which may be a little step in the evolution of knowledge for these stars and the planetary systems. I studied several techniques and will be happy now to go back to my own country, Chile, and try to exploit there what I have learned in France.

Conclusion

Ce travail de thèse avait plusieurs buts. D'une part nous voulions caratériser d'une manière détaillée des étoiles centrales de systèmes planétaires en utilisant des méthodes d'astérosismologie, et comparer nos résultats avec ceux obtenus en utilisant des procédures automatiques. D'autre part nous étions intéressés à déterminer si l'astérosismologie pouvait donner quelques indications au sujet de la différence entre les étoiles avec ou sans planètes détectées.

Pour atteindre ces objectifs, nous avons étudié en détail trois étoiles centrales de systèmes planétaires:

- HD 52265, la seule cible principale de CoRoT, étoile centrale de système planétaire, observée en continu pendant plus d'un mois. Nous avons obtenu avec cette étoile les résultats les plus précis puisque les fréquences obserées ne comportaient pas ou peu d'alias (les seuls alias provenant des passages du satellite dans l'anomalie sud-atlantique). Nous avons pu effectuer une analyse très précise de cette étoile et obtenir des résultats précis sur sa masse, son rayon, son âge et sa gravité superficielle. Nous avons pu comparer ces résultats avec ceux obtenus en utilisant deux procédures automatiques différentes: SEEK et AMP. Alors que la seconde donnait des résultats semblables aux nôtres, la première donnait des valeurs différences pour les paramètres stellaires. Dans notre discussion, chapitre 2, nous suggérons que ces différences sont principalement dues à une erreur sur la valeur de l'abondance de l'hélium trouvée par le code SEEK. Dans ces codes automatiques, de nombreux paramètres différents sont traités ensemble, et le fait que le système choisisse un certain maximum de probabilité est parfois un processus délicat. Si l'un des paramètres n'est pas tout à fait correct, les autres suivent. Dans notre cas, nous avons remarqué que les résultats donnés par SEEK correspondaient à un maximum secondaire de probabilité dans AMP. Ceci montre les limites des méthodes automatiques.

- 94 Ceti a été observée avec HARPS (Chili) pendant 8 nuits. Il s'agissait d'une observation monosite et les données étaient polluées par les alias dus à l'interruption journalière, ce qui rendait difficile l'identification des modes. Malgré cela nous avons pu obtenir de bons résultats sur la détermination des

paramètres externes de cette étoile. Le but de ce choix particulier était de comparer 94 Ceti avec sa "jumelle" β Virginis, qui avait déjà été étudiée par l'astérosismologie par d'autres auteurs. Alors que 94 Ceti présente une surabondance des éléments lourds, β Virginis a des abondances normales. Nous espérions pouvoir obtenir des différences significatives entre les deux étoiles, qui pourraient être reliées à la présence de planètes. Malheureusement il est apparu que la précision obtenue pour les deux étoiles, β Virginis d'abord, 94 Ceti ensuite, n'était pas suffisante pour atteindre ce but.

- 51 Peg a aussi été observée depuis un instrument au sol, SOPHIE (OHP), pendant deux campagnes d'observation de respectivement 8 et 12 nuits. J'ai moi-même effectué une partie des observations de la deuxième campagne. Pendant ces observations, nous avons eu plusieurs problèmes avec le mauvais temps d'une part, mais aussi avec l'instrument qui n'était pas toujours stable en température. Le bruit dans les données est beaucoup plus important que pour 94 Ceti et les oscillations étaient difficiles à caractériser. La structure caractéristique des oscillations solaires and la transformée de Fourier apparait plus clairement dans la seconde campagne que dans la première. Elles semblent se situer autour de 2.5 μHz. Nous avons effectué les identifications de modes en utilisant des comparaisons entre les deux transformées de Fourier. Ces résultats conduisirent à une grande séparation de 117 μHz et à des modèles semblables à ceux calculés par Murphy et al. 2004. Il serait nécessaire d'effectuer plus d'observations de cette étoile dans le futur.

A l'époque actuelle, le nombre d'étoiles observées avec *Kepler* est si grand que des procédures simplifiées doivent être utilisées pour les caractériser. L'équipe de *Kepler* a montré que la connaissance de la grande séparation, qui peut être obtenue facilement à partir des observations spaciales, est suffisante pour obtenir le rayon de l'étoile à quelques pourcents près. La connaissance de ce rayon est très importante pour la caractérisation des exoplanètes. Cependant, si on souhaite atteindre une bonne détermination de tous les paramètres stellaires, il est important de faire des modélisations complètes avec des abondances chimiques correctes. En ce qui concerne ces abondances, il faut noter que, si la métallicité est un paramètre observable, ce n'est pas le cas, en revanche, pour l'abondance d'hélium. Nous avons montré que des différences dans la quantité d'hélium supposée au départ à l'intérieur de l'étoile peuvent conduire à de grandes différences dans les paramètres stellaires obtenus. Des tests sur les erreurs qui peuvent être faites si on ne tient pas correctement compte de la composition chimique sont montrés dans le chapitre 1, avec les diagrammes "grandes séparations - petites séparations", ou encore "diagrammes JCD".

Un autre but de nos calculs était de tester l'importance d'introduire les accélérations radiatives dans le traitement de la diffusion atomique. Les accélérations radia-

tives sur un grand nombre d'éléments lourds sont introduites dans le code TGEC, de telle manière que l'évolution stellaire peut être traitée avec ou sans cet effet. Comme les trois étoiles que nous avons étudiées avaient des masses différentes, 94 Ceti étant la plus massive, nous avons pu vérifier que l'introduction des accélérations radiatives ne change pas les résultats sur les valeurs finales des paramètres stellaires pour des masses inférieures à 1.4 masses solaires. Pour les étoiles plus massives, cela commence à donner des effets importants. Pour 94 Ceti, la différence est seulement de quelques pourcents.

En conclusion, nous avons montré que l'asterosismologie est un très bon outil pour obtenir des valeurs précises des paramètres stellaires. Les résultats obtenus avec des instruments spaciaux sont plus précis que ceux obtenus avec des instruments au sol, pourvu que l'étoile soit observée sur une longue période temporelle, comme HD 52265. Pour les observations au sol, il est clairement important d'avoir accès à des observations multisites. Dans ce cadre, le projet SONG Stellar Oscillation Network Group), actuellement en cours avec déjà un noeud aux iles Canaries, un noeud en Chine et dans un futur proche un noeud au Chili, va être d'une grande aide pour obtenir des données plus précises.

Pendant ces 4 années de thèse, j'ai étudié par des méthodes d'astérosismologie des étoiles de type solaire possédant des planètes, à la fois sur le plan observationnel (observations à l'OHP) et sur le plan de la modélisation. J'ai obtenu des résultats intéressants, qui peuvent représenter une petite étape dans l'évolution des connaissances pour ces étoiles et pour les systèmes planétaires. J'ai étudié plusieurs techniques et je serai maintenant heureuse de retourner dans mon pays, le Chili, et d'essayer d'exploiter là-bas ce que j'ai appris en France.

Publications

Publications in rank A Journals:

- *Precise modeling of the exoplanet host star and CoRoT main target HD 52265*, **Escobar, M. E.**; Théado, s.; Vauclair, V.; Ballot, J.; Charpinet, S.; Dolez, N.; Hui-Bon-Hoa, A.; Vauclair, G.; Gizon, L.; Mathur, S.; Quirion, P.-O.; Stahn, T., 2012, A&A, Volume 543, A96.

Conference Proceedings

- *Precise Modeling of the Exoplanet Host Star and CoRoT Main Tarjet HD 52265*, **Escobar, M. E**; Théado, S.; Vauclair, S.; Ballot, J.; Dolez, N.; Charpinet, S.; Vauclair, G.; Gizon, L., 2011, Proceedings of 20th Stellar Pulsation Conference Series "Impact of New Intrumentation and New Insights in Stellar Pulsations", Granada, Spain.

- *Asteroseismology of the CoRoT main target HD 52265*, **Escobar, M. E**; Théado, S.; Vauclair, S.; Ballot, J.; Dolez, N.; Charpinet, S.; Vauclair, G.; Gizon, L., 2011, Proceedings of 2nd Stellar CoRoT Symposium "Transiting Planets, Vibrating Stars and their Connection", Marseille, France.

In Preparation

- *Asteroseismology of the exoplanet-host star 94 Cet*, **Escobar, M.E.**; Vauclair, S.; Vauclair, G.; Théado, S.; Dolez, N., 2013.

- *Asteroseismology of the exoplanet-host star 51 Pegasi*, **Escobar, M.E.**; Vauclair, S.; Vauclair, G., 2013-2014.

Publication 1

Precise modeling of the exoplanet host star and CoRoT main target HD 52265

M. E. Escobar; S. Théado; V. Vauclair; J. Ballot; S. Charpinet; N. Dolez; A. Hui-Bon-Hoa; G. Vauclair; L. Gizon; S. Mathur; P.-O. Quirion; T. Stahn2012, A&A, Volume 543, A96.

Cet article présente une étude détaillée et précise des caractéristiques de l'étoile centrale de système planétaire, cible principale de Corot, HD 52265, à partir de l'astérosismologie. Les résultats sont comparés avec les estimations précédentes obtenues par d'autres auteurs, avec une discussion générale. La méthode de base est semblable à celle déjà utilisée par le groupe de Toulouse pour les étoiles de type solaire. Les modèles sont calculés avec plusieurs compositions chimiques initiales et les fréquences calculées pour les modes p sont comparées avec les fréquences observées. Tous les modèles incluent la diffusion atomique et l'importance de l'accélération radiative est discutée. Plusieurs tests sont utilisés, en particulier les combinaisons habituelles de fréquences et les comparaisons précises de diagrammes échelle. Les effets de surface sont introduits et discutés. Des codes automatiques ont aussi été utilisés pour trouver le meilleur modèle pour cette étoile (SEEK, AMP) et leurs résultats sont comparés avec ceux que nous obtenons en utilisant la méthode détaillée. Nous trouvons des résultats précis pour la masse, le rayon et l'âge de cette étoile, ainsi que sa température effective et sa luminosité. Nous donnons aussi une estimation de l'abondance initiale d'hélium. Ces résultats sont importants pour la caractérisation du système stellaire.

2012, Astronomy & Astrophysics, Volume 543, A96

A&A 543, A96 (2012)
DOI: 10.1051/0004-6361/201218969
© ESO 2012

Astronomy & Astrophysics

Precise modeling of the exoplanet host star and CoRoT main target HD 52265

M. E. Escobar[1], S. Théado[1], S. Vauclair[1,2], J. Ballot[1], S. Charpinet[1], N. Dolez[1], A. Hui-Bon-Hoa[1], G. Vauclair[1], L. Gizon[3,4], S. Mathur[5], P. O. Quirion[6], and T. Stahn[4]

[1] Institut de Recherche en Astrophysique et Planétologie, Observatoire Midi-Pyrénées, CNRS, Université Paul Sabatier, 14 Avenue Édouard Belin, 31400 Toulouse, France
e-mail: mescobar@irap.omp.eu
[2] Institut universitaire de France, 103 boulevard Saint Michel, 75005 Paris, France
[3] Max-Planck-Institut für Sonnensystemforschung, Max-Planck-Str. 2, 37191 Katlenburg-Lindau, Germany
[4] Institut für Astrophysik, Georg-August-Universität Göttingen, Friedrich-Hundt-Platz 1, 37077 Göttingen, Germany
[5] High Altitude Observatory, NCAR, PO Box 3000, Boulder, CO 80307, USA
[6] Canadian Space Agency, 6767 Boulevard de l'Aroport, Saint-Hubert, QC, J3Y 8Y9, Canada

Received 6 February 2012 / Accepted 23 May 2012

ABSTRACT

Aims. This paper presents a detailed and precise study of the characteristics of the exoplanet host star and CoRoT main target HD 52265, derived from asteroseismic studies. We compare our results with previous estimates, and provide a comprehensive summary and discussion.
Methods. Our basic method is similar to that previously used by the Toulouse group for solar-type stars. Models are computed with various initial chemical compositions and the computed p-mode frequencies are compared with the observed ones. All models include atomic diffusion and we discuss the importance of radiative accelerations. Several tests are used, including the usual frequency combinations and the fits to the échelle diagrams. Possible surface effects are introduced and discussed. Automatic codes are also used to identify the best-fit model for this star (SEEK and AMP) and their results are compared with those obtained with the detailed method.
Results. We find precise results for the mass, radius, and age of this star, as well as its effective temperature and luminosity. We also estimate the initial helium abundance. These results are important for the characterization of the star-planet system.

Key words. planet-star interactions – stars: interiors – stars: evolution – stars: late-type – stars: fundamental parameters – asteroseismology

1. Introduction

In the past few years, the number of observed exoplanets has increased dramatically, owing to missions such as CoRoT (Baglin et al. 2006) and *Kepler* (Koch et al. 2010), as well as many other ground-based and space missions (see the exoplanet encyclopedia for a complete summary[1]). The precise characterization of exoplanet host stars becomes more and more important in the framework of the detailed studies of the observed planetary systems. Constraints on the parameters and internal structure of the star can be obtained by comparing models with photometric and spectroscopic observations (Southworth 2011; Basu et al. 2012), but the highest precision is obtained from asteroseismology, when the stellar oscillations may be observed and analyzed. This was the case, for example, for the exoplanet host stars (EHS) ι Hor (Vauclair et al. 2008) and μ Arae (Soriano & Vauclair 2010), both observed with HARPS, as well as the EHS HAT-P-7, HAT-P-11, and TrES-2 (Christensen-Dalsgaard et al. 2010), observed with *Kepler*.

Among the EHS, the star HD 52265 is one of the most precisely observed for asteroseismology, as it was the only EHS observed as a main target by CoRoT. This G0V metal-rich main sequence star has an orbiting jupiter-mass planet at 0.5 AU with a period of 119 days (Naef et al. 2001; Butler et al. 2000). It was continuously observed between December 13, 2008 and March 3, 2009, that is 117 consecutive days. As a result, 31 p-mode frequencies were reported, between 1500–2550 μHz, corresponding to $\ell = 0$, 1, and 2 (Ballot et al. 2011). From this analysis, a large separation of $\langle\Delta\nu\rangle = 98.4 \pm 0.1$ μHz and a small separation of $\langle\delta\nu_{02}\rangle = 8.1 \pm 0.2$ μHz were found, and a complete asteroseismic analysis including mode lifetimes was presented. An extensive study of the seismic rotation of HD 52265 was performed by Stahn (2011) and Gizon et al. (2012).

Spectroscopic observations of this star have been performed by several groups, who provide different values of the observed triplet ([Fe/H], $\log g$, $T_{\rm eff}$). Their results are given in Table 1. Some of these groups also observed lines of other elements, and gave detailed relative abundances. The results show that there is an overall overmetallicity in this star, which is similar for most heavy elements, with a small dispersion. The Hipparcos parallax is 34.54 ± 0.40 mas (van Leeuwen 2007), which leads to a luminosity value $\log L/L_\odot = 0.29 \pm 0.05$. A spectroscopic follow-up was also done with the Narval spectropolarimeter installed on the Bernard Lyot telescope at Pic du Midi Observatory (France) during December 2008 and January 2009, i.e., during CoRoT observations. No magnetic signature was observed.

Preliminary modeling of this star, using spectroscopic constraints, was done by Soriano et al. (2007), as preparation to CoRoT observations. Evolutionary tracks were computed using the Toulouse-Geneva evolution code (TGEC). According to the spectroscopic constraints, eight models with masses between

[1] http://exoplanet.eu/index.php

Table 1. Summary of previous spectroscopic studies of HD 52265.

[Fe/H]	$T_{\rm eff}$	log g	Reference
0.27 ± 0.02	6162 ± 22	4.29 ± 0.04	Gonzalez et al. (2001)
0.23 ± 0.05	6103 ± 52	4.28 ± 0.12	Santos et al. (2004)
0.19 ± 0.03	6069 ± 15	4.12 ± 0.09	Takeda et al. (2005)
0.19 ± 0.03	6076 ± 44	4.26 ± 0.06	Fischer & Valenti (2005)
0.24 ± 0.02	6179 ± 18	4.36 ± 0.03	Gillon & Magain (2006)
0.19 ± 0.05	6100 ± 60	4.35 ± 0.09	Ballot et al. (2011)

1.18 $M_\odot$ and 1.30 $M_\odot$ and metallicities ranging from 0.19 to 0.27 were chosen for further analysis, and adiabatic p-modes frequencies were computed. Echelle diagrams for each selected model were presented as well as their corresponding large and small separations. A large separation around ∼100 μHz was predicted from these models except for the Takeda et al. (2005) values, which corresponded to a smaller large separation (around ∼75 μHz).

The detailed CoRoT observations allow us to progress in this analysis, using the precise seismic results. First of all, the Takeda et al. (2005) values,which correspond to a more evolved star, are excluded. We now present a complete asteroseismic analysis for HD 52265, and give precise results for the stellar parameters.

The method and models used for the asteroseismic comparisons with observations are described in Sect. 2. All the models, as described in Sect. 2.1, include element gravitational settling. The seismic tests are discussed in Sect. 2.2 and we discuss the influence of radiative accelerations on heavy elements in Sect. 2.3. The results are given in Sect. 3. Section 3.1 is devoted to the results obtained without taking surface effects into account. An analysis of surface effects and their consequences for our results is given in Sect. 3.2. A first discussion of the results is given in Sect. 3.3. Finally, in Sect. 4 the results obtained using automatic codes to find the best-fit models for this star from seismology (SEEK and AMP) are presented and compared with the previously obtained solutions. A summary and discussion are given in Sect. 5.

2. Computations with TGEC

2.1. Stellar models

Stellar models were computed using the TGEC code (Hui-Bon-Hoa 2008; Théado et al., in prep.), with the OPAL equation of state and opacities (Rogers & Nayfonov 2002; Iglesias & Rogers 1996), and the NACRE nuclear reaction rates (Angulo et al. 1999). Convection was treated using the mixing length theory. For all models, the mixing length parameter was adjusted to that of the solar case, i.e. $\alpha = 1.8$ without either overshooting or extra-mixing. Gravitational settling of helium and metals was included using the Paquette prescription (Paquette et al. 1986; Michaud et al. 2004). Radiative accelerations of metals were also introduced using the SVP method (Single Valued Parameters approximation, see Alecian & LeBlanc 2002; LeBlanc & Alecian 2004; Théado et al. 2009). As most stellar evolution codes neglect these radiative accelerations, we analyzed the effects on the seismic results of introducing them or not.

Evolutionary tracks were computed for two metallicity values and two different initial helium abundances. The metallicity values were chosen as [Fe/H] = 0.23 and 0.30, so that after diffusion the final model value lies inside the observed range. Here [Fe/H] represents the global overmetallicity with respect to the Sun, defined as $[\log(Z/X)_* - \log(Z/X)_\odot]$, where Z and X are computed at the stellar surface. Considering the small dispersion in the detailed abundances, this value may be compared with the observed [Fe/H]. A discussion of the computed detailed abundance variations is given in Sect. 2.3. The initial helium values are labeled $Y_\odot$ and $Y_{\rm G}$, where $Y_\odot$ is the solar helium value taken from Grevesse & Noels (1993) and $Y_{\rm G}$ is a helium abundance that increases with Z as expected if the local medium follows the general trend observed for the chemical evolution of galaxies (cf. Izotov & Thuan 2004, 2010).

Adiabatic oscillation frequencies were computed for many models along the evolutionary tracks using the PULSE code (Brassard & Charpinet 2008). We computed these frequencies for degrees $\ell = 0$ to $\ell = 3$. For comparisons with the observations (seismic tests), we used the same frequency interval for both computed and observed frequencies for consistency, i.e. between 1500 μHz and 2550 μHz, as discussed below.

2.2. Seismic tests

A well-known characteristic of p-modes in spherical stars is that modes of the same degree with successive radial order n are nearly equally spaced in frequency (e.g. Tassoul 1980). The large separation is defined as

$$\Delta\nu_{n,\ell} = \nu_{n+1,\ell} - \nu_{n,\ell}. \quad (1)$$

In real stars, this large separation varies slightly with frequency, so that an average value has to be used for comparisons between models and observations. One has to be careful to use the same frequency range in both cases to do the comparisons. Taking this into account, the fit between the computed and measured large separations is the first step in the process of comparisons. The large separation gives access to the stellar average density (Ulrich 1986; White et al. 2011).

A second characteristic of the p modes is that the difference between (n, ℓ) and $(n-1, \ell+2)$ modes varies very slowly with frequency. The small separations are defined as

$$\delta\nu_{n,\ell} = \nu_{n,\ell} - \nu_{n-1,\ell+2}. \quad (2)$$

These small separations are most sensitive to the stellar core and may provide information on the extension of the convective core in some stars (Tassoul 1980; Roxburg & Vorontsov 1994; Gough 1986; Soriano & Vauclair 2008).

Provided that the stellar chemical composition is precisely known, the knowledge of both the large and the small separations, which may be plotted in the so-called C-D diagrams, gives strong constraints on the stellar parameters (Christensen-Dalsgaard 1984; White et al. 2011). However, while the stellar metallicity can be derived precisely from spectroscopy, the helium content of solar-type stars cannot be directly inferred from observations. This ignorance leads to important uncertainties in the evolutionary tracks, thus in the derived stellar parameters.

We analyzed these uncertainties in detail by computing models with various chemical compositions. For each stellar evolutionary track that we computed, we first searched for the model that had an average large separation of $\langle\Delta\nu\rangle = 98.4 \pm 0.1$ μHz. As the large separation continously decreases when the star evolves along the main sequence, one model only is found with the observed value (within the uncertainties). For each set of computations done with a given initial chemical composition ([Fe/H] and Y), we then searched for the model that most closely fitted the small separations observed between modes of $\ell = 2$ and 0, $\langle\delta\nu_{02}\rangle = 8.1 \pm 0.2$ μHz. We further proceed with detailed comparisons of observed and computed échelle diagrams.

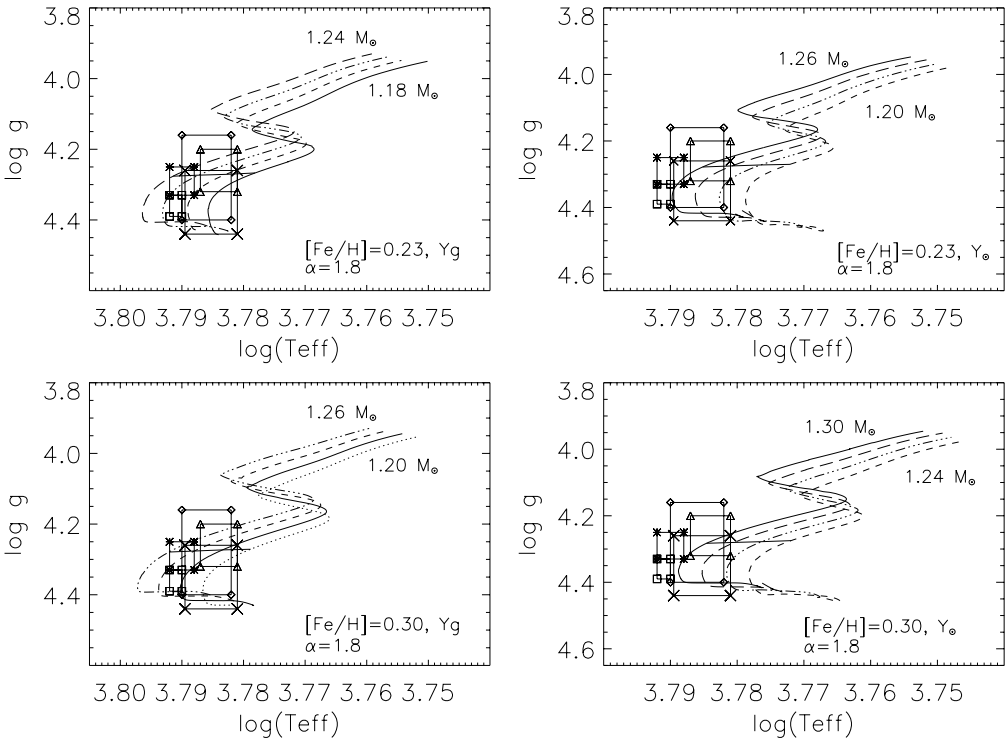

Fig. 1. Evolutionary tracks in the log g versus log $T_{\rm eff}$ plane for the various sets of metallicities and helium abundance, for α = 1.8 (see text for details). The symbols indicate the error boxes of Gonzalez et al. (2001) (asterisks), Santos et al. (2004) (diamonds), Gillon & Magain (2006) (squares), Fisher & Valenti (2005) (triangles), and Ballot et al. (2011) (crosses). The straight thick line represents the iso-$\langle\Delta\nu\rangle$ line, with $\langle\Delta\nu\rangle$ = 98.4 μHz.

In our final comparison between the models and the seismic observations, we need to take into account the surface effects induced by the wave behavior in the outer stellar layers. We computed the frequency shift induced by these effects, using the recipe proposed by Kjeldsen et al. (2008). In this case, the large separations are modified, as discussed in Sect. 3.2, which leads to corrections in the results.

2.3. Test on atomic diffusion: radiative accelerations

Atomic diffusion is a very important process inside stars: it can modify the atmospheric abundances and also have strong implications for the internal structure of stars (Richard et al. 2001; Michaud et al. 2004; Théado et al. 2009). At the present time, most stellar evolution codes include the computation of gravitational settling, but not the computation of radiative accelerations of heavy elements. These accelerations, which oppose gravitation, are negligible for the Sun but significant for more massive stars (Michaud et al. 1976). The variations with depth in the radiative accelerations of specific elements can lead to either their accumulation or depletion in various layers inside stars. The presence of a heavy iron layer above layers with smaller molecular weights creates an inverse μ-gradient that is unstable towards thermohaline convection (Vauclair 2004). This induced mixing has also to be taken into account in computations of stellar modeling (Théado et al. 2009). An improved TGEC version including radiative accelerations on C, N, O, Ca, and Fe has been developed (Théado et al., in prep.). This new version was used to compare the oscillation frequencies computed with and without introducing the radiative accelerations in the models. For solar-type stars (masses less than 1.30 $M_{\odot}$), we found that the difference in the computed frequencies is small. Two models with the same mass of 1.28 $M_{\odot}$ and the same average large separations of 98.26 μHz, one computed with the radiative accelerations and one neglecting them, display differences in the average small separations on the order of 0.01 μHz. These differences between the two models decrease with decreasing stellar mass. We conclude that the radiative accelerations may be neglected in the following computations.

The result that radiative accelerations have no important consequences for the present models is consistent with the detailed abundances not showing large relative variations for the observed elements (Sect. 1). In the case of gravitational settling, the abundances of heavy elements all decrease in a similar way, in spite of their different masses, owing to the slowing down effect of the Coulomb forces. The diffusion velocities typically vary as A/Z^2 where A is the mass number and Z the charge, which is similar for various elements in stellar conditions. This behavior would be different if radiative accelerations were important.

3. Results

3.1. Computations without surface effects

The computations of evolutionary tracks with two initial metallicity values, [Fe/H] = 0.23 and 0.30, and two different helium abundances, the first $Y_{\odot}$ equal to 0.271, and the second $Y_{\rm G}$ equal to 0.293 and 0.303 for the two metallicity values, leads to four different sets of tracks, each of them covering masses from 1.10 $M_{\odot}$ to 1.30 $M_{\odot}$. A few of these tracks are presented in Figs. 1 and 2. Error boxes of five of the spectroscopic studies given in Table 1 are also drawn in these figures.

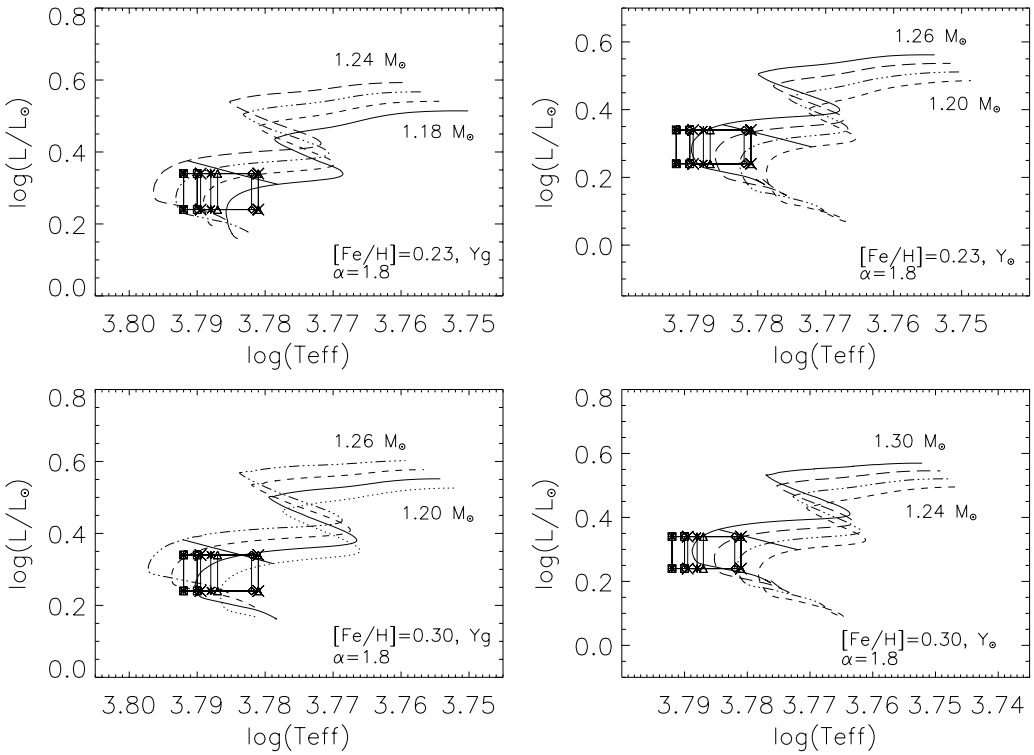

Fig. 2. HR diagrams for $\alpha = 1.8$ (see text for details). Error boxes are the same horizontally as presented in Fig. 1, for the effective temperatures, and correspond vertically to the luminosity uncertainty. The straight thick line represents the iso-$\langle\Delta\nu\rangle$ line, with $\langle\Delta\nu\rangle = 98.4$ μHz.

Table 2. Examples of models with $\alpha = 1.8$, without surface effects.

[Fe/H]$_i$	Y_i	$M/M_\odot$	Age [Gyr]	[Fe/H]$_S$	Y_S	log g [K]	log $T_{\rm eff}$	log $(L/L_\odot)$	$R/R_\odot$	M/R^3 [solar units]	$\langle\Delta\nu\rangle$ [μHz]	$\langle\Delta\nu_{02}\rangle$ [μHz]
0.23	0.293	1.18	3.682	0.16	0.246	4.267	3.778	0.310	1.328	0.50	98.31	7.08
0.23	0.293	1.20	3.204	0.16	0.246	4.271	3.782	0.332	1.333	0.51	98.38	7.54
0.23	0.293	1.22	2.820	0.16	0.248	4.273	3.787	0.355	1.341	0.51	98.36	7.85
0.23	0.293	1.24	2.416	0.15	0.242	4.276	3.791	0.375	1.347	0.51	98.34	8.33
0.23	0.271	1.22	3.756	0.16	0.228	4.272	3.776	0.312	1.343	0.51	98.33	7.11
0.23	0.271	1.24	3.283	0.16	0.228	4.275	3.780	0.334	1.349	0.51	98.31	7.80
0.23	0.271	1.26	2.865	0.16	0.230	4.278	3.785	0.355	1.355	0.51	98.34	7.98
0.23	0.271	1.28	2.461	0.16	0.227	4.281	3.789	0.375	1.361	0.51	98.35	8.30
0.30	0.303	1.20	3.209	0.23	0.257	4.271	3.778	0.316	1.333	0.51	98.42	7.35
0.30	0.303	1.22	2.820	0.23	0.258	4.273	3.783	0.339	1.341	0.51	98.35	7.75
0.30	0.303	1.24	2.431	0.23	0.261	4.276	3.787	0.361	1.347	0.51	98.38	8.11
0.30	0.303	1.26	2.072	0.22	0.254	4.282	3.792	0.382	1.354	0.51	98.38	8.59
0.30	0.271	1.24	3.771	0.23	0.231	4.274	3.771	0.299	1.349	0.51	98.32	7.11
0.30	0.271	1.26	3.293	0.23	0.231	4.277	3.776	0.320	1.356	0.51	98.37	7.64
0.30	0.271	1.28	2.865	0.23	0.231	4.280	3.780	0.341	1.363	0.51	98.34	7.87
0.30	0.271	1.30	2.476	0.24	0.233	4.282	3.784	0.362	1.369	0.51	98.39	8.25

As explained in previous sections, we found, along each evolutionary track, a model that has an average large separation consistent with the observed one, computed in the same frequency range, of ~[1.5, 2.5] mHz. The location of all these models in the log g − log $T_{\rm eff}$ plane as well as in the HR diagrams are indicated in Figs. 1 and 2 with iso-$\langle\Delta\nu\rangle$ 98.4 μHz lines. For each case, we also computed the average small separation, $\delta\nu_{n,02}$ (Table 2). We can see that for models with the same large separation, the small separation increases for increasing mass, so that in each case (i.e. for each set of chemical composition), there is a model that is consistent with both the large and small separations. However, when comparing the absolute model frequencies with the observed ones, we find that we must shift the computed frequencies by about 20 μHz to obtain the best fit to the observed ones. This offset is attributed to surface effects. The échelle diagrams corresponding to these best-fit models are given in Fig. 3.

3.2. Computations including surface effects

We know that stellar modeling fails to represent properly the near-surface layers of the stars. As a consequence, there is a systematic offset between the observed and computed frequencies. This offset is independent of the angular degree ℓ and increases

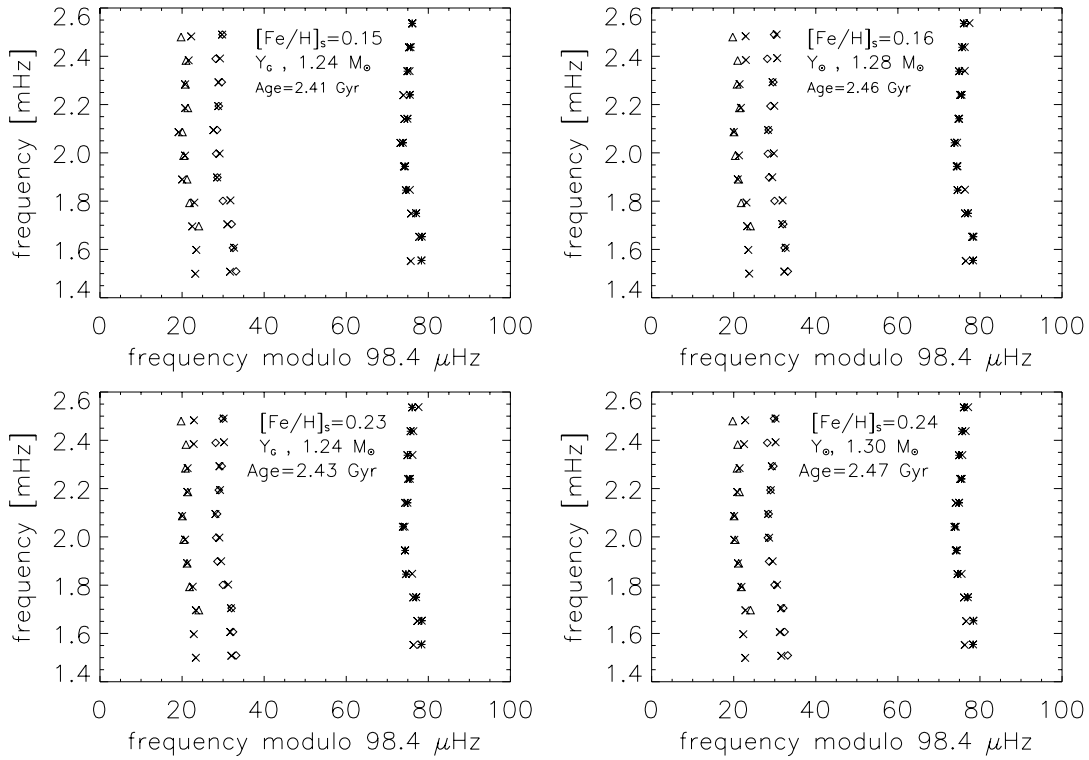

Fig. 3. Echelle diagrams for the best-fit model found for each set of evolutionary tracks calculated with $\alpha = 1.8$. In this set of models, the surface effects are not included. The model frequencies (crosses) are compared to the observed frequencies, wich are represented as diamonds ($\ell = 0$), asterisks ($\ell = 1$), and triangles ($\ell = 2$). To obtain these best fits, we had to shift the model frequencies by respectively (*top left, top right, bottom left, bottom right*) 27, 25, 24, and 22 μHz (see text).

with frequency. This has been studied in the case of the Sun, and a similar offset is expected to occur in other stars. Using the Sun as a reference, Kjeldsen et al. (2008) suggested that for other stars, the near-surface correction to the frequencies may be approximated by

$$\nu_{\rm obs}(n) - \nu_{\rm best}(n) = a \left[\frac{\nu_{\rm obs}(n)}{\nu_0} \right]^b , \quad (3)$$

where $\nu_{\rm obs}(n)$ are the observed $\ell = 0$ frequencies with radial order n, $\nu_{\rm best}(n)$ are the calculated frequencies for the best model, which is the model that most closely describes the star but still fails to correctly model the near-surface layers, and ν_0 is a constant reference frequency chosen to be that of the frequency at the maximum amplitude in the power spectrum. The parameter a may be derived as a function of the parameter b, which has to be adjusted to the solar case. We used this method to determine the frequency corrections that we have to apply to our models, which lead to a new average large separation $\langle \Delta\nu^* \rangle$, which is slightly larger than the observed one. We then proceed as before to derive models for the same sets of values of the helium abundance and metallicity, using $\alpha = 1.8$ (Table 3). Figure 4 presents the échelle diagrams obtained with the new best-fit models. In these graphs, the frequency corrections were applied to the new model frequencies in order to compare them directly with the observations.

3.3. Best-fit models and discussion

We give in Table 4 the parameters of the best-fit models that we obtained for the four different sets of chemical composition. These models have been computed with a mixing length parameter of 1.8, the frequencies have been corrected for surface effects and the computed large and small separations are the closest to the observed ones in the sample. We also give the χ^2 values for the comparisons of the three $\ell = 0, 1, 2$ lines in the échelle diagrams.

Figure 5 displays the large and small separations as a function of the frequency for the observations and the four best-fit models. The pattern observed in the large separations are well-reproduced by the models. For the small separations, the agreement is also very good except for two points at high frequencies (2284 μHz and 2479 μHz). This suggests that the uncertainties given in Ballot et al. (2011) for these points were underestimated.

Several concluding points can already be derived from a first analysis of Table 4. First of all, the stellar gravity is obtained, as usual, with a precision of order 0.1%. The mass and age depend basically on the chosen value for the initial helium content. For a low helium value, the mass is between 1.26 $M_\odot$ and 1.28 $M_\odot$, and the age is 2.73 Gyr, whereas for a higher helium abundance the mass is slightly lower (around 1.22–1.23 $M_\odot$) as well as the age (2.48 to 2.68 Gyr). In any case, the radius and luminosity are known with a precision of order 1%.

We can go further by comparing the effective temperatures of the models with the spectroscopic observations (Fig. 6). As previously found for the cases of ι Hor (Vauclair et al. 2008) and μ Arae (Soriano & Vauclair 2010), the effective temperatures of the best-fit models are lower for lower initial helium abundances and higher for lower metallicities. In the present case, we find that the model with the highest metallicity and the

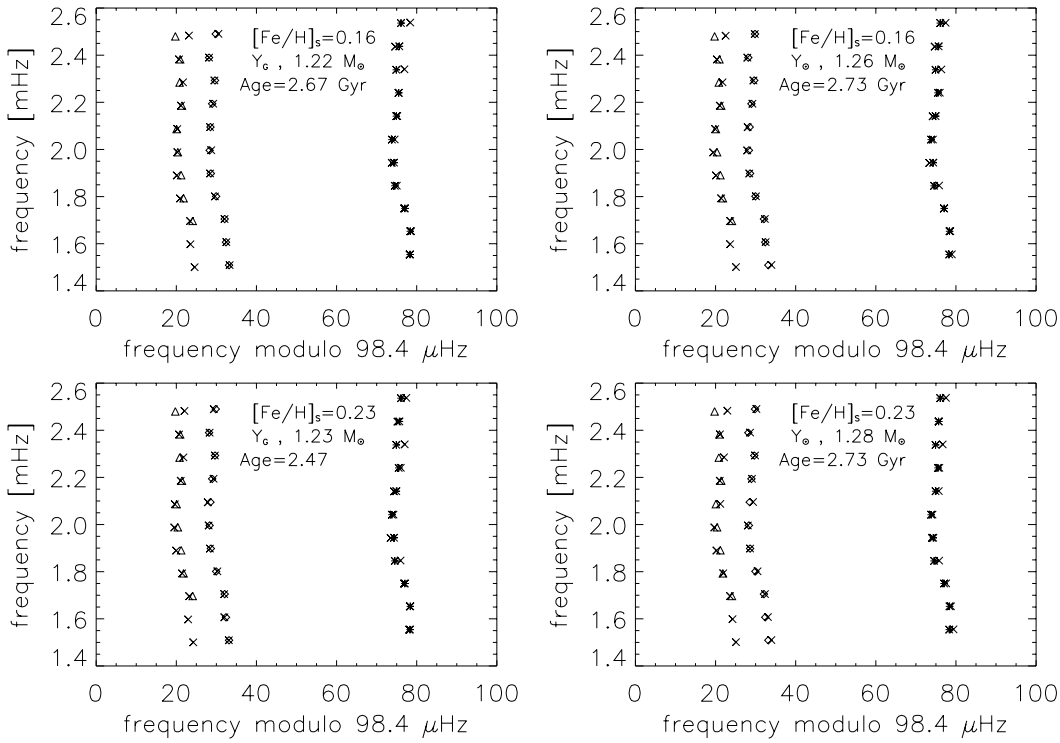

Fig. 4. Echelle diagrams for the best-fit model, including near-surface corrections, as proposed by Kjeldsen et al. (2008), found for each set of evolutionary tracks calculated with $\alpha = 1.8$, in comparison with the observed frequencies. The symbols are the same as those in Fig. 3.

Table 3. Examples of models with $\alpha = 1.8$, including surface effects.

[Fe/H]$_i$	Y_i	$M/M_\odot$	Age [Gyr]	[Fe/H]$_S$	Y_S	log g [K]	log $T_{\rm eff}$	log $(L/L_\odot)$	$R/R_\odot$	M/R^3 [solar units]	$\langle\Delta\nu^*\rangle$ [μHz]	$\langle\Delta\nu\rangle$ [μHz]	$\langle\Delta\nu_{02}\rangle$ [μHz]
0.23	0.293	1.18	3.548	0.16	0.247	4.275	3.779	0.306	1.315	0.52	99.67	98.27	7.27
0.23	0.293	1.20	3.069	0.16	0.247	4.279	3.784	0.328	1.321	0.52	99.68	98.27	7.83
0.23	0.293	1.22	2.670	0.16	0.250	4.282	3.788	0.350	1.327	0.52	99.86	98.19	8.11
0.23	0.293	1.24	2.251	0.16	0.244	4.287	3.792	0.369	1.331	0.52	100.08	98.19	8.47
0.23	0.271	1.20	4.130	0.16	0.228	4.276	3.773	0.287	1.325	0.52	99.51	98.19	6.85
0.23	0.271	1.22	3.622	0.16	0.228	4.279	3.777	0.309	1.331	0.52	99.56	98.18	7.26
0.23	0.271	1.24	3.149	0.16	0.229	4.283	3.781	0.330	1.337	0.52	99.61	98.18	7.69
0.23	0.271	1.26	2.730	0.16	0.232	4.286	3.786	0.351	1.343	0.52	99.62	98.07	8.11
0.30	0.303	1.20	3.089	0.23	0.258	4.278	3.780	0.313	1.322	0.52	99.64	98.32	7.70
0.30	0.303	1.22	2.685	0.23	0.260	4.282	3.784	0.335	1.328	0.52	99.72	98.13	7.94
0.30	0.303	1.24	2.296	0.24	0.263	4.285	3.788	0.357	1.334	0.52	99.78	98.15	8.34
0.30	0.303	1.26	1.907	0.23	0.257	4.290	3.793	0.376	1.337	0.52	100.23	98.20	8.84
0.30	0.271	1.24	3.637	0.23	0.231	4.282	3.773	0.295	1.338	0.52	99.56	98.27	7.30
0.30	0.271	1.26	3.173	0.23	0.232	4.284	3.777	0.317	1.345	0.52	99.50	98.16	7.64
0.30	0.271	1.28	2.730	0.23	0.233	4.288	3.781	0.337	1.351	0.52	99.64	98.09	8.08
0.30	0.271	1.30	2.326	0.23	0.236	4.291	3.785	0.357	1.355	0.52	99.80	98.20	8.52

Notes. Here $\langle\Delta\nu^*\rangle$ represents the Kjeldsen et al. (2008)-corrected large separations.

lowest helium abundance, represented by black squares in Fig. 6, is at the coolest limit of the observational boxes, thus may be excluded from the sample on spectroscopic grounds. We derive the stellar parameters from the mean value for the resulting three models, as given in Table 5.

4. Scaling relations and automatic fits

4.1. Scaling relations

The empirical scaling relations proposed by Kjeldsen & Bedding (1995) can give approximate values of the mass and radius of a star based on the observed average large separation, the frequency at the maximum of the power spectrum, and the observed effective temperature

$$\frac{M}{M_\odot} = \left(\frac{135\,\mu\text{Hz}}{\langle\Delta\nu\rangle}\right)^4 \left(\frac{\nu_{\rm max}}{3050\,\mu\text{Hz}}\right)^3 \left(\frac{T_{\rm eff}}{5777\,\text{K}}\right)^{3/2} \quad (4)$$

$$\frac{R}{R_\odot} = \left(\frac{135\,\mu\text{Hz}}{\langle\Delta\nu\rangle}\right)^2 \left(\frac{\nu_{\rm max}}{3050\,\mu\text{Hz}}\right) \left(\frac{T_{\rm eff}}{5777\,\text{K}}\right)^{1/2}. \quad (5)$$

For HD 52265, the frequency at the maximum amplitude is $\nu_{\rm max} = 2090 \pm 20\ \mu$Hz (Ballot et al. 2011). With a large

Table 4. Best-fit models obtained with the TGEC code, including near surface corrections.

$M/M_\odot$	$L/L_\odot$	$R/R_\odot$	log g	$T_{\rm eff}$ [K]	Age [Gyr]	[Fe/H]$_i$	Y_i	[Fe/H]$_S$	Y_S	χ^2
1.22	2.239	1.327	4.282	6143	2.670	0.23	0.293	0.16	0.250	5.06
1.23	2.219	1.330	4.283	6120	2.476	0.30	0.303	0.23	0.262	3.34
1.26	2.244	1.343	4.286	6109	2.730	0.23	0.271	0.16	0.232	6.42
1.28	2.173	1.351	4.288	6043	2.730	0.30	0.271	0.23	0.233	3.51

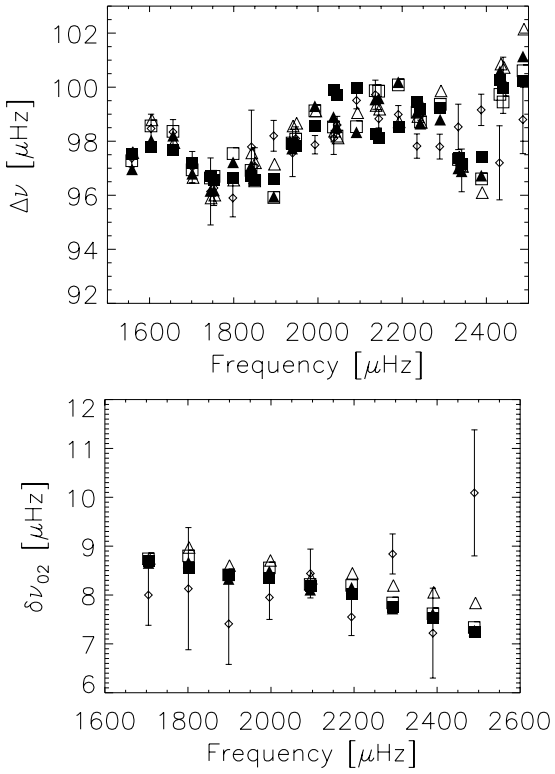

Fig. 5. Comparisons between the large separations (*top*) and the small separations (*bottom*) of the four best-fit models indicated by squares for models with [Fe/H]$_s$ = 0.23 ([Fe/H]$_i$ = 0.30) and triangles for models with [Fe/H]$_s$ = 0.16 ([Fe/H]$_i$ = 0.23). Empty symbols are used to indicate a helium abundance according to Y_g, and filled symbols for a solar helium abundance (see text for details). Observations are represented as white diamonds.

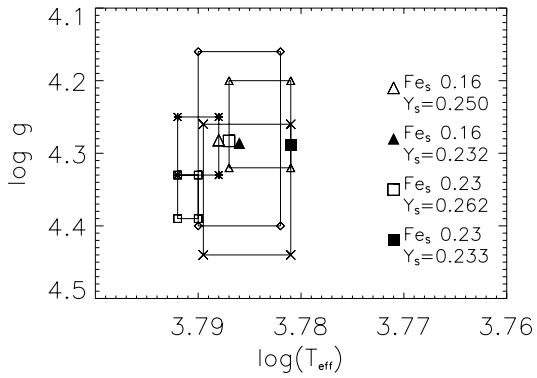

Fig. 6. Location of the best-fit models in the log g vs. log $T_{\rm eff}$ plane. Triangles indicate models with [Fe/H]$_s$ = 0.16 ([Fe/H]$_i$ = 0.23), and squares indicate models with [Fe/H]$_s$ = 0.23 ([Fe/H]$_i$ = 0.30). Filled symbols are used to show the models with a solar helium value. Error boxes correspond to the Gonzalez et al. (2001) (asterisks), Santos et al. (2004) (diamonds), Gillon & Magain (2006) (squares), Fisher & Valenti (2005) (triangles), and Ballot et al. (2011) (crosses) spectroscopic studies.

Table 5. Final results for the parameters of the exoplanet-host star HD 52265 obtained with the TGEC code.

$M/M_\odot$ = 1.24 ± 0.02	[Fe/H]$_i$ = 0.27 ± 0.04
$R/R_\odot$ = 1.33 ± 0.02	Y_i = 0.28 ± 0.02
$L/L_\odot$ = 2.23 ± 0.03	[Fe/H]$_s$ = 0.20 ± 0.04
log g = 4.284 ± 0.002	Y_s = 0.25 ± 0.02
Age (Gyr) = 2.6 ± 0.2	$T_{\rm eff}$ (K) = 6120 ± 20

separation of 98.4 μHz and an effective temperature of 6100 K, we obtain from these relations M = 1.23 $M_\odot$ and R = 1.32 $R_\odot$. With a large separation corrected for the surface effects, of 99.4 μHz, we obtain M = 1.19 $M_\odot$ and R = 1.29 $R_\odot$. In spite of the uncertainties, these results are in good agreement with our own results.

4.2. Results from the SEEK code

Computations have been done for this star using the SEEK automatic code (Quirion et al. 2010; Gizon et al. 2012). This code makes use of a large grid of stellar models computed with the Aarhus Stellar Evolution Code (ASTEC). It searches for the best-fit model corresponding to a seismically observed star, with the help of Bayesian statistics. The input parameters are the large and small average separations, the spectroscopic observables ($T_{\rm eff}$, log g, [Fe/H]), and the absolute magnitude. The output gives the stellar mass, radius, and age. In the case of HD 52265, the values of mass and radius given by the SEEK code are slightly larger than our results, and the age is younger, i.e. M = 1.27 ± 0.03 $M_\odot$, R = 1.34 ± 0.02 $R_\odot$, and age = 2.37 ± 0.29 Gyr. The differences between the SEEK results and our own may be related to a different initial helium, to slightly different values of the average large and small separations as given by Gizon et al. (2012), or to the SEEK results corresponding to a secondary maximum of probability, as discussed below.

4.3. Results from the asteroseismic modeling portal

We also performed computations for HD 52265 using the Asteroseismic Modeling Portal[2] (AMP). The AMP provides a web-based interface for deriving the stellar parameters of Sun-like stars from asteroseismic data, and was developed at the High Altitude Observatory and the Computational & Information Systems Laboratory of the National Center for Atmospheric Research (Metcalfe et al. 2009). It uses the ASTEC and ADIPLS codes (Christensen-Dalsgaard 2008a,b) coupled with a parallel genetic algorithm (Metcalfe & Charbonneau 2003).

[2] https://amp.ucar.edu/

Table 6. Final results for the parameters of the exoplanet-host star HD 52265 obtained from AMP automatic analysis, using (a) all observed frequencies or (b) only the most reliable frequencies.

	AMP(a)	AMP(b)
$M/M_\odot$	1.22	1.20
$R/R_\odot$	1.321	1.310
$L/L_\odot$	2.058	2.128
$\log g$	4.282	4.282
[Fe/H]	0.23	0.215
Y	0.280	0.298
Age (Gyr)	3.00	2.38
$T_{\rm eff}$	6019	6097

Two different computations were done, the first one, AMP(a), by Vauclair using all the observed frequencies given by Ballot et al. (2011), and the second one, AMP(b), by S. Mathur using only the most reliable frequencies (($l = 0, n = 14$), ($l = 1, n = 14$) and ($l = 2, n = 15$) were excluded). The final results are very close to the parameters found by using the TGEC code (Table 6). Interestingly, the code also found solutions for a mass of 1.27 $M_\odot$ with both a small Y (about 0.26) and a young age (about 2.7 Gyr) but the χ^2 tests showed that these results corresponded to secondary maxima, not to the best-fit solution.

5. Summary and conclusions

We have performed a detailed analysis of the exoplanet-host star HD 52265, which was observed by CoRoT over 117 consecutive days, as one of the main targets. The very precise observational results obtained for this star (Ballot et al. 2011) have allowed us to perform a precise determination of its parameters, using classical comparisons between models computed with the TGEC and observational data. In our computations, we have included the atomic diffusion of helium and heavy elements. For the computed stellar models, we have found that the effects of radiative accelerations on individual elements is small and may be neglected. This is consistent with the detailed abundance analysis showing similar enhancements in the heavy elements compared to the Sun. We iterated the model computations until we found a final surface metallicity $[Fe/H]_S$ in the observational range. We also compared these results with those obtained using approximate scaling relations (Kjeldsen & Bedding 1995), and automatic codes such as SEEK (Quirion et al. 2010) and AMP (Metcalfe et al. 2009). Although the detailed physics included in the models varies, these results are in good agreement.

The good concordance between results obtained with the TGEC code and the AMP for Sun-like stars had already been proven for the star μ Arae. The results for this star, which were published separately (Soriano & Vauclair 2010, for TGEC; Doğan et al. 2012, for AMP), are presented in the Appendix for comparison. Taken together, these works represent significant advances in asteroseismic studies of Sun-like stars.

Acknowledgements. Much thanks are due to Travis Metcalfe for fruitful discussions and for introducing S.V. to A.M.P. Computational resources were provided by TeraGrid allocation TG-AST090107 through the Asteroseismic Modeling Portal (AMP). NCAR is partially supported by the Natiional Science Foundation. We also thanks the referee for important and constructive remarks.

Appendix A

Comparison of the results given by the TGEC analysis (Soriano & Vauclair 2008) and the AMP (Doğan et al.2012) for the exoplanet-host sun-like star μ Arae.

Table A.1. Comparison of the results obtained with the TGEC and the AMP for μ Arae.

	TGEC	AMP
$M/M_\odot$	1.1 ± 0.02	1.1
$R/R_\odot$	1.36 ± 0.06	1.365
$L/L_\odot$	1.90 ± 0.10	1.894
$\log g$	4.215 ± 0.005	4.213
$T_{\rm eff}$	5820 ± 50	5807
[Fe/H]	+0.32 ± 0.02	+0.418
Y	0.30 ± 0.01	0.316
Age (Gyr)	6.34 ± 0.80	6.66

References

Alecian, G., & LeBlanc, F. 2002, MNRAS, 332, 891
Angulo, C., Arnould, M., Rayer, M., et al. 1999, Nucl. Phys. A, 656, 3, http://pntpm.ylb.ac.be/Nacre/nacre.htm
Baglin, A., Auvergne, M., Barge, P., et al. 2006, in The CoRoT Mission: Pre-launch Status, eds. M. Fridlund, A. Baglin, J. Lochard, & L. Conroy (Noordwijk: ESA Publication Divisions), ESA SP, 1306, 33
Basu, S., Verner, G. A., Chaplin, W. J., & Elsworth, Y. 2012, ApJ, 746, 76
Ballot, J., Gizon, L., Samadi, R., et al. 2011, A&A, 530, 97
Brassard, P., & Charpinet, S. 2008, Ap&SS, 316, 107
Butler, R. P., Vogt, S., Marcy, G., et al. 2000, ApJ, 545, 504
Christensen-Dalsgaard, J. 1984, in Space Research in Stellar and Variability, eds. A. Mangeney, & F. Praderie, 11
Christensen-Dalsgaard, J. 2008a, Ap&SS, 316, 13
Christensen-Dalsgaard, J. 2008b, Ap&SS, 316, 113
Christensen-Dalsgaard, J., Kjeldsen, H., Brown, T. M., et al. 2010, ApJ, 713, L164
Doğan, G., Metcalfe, T. S., Woitaszek, M., et al. 2012, ApJ, submitted
Fischer, D. A., & Valenti, J. A. 2005, ApJ, 622, 1102
Gillon, M., & Magain, P. 2006, A&A, 448, 341
Gizon, L., Ballot, J., Michel, E., et al. 2012, Nature, submitted
Gonzalez, G., Laws, C., Tyagi, S., & Reddy, B. E. 2001, ApJ, 121, 432
Gough, D. O. 1986, in Hydrodynamic and magnetohydrodynamic problems in the Sun and stars, ed. Y. Osaki (Univ. of Tokyo Press), 117
Grevesse, N., & Noels, A. 1993, in Origin and Evolution of the Elements, eds. N. Prantzos, E. Vangioni-Flam, & M. Cassé (Cambridge University Press), 15
Hui-Bon-Hoa, A. 2008, Ap&SS, 316, 55
Iglesias, C. A., & Rogers, F. J. 1996, ApJ, 464, 943
Izotov, Y. I., & Thuan, T. X. 2004, ApJ, 602, 200
Izotov, Y. I., & Thuan, T. X. 2010, ApJ, 710, L67
Kjeldsen, H., & Bedding, T. R. 1995, A&A, 293, 87
Kjeldsen, H., Bedding, T. R., & Christensen-Dalsgaard, J. 2008, ApJ, 683, L175
Koch, D. G., Borucki, W. J., Basri, G., et al. 2010, ApJ, 713, L79
LeBlanc, F., & Alecian, G. 2004, MNRAS, 352, 1329
van Leeuwen, F. 2007, A&A, 474, 653
Metcalfe, T., & Charbonneau, P. 2003, JCoPh, 185, 176
Metcalfe, T., Creevey, O. L., & Christensen-Dalsgaard, J. 2009, ApJ, 699, 373
Michaud, G., Charland, Y., Vauclair, S., & Vauclair, G. 1976, ApJ, 210, 447
Michaud, G., Richard, O., Richer, J., & VandenBerg, D. 2004, ApJ, 606, 452
Naef, D., Mayor, M., Pepe, F., et al. 2001, A&A, 375, 205
Paquette, C., Pelletier, C., Fontaine, G., & Michaud, G. 1986, ApJS, 61, 177
Quirion, P. O., Christensen-Dalsgaard, J., & Arenthoft, T. 2010, ApJ, 725, 2176
Richard, O., Michaud, G., & Richer, J. 2001, ApJ, 558, 377
Rogers, F. J., & Nayfonov, A. 2002, ApJ, 576, 1064
Roxburgh, I. W., & Vorontsov, S. V. 1994, MNRAS, 267, 297
Santos, N. C., Israelian, G., & Mayor, M. 2004, A&A, 415, 1153
Soriano, M., & Vauclair, S. 2008, A&A, 488, 975
Soriano, M., & Vauclair, S. 2010, A&A, 513, A49
Soriano, M., Vauclair, S., Vauclair, G., & Laymand, M. 2007, A&A, 471, 885
Southworth, J. 2011, MNRAS, 417, 216
Stahn, T. 2011, Ph.D. Thesis, University of Göttingen, Germany
Takeda, Y., Ohkubo, M., Sato, B., Kambe, E., & Sadakane, K. 2005, PASJ, 57, 27
Tassoul, M. 1980, ApJS, 43, 469
Théado, S., Vauclair, S., Alecian, G., & LeBlanc, F. 2009, ApJ, 704, 1262
Ulrich, R. K. 1986, ApJ, 306, L37
Vauclair, S. 2004, ApJ, 605, 874
Vauclair, S., Laymand, M., Bouchy, F., et al. 2008, A&A, 482, L5
White, T. R., Bedding, T. R., Stello, D., et al. 2011, ApJ, 743, 161

Precise Modeling of the Exoplanet Host Star and CoRoT Main Tarjet HD 52265

Escobar, M. E; Théado, S.; Vauclair, S.; Ballot, J.; Dolez, N.; Charpinet, S.; Vauclair, G.; Gizon, L., 2011

Proceedings of 20th Stellar Pulsation Conference Series "Impact of New Intrumentation and New Insights in Stellar Pulsations"

Precise Modeling of the Exoplanet Host Star and CoRoT Main Tarjet HD 52265

M. E. Escobar, S. Théado, S.Vauclair, J. Ballot, N. Dolez, S. Charpinet, G. Vauclair, L. Gizon

Abstract We present the results of a detailed modelling of the CoRoT main target HD52265, the only main target with a detected exoplanet. We computed evolutionary tracks using the Toulouse-Geneva Evolution Code (TGEC) for a range of masses between 1.10 and 1.30 $M_{\odot}$, and for four different sets of initial chemical composition. We obtained adiabatic mode frequencies using the PULSE code. We derive models which best fit all the observational constraints. We have studied the impact on the obtained results of including or not atomic diffusion, including or not the radiative accelerations on heavy elements, varying the mixing length parameter, and applying near-surface corrections. All the results presented here include gravitational atomic diffusion.

1 Evolutionary Tracks, Frequency Computations and Results

We computed evolutionary tracks using the Toulouse-Geneva Evolution Code (TGEC), for a range of masses between 1.10 and 1.30 $M_{\odot}$, and using four different sets of initial chemical composition: two different metallicities, [Fe/H]=0.19 or 0.23, and two differents initial helium abundances, Yg (increasing with the metal content as observed in galaxies) or $Y_{\odot}$=0.271 (see Fig. 1). The TGEC includes the OPAL equation of state and opacities and the NACRE nuclear reaction rates. Convection is treated with the mixing length theory. We first used a mixing length parameter adjusted to that of the Sun (α=1.8), and we then decreased it to study the impact on the results. Adiabatic mode frequencies were computed for degrees ℓ=0,1,2. For each set of parameters, we derived the best models which fit the seismic observations: the large and small separations ($\Delta\nu \sim 98.3$ µHz and $\delta\nu_{02} \sim 8.1$ μHz), and the échelle diagrams. We also checked the δ_{01} differences as defined in [3]. A first analysis of

M.E Escobar
Institute de Recherche en Astrophysique et Planétologie, 14 Avenue Edouard Belin, Toulouse, France, e-mail: mescobar@irap.omp.eu

these oscillations yields an acoustic radius of the convective zone in the real star of 2650 sec. This value has however to be taken cautiously because of the large uncertainties (see [1]). The computed value is 2680 sec for the 1.25 $M_\odot$ model with α=1.4.

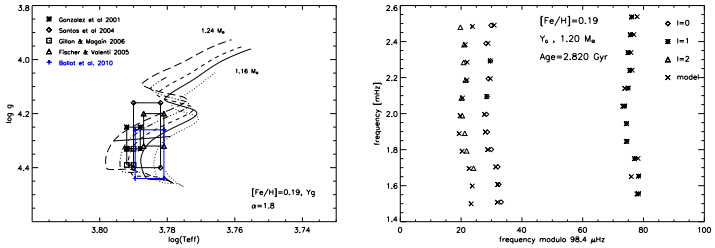

Fig. 1 *Left*: Evolutionary tracks from 1.16 to 1.24 $M_\odot$, for the case [Fe/H]=0.19, Y_g=0.289, in the log g – log T_{eff} plane. Error boxes correspond to the spectroscopic studies of Gonzales et al. 2001 (*asterisks*), Santos et al. 2004 (*diamonds*), Fisher & Valenti 2005 (*triangles*), Gillon & Magain 2006 (*squares*), and Ballot et al. 2011 (*blue plus signs*).*Right*: Example of a échelle diagram corrected by near-surface effects for the best model found for M=1.20 $M_\odot$, and α=1.8

Surface effects corrections have been introduced using the method proposed by Reference [2]. We also computed an evolutionary track for 1.18 $M_\odot$ including radiative accelerations on C, N, O, Ca and Fe. For a low mass star as HD 52265, the effect of including radiative accelerations is of order 1% on the frequencies.

Robust results appear in the determinations of the stellar parameters from asteroseismology. The gravity is precisely fixed and similar in all models within 0.1%: log g = 4.29. The radius is also the same one in all models within 1%: $R/R_\odot$= 1.305. Luminosities and effective temperatures are known within a few %: Teff = 6100 and $L/L_\odot$=2.1. On the other hand, masses and ages more strongly depend on Y and α. For large Y, increasing with [Fe/H], the masses of the best models lie between 1.18 and 1.22 $M_\odot$, whereas for smaller Y the masses are slightly larger (1.22 to 1.26 $M_\odot$). In both cases the ages lie in the interval of 2.45 to 3.40 Gyr. When decreasing the value of α, the best model becomes more massive and young. For Yg and [Fe/H]=0.19, α=1.8, we find a best model for a mass of 1.18 $M_\odot$ and an age of 3.37 Gyr whereas for α=1.4, we obtain a mass of 1.25 $M_\odot$ and an age of only 1.05 Gyr.

References

1. Ballot, J., Gizon, L., Samadi, R. et al., Astron. & Astroph. , **530**, A97 (2011)
2. Kjeldsen, H., Bedding, T. R., & Christensen-Dalsgaard, J., Astrophys. Journal Letters, **683**, 175 (2008)
3. Roxburgh, I. W., in PRISMA, Report on the phase-A Study, ed. T. Appourchaux et al., ESA SCI 93(3), 31 (1993)

Asteroseismology of the CoRoT main target HD 52265

Escobar, M. E; Théado, S.; Vauclair, S.; Ballot, J.; Dolez, N.; Charpinet, S.; Vauclair, G.; Gizon, L., 2011

Proceedings of 2nd Stellar CoRoT Symposium "Transiting Planets, Vibrating Stars and their Connection"

Transiting planets, vibrating stars & their connection
Proceedings of the 2nd CoRoT symposium (14 - 17 June 2011, Marseille)
Edited by A. Baglin, M. Deleuil, E. Michel & C. Moutou

Asteroseismology of the CoRoT main target HD 52265

M. E. Escobar[1], S. Théado[1], S.Vauclair[1, 2], J. Ballot[1], N. Dolez[1], S. Charpinet[1], G. Vauclair[1], L. Gizon[3]

[1] *Institute de Recherche en Astrophysique et Planétologie, 14 Avenue Edouard Belin, Toulouse, France [mescobar@irap.omp.eu]*
[2] *Institute Universitaire de France*
[3] *Max-Planck-Institut fur Sonnensystemforschung, 37191 Kaltenburg-Lindau, Germany*

Abstract. We present the results of a detailed modelling of the *CoRoT* main target HD 52265, the only main target with a detected exoplanet. We computed evolutionary tracks using the Toulouse-Geneva Evolution Code (TGEC) for a range of masses between 1.10 and 1.30 $M_{\odot}$, and for four different sets of initial chemical composition. We obtained adiabatic mode frequencies using the PULSE code. Applying a χ–square statistical test and taking into account the log g – log Teff – [Fe/H] triplet from spectroscopic observations, we are able to derive models which best fit all the observational constraints. We have studied the impact on the obtained results of including or not atomic diffusion, including or not the radiative accelerations on heavy elements, varying the mixing length parameter, and applying near-surface corrections. All the results presented here include gravitational atomic diffusion.

1. Introduction

Asteroseismology has proved to be a useful and accurate tool to study stellar interiors. It is important in the extra-solar planet context, as the properties of the exoplanet-host stars need to be known with a high precision. HD 52265 is the only CoRoT main target with an orbiting exoplanet. This main sequence G0V star was observed by CoRoT between November 2008 and March 2009, collecting 117 days of high-precision photometric data. These observations allowed the detection of 31 p-modes of orders ℓ=0,1,2 with a very high precision (Ballot *et al.* 2011). Also the rotation period could be precisely determined, and a first estimate of the stellar parameters obtained with the automatic code SEEK is given in Gizon *et al.* 2011. Here we present a more detailed asteroseismic modelling of this star, with a precise exploration of the various parameters.

2. Evolutionary Tracks, Seismic Tests and Results

We computed evolutionary tracks using the Toulouse-Geneva Evolution Code (TGEC), for a range of masses between 1.10 and 1.30 $M_{\odot}$, and using four different sets of initial chemical composition: two different metallicities, [Fe/H]= 0.19 or 0.23, and two differents initial helium abundances, Yg (increasing with the metal content as observed in galaxies) or $Y_{\odot}$=0.271. The TGEC includes the OPAL equation of state and opacities and the NACRE nuclear reaction rates, and convection is treated with the mixing length theory. We first used a mixing length parameter adjusted to that of the Sun ($\alpha = 1.8$), and we then decreased it to study the impact on the results (see below). Adiabatic mode frequencies were computed for degrees ℓ=0,1,2. For each set of parameters, we derived the best models which fit the seismic observations: the large and small separations ($\Delta\nu \sim 98.3$ μHz and $\delta\nu_{02} \sim 8.1$ μHz), and the échelle diagrams. We also checked the δ_{01} differences as defined in Roxburgh *et al.* 1993. The visible oscillations of these small differences are due to the bottom of the convective zone. A first analysis of these oscillations yields an acoustic radius of the convective zone in the real star of 2650 sec. This value

has however to be taken cautiously because of the large uncertainties (see Ballot *et al.* 2011). The computed value is 2680 sec for the 1.25 $M_{\odot}$ model with α=1.4.

We applied near-surface corrections (Kjeldsen *et al.* 2008) to the computed frequencies. An example of a resulting échelle diagram is shown in Fig. 1. We do obtain a better match of the échelle diagrams but in any case the parameters of the resulting models do not differ from the ones without corrections by more than 1%. We also computed an evolutionary track for 1.18 $M_{\odot}$ using a new version of the TGEC, which includes radiative accelerations on C, N, O, Ca and Fe. We proceeded as before to obtain the best model within this track. We could check that for a low mass star as HD 52265, the effect of including radiative accelerations is of order 1% on the frequencies.

We conclude that robust results appear in the determinations of the stellar parameters from asteroseismology. The gravity is precisely fixed and similar in all models within 0.1%: log g = 4.29. The radius is also the same one in all models within 1%: $R/R_{\odot}$= 1.305. Luminosities and effective temperatures are known within a few %: Teff = 6100 and $L/L_{\odot}$=2.1. On the other hand, masses and ages more strongly depend on Y and α. For large Y, increasing with [Fe/H], the masses of the best models lie between 1.18 and 1.22 $M_{\odot}$, whereas for smaller Y the masses are slightly larger (1.22 to 1.26 $M_{\odot}$). In both cases the ages lie in the interval of 2.45 to 3.40 Gyr. When decreasing the value of α, the best model becomes more massive and young. For Yg and [Fe/H]=0.19, α=1.8, we find a best model for a mass of 1.18 $M_{\odot}$ and an age of 3.37 Gyr whereas for α=1.4, we obtain a mass of 1.25 $M_{\odot}$ and an age of only 1.05 Gyr.

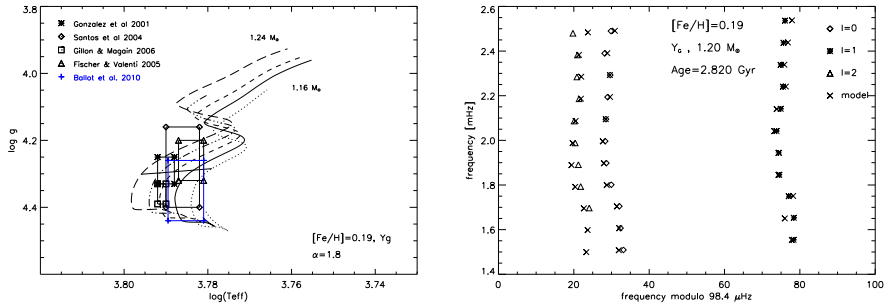

Figure 1.: *Right: Evolutionary tracks from 1.16 to 1.24 $M_{\odot}$, for the case [Fe/H]=0.19, Y_g=0.289, in the log g – log $T_{\rm eff}$ plane. Error boxes correspond to the spectroscopic studies of Gonzales* et al.*2001 (asterisks), Santos* et al.*2004 (diamonds), Fisher & Valenti 2005 (triangles), Gillon & Magain 2006 (squares), and Ballot* et al.*2011 (blue plus signs).Left: Example of a échelle diagram corrected by near-surface effects for the best model found for M=1.20 $M_{\odot}$, and α=1.8*

References

Ballot, J., Gizon, L., Samadi, R. et al. 2011, A&A, 530, A97.

Gizon, L. et al. 2011, in preparation.

Kjeldsen, H., Bedding, T. R., & Christensen-Dalsgaard, J. 2008, ApJ, 683, 175.

Roxburgh, I. W., 1993, in PRISMA, Report on the phase-A Study, ed. T. Appourchaux et al., ESA SCI 93(3), 31.

List of Figures

List of Tables

Bibliography

Aerts, C. & Christensen-Dalsgaard, J. and Kurtz, D. W.: 2010, *Asteroseismology*, Springer

Alecian, G. & LeBlanc, F.: 2002, *Mon. Not. R. Astron. Soc.* **332**, 891

Angulo, C., Arnould, M., Rayer, M., Descouvemont, P., Baye, D., & 23 coauthors: 1999, *Nucl. Phys. A* **656**, 3

Baglin, A., Auvergne, M., Barge, P., Deleuil, M., Catala, C., Michel, E., Weiss, W., & The COROT Team: 2006, in M. Fridlund, A. Baglin, J. Lochard & L. Conroy (ed.), *Proceedings of The CoRoT Mission Pre-Launch Status - Stellar Seismology and Planet Finding*, Vol. 1306 of *ESA Special Publication*

Baines, E. K., McAlister, H. A., ten Brummelaar, T. A., Turner, N. H., Sturmann, J., Sturmann, L., Goldfinger, P. J., & Ridway, S. T.: 2008, *Astrophys. J.* **680**, 728

Ballot, J., Gizon, L.and Samadi, R., Vauclair, G., Benomar, O., Bruntt, H., Moser, B., & 23 coauthors: 2011, *Astron. & Astrophys.* **530**, A97

Bazot, M., Vauclair, S.and Bouchy, F., & Santos, N. C.: 2005, *Astron. & Astrophys.* **440**, 615

Bensby, T. & Feltzing, S.and Lundstrom, I.: 2003, *Astron. & Astrophys.* **410**, 527

Böhm-Vitense, E.: 1958, *Zeitschrift f´ur Astrophysik* **46**, 108

Bouchy, F., Bazot, M.and Santos, N. C., Vauclair, S., & Sosnowska, D.: 2005, *Astron. & Astrophys.* **440**, 609

Bouchy, F. & Carrier, F.: 2001, *Astron. & Astrophys. Lett.* **374**, L5

Bouchy, F., Deleuil, M.and Guillot, T., Aigrain, A., Carone, L., Cochran, W. D., Almenara, J. M., & 42 coauthors: 2011, *Astron. & Astrophys.* **525**, A68

Brassard, P. & Charpinet, S.: 2008, *Astrophys. & Space Sci.* **316**, 107

Butler, R. P., Vogt, S. S., Marcy, G. W., Fischer, D. A., Henry, G. W., & Apps, K.: 2000, *Astrophys. J.* **545**, 504

Carrier, F., Eggenberger, P., D'Alessandro, A., & Weber, L.: 2005, *New Astr.* **10**, 315

Chaplin, W. J., Kjeldsen, H., Christensen-Dalsgaard, J., Basu, S., Miglio, A., Appourchaux, T., & 53 coauthors: 2011, *Science* **332**, 213

Chen, Y. Q. & Zhao, G.: 2006, *Astron. J.* **131**, 1816

Christensen-Dalsgaard, J.: 1984, *Space Research Prospects in Stellar Activity and Variability*, Chapt. What will asteroseismology teach us?, pp 11–45, Paris Observatory Press

Christensen-Dalsgaard, J.: 2003, *Lecture Notes on Stellar Oscillations*

Christensen-Dalsgaard, J.: 2008, *Astrophys. & Space Sci.* **316**, 113

Christensen-Dalsgaard, J., Dappen, W., Ajukov, S. V., Anderson, E. R., Antia, H. M., Basu, S., & 27 coauthors: 1996, *Science* **272**, 1286

Colavita, M. M.: 1999, *Publ. Astron. Soc. Pacific* **111**, 111

Deleuil, M., Deeg, H. J., Alonso, R., Bouchy, F., Rouan, D., , F., Auvergne, M., Baglin, A., & 35 more authors: 2008, *Astron. & Astrophys.* **491**, 889

Duvall, T. L.: 1982, *Nature* **300**, 242

Edvardsson, B., Andersen, J., Gustafsson, B., Lambert, D. L., Nissen, P. E., & Tomkin, J.: 1993, *Astron. & Astrophys.* **275**, 101

Eggenberger, P. & Carrier, F.: 2006, *Astron. & Astrophys.* **449**, 293

Fischer, D. A. & Valenti, J.: 2005, *Astrophys. J.* **622**, 1102

Fressin, F., Torres, G., Rowe, J. F., Charbonneau, D., Rogers, L. A., Ballard, S., & 30 coauthors: 2012, *Nature* **482**, 195

Fuhrmann, K., Pfeiffer, M. J., & Bernkopf, J.: 1997, *Astron. & Astrophys.* **326**, 1081

Garaud, P.: 2011, *Astrophys. J., Lett.* **728**, L30

Gaulme, P., Deheuvels, S., Weiss, W. W., Mosser, B., Moutou, C., Bruntt, H., & 10 coauthors: 2010, *Astron. & Astrophys.* **524**, A47

Gillon, M. & Magain, P.: 2006, *Astron. & Astrophys.* **448**, 341

Gizon, L., Ballot, J., Michel, E., & et al.: 2012, , submitted

Gizon, L. & Solanki, S. K.: 2003, *Astrophys. J.* **589**, 1009

Gonzalez, G., Laws, C., Tyagi, S., & Reddy, B. E.: 2001, *Astron. J.* **121**, 432

Grevesse, N. & Noels, A.: 1993, in *Origin and evolution of the elements*, pp 15–25

Grevesse, N. & Sauval, A. J.: 1998, *Space Sci. Rev.* **85**, 161

Hale, A.: 1994, *Astron. J.* **107**, 306

Heiter, U. & Luck, R. E.: 2003, *Astron. J.* **126**, 2015

Hoffleit, D. & Jaschek, C.: 1982, *The Bright Star Catalogue*, Yale University Observatory

Hui-Bon-Hoa, A.: 2008, *Astrophys. & Space Sci.* **316**, 55

Iglesias, C. A. & Rogers, F.-J.: 1996, *Astrophys. J.* **464**, 943

Izotov, Y. I. & Thuan, T. X.: 2004, *Astrophys. J.* **602**, 200

Izotov, Y. I. & Thuan, T. X.: 2010, *Astrophys. J., Lett.* **710**, L67

Kjeldsen, H. & Bedding, T. R.: 1995, *Astron. & Astrophys.* **293**, 87

Kjeldsen, H., Bedding, T. R., & Christensen-Dalsgaard, J.: 2008, *Astrophys. J., Lett.* **683**, L175

Koch, D. G., Borucki, W., Basri, G., Batalha, N., Brown, T. M., Caldwell, D., Christensen-Dalsgaard, J., & 40 coauthors: 2010, *Astrophys. J., Lett.* **713**, L79

Lazrek, M., Baudin, F., Bertello, L., Bourmier, P., Charra, J., & 15 coauthors: 1997, *Sol. Phys.* **175**, 227

LeBlanc, F. & Alecian, G.: 2004, *Mon. Not. R. Astron. Soc.* **352**, 1329

Leger, A., Rouan, D., Schneider, J., & CoRoT team: 2009, *Astron. & Astrophys.* **506**, 287

Maldonado, J., Eiroa, C., Villaver, E., Montesinos, B., & Mora, A.: 2012, *Astron. & Astrophys.* **541**, A40

Marcy, G. W., Butler, R. P., Williams, E., Bildsten, L., Graham, J. R., M., G. A., & Jernigan, J. G.: 1997, *Astrophys. J.* **481**, 926

Martic, M., Lebrun, J. C., Appourchaux, T., & Schmitt, J.: 2004, in D.. Danesy (ed.), *Proceedings of the SOHO 14/GONG Workshop - Helio- and Asteroseismology: Towards a Golden Future*, Vol. 559 of *ESA Special Publication*

Mathur, S., Metcalfe, T. S., Woitaszek, M., Bruntt, H., Verner, G. A., Christensen-Dalsgaard, J., & 36 coauthors: 2012, *Astrophys. J.* **749**, 152

Mayor, M. & Queloz, D.: 1995, *Nature* **378**, 355

Mayor, M., Udry, S., Naef, D., Queloz, D., Santos, N. C., & Burnet, M.: 2004, *Astron. & Astrophys.* **415**, 391

Metcalfe, T. S. & Charbonneau, P.: 2003, *Journal of Computational Phys.* **185**, 176

Metcalfe, T. S., Creevey, O., & Christensen-Dalsgaard, J.: 2009, *Astrophys. J.* **699**, 373

Michaud, G., Charland, Y., Vauclair, S., & Vauclair, G.: 1976, *Astrophys. J.* **210**, 447

Michaud, G. & Proffitt, C. R.: 1993, in W. W. Weiss, A. Baglin (ed.), *Proceedings of 137th IAU Colloquium - Inside the stars*, Vol. 40 of *ASP Conference Series*

Michaud, G., Richard, O., Richer, J., & VandenBerg, D. A.: 2004, *Astrophys. J.* **606**, 452

Murphy, E. J., Demarque, P., & Guenther, D. B.: 2004, *Astrophys. J.* **605**, 472

Naef, D., Mayor, M., Beuzit, J. L., Perrier, C., Queloz, D., Sivan, J. P., & Udry, S.: 2004, *Astron. & Astrophys.* **414**, 351

Naef, D., Mayor, M., Pepe, F., Queloz, D., Santos, N. C., Udry, S., & Burnet, M.: 2001, *Astron. & Astrophys.* **375**, 205

Paquette, C., Pelletier, C., Fontaine, G., & Michaud, G.: 1986, *Astrophys. J. Suppl. Ser.* **61**, 177

Pepe, F., Correia, A. C. M., Mayor, M., Tamuz, O., Couetdic, J., Benz, W., Bertaux, J.-L., Bouchy, F., Laskar, J., Lovis, C., Naef, D., Queloz, D., Santos, N., Sivan, J.-P., Sosnowska, D., & Udry, S.: 2007, *Astron. & Astrophys.* **462**, 769

Queloz, D., Bouchy, F., Moutou, C., A., H., Hébrard, G., Alonso, R., Auvergne, M., Baglin, A., & 32 other authors: 2009, *Astron. & Astrophys.* **506**, 303

Queloz, D., Mayor, M., Naef, D., & et al.: 2000, in A. Penny, P. Artymowicz, A.-M. Lagrange & S. Russell (ed.), *Proceedings of IAU Symp. 202 - Planetary Systems in the Universe: Observations, Formation and Evolution*, ASP Conference Series

Quirion, P.-O., Christensen-Dalsgaard, J., Moutou, C., & T., A.: 2010, *Astrophys. J.* **725**, 2176

Ramirez, I., Meléndez, J., & Asplund, M.: 2009, *Astron. & Astrophys. Lett.* **508**, L17

Richard, O., Michaud, G., & Richer, J.: 2001, *Astrophys. J.* **558**, 377

Rogers, F. J. & Nayfonov, A.: 2002, *Astrophys. J.* **576**, 1064

Samadi, R., Ludwing, H.-G., Belkacem, K., Goupil, M. J., Benomar, O., Mosser, B., Dupret, M.-A., Baudin, F., Appourchaux, T., & Michel, E.: 2010, *Astron. & Astrophys.* **509**, A16

Santos, N. C., Bouchy, F., Mayor, M., Pepe, F., Queloz, D., Udry, S., Lovis, C., Bazot, M., Benz, W., Bertaux, J.-L., Lo Curto, G., Delfosse, X., Mordasini, C., Naef, D., Sivan, J.-P., & Vauclair, S.: 2004a, *Astron. & Astrophys. Lett.* **426**, L19

Santos, N. C., Israelian, G., & Mayor, M.: 2001, *Astron. & Astrophys.* **373**, 1019

Santos, N. C., Israelian, G., & Mayor, M.: 2004b, *Astron. & Astrophys.* **415**, 1153

Santos, N. C., Israelian, G., Mayor, M., Bento, J. P., Almeida, P. C., Sousa, S. G., & Ecuvillon, A.: 2005, *Astron. & Astrophys.* **437**, 1127

Santos, N. C., Israelian, G., Mayor, M., Rebolo, R., & Udry, S.: 2003, *Astron. & Astrophys.* **398**, 363

Smith, V. V., Cunha, K., & Lazzaro, D.: 2001, *Astron. J.* **121**, 3207

Soriano, M. & Vauclair, S.: 2010, *Astron. & Astrophys.* **513**, A49

Soriano, M., Vauclair, S., Vauclair, G., & Laymand, M.: 2007, *Astron. & Astrophys.* **471**, 885

Takeda, Y., Ohkubo, M., Sato, B., Kambe, E., & Sadakane, K.: 2005, *Publ. Astron. Soc. Japan* **57**, 27

Tassoul, M.: 1980, *Astrophys. J. Suppl. Ser.* **43**, 469

Théado, S., Alecian, G., LeBlanc, F., & Vauclair, S.: 2012, *Astron. & Astrophys.* **546**, A100

Théado, S., Vauclair, S., Alecian, G., & LeBlanc, F.: 2009, *Astrophys. J.* **704**, 1262

Traxler, A., Garaud, P., & Stellmach, S.: 2011, *Astrophys. J., Lett.* **728**, L29

Unno, W., Osaki, Y., Ando, H., & Shibahashi, H.: 1979, *Nonradial oscillations of stars*, University of Tokyo Press, Tokyo, Japan

Valenti, J. A. & Fischer, D. A.: 2005, *Astrophys. J. Suppl. Ser.* **159**, 141

van Belle, G. T. & von Braun, K.: 2009, *Astrophys. J.* **694**, 1085

van Leeuwen, F.: 2007, *Astron. & Astrophys.* **474**, 653

Vauclair, S.: 2004, *Astrophys. J.* **605**, 874

Vauclair, S., Laymand, M., Bouchy, F., Vauclair, G., Hui-Bon-Hoa, A., Charpinet, S., & Bazot, M.: 2008, *Astron. & Astrophys. Lett.* **482**, L5

Vauclair, S. & Théado, S.: 2012, *Astrophys. J.* **753**, 49V

White, S., Bedding, T. R., Stello, D., Appourchaux, T., Ballot, J., Benomar, O., Bonanno, A., & 26 coauthors: 2011a, *Astrophys. J., Lett.* **742**, L3

White, S., Bedding, T. R., Stello, D., Christensen-Dalsgaard, J., Huber, D., & Kjeldsen, H.: 2011b, *Astrophys. J.* **743**, 161

This thesis was funded by Becas Chile grant.